Pre-flight Calibration and Near-Earth Commissioning Results of the Mercury Plasma Particle Experiment (MPPE) onboard MMO (Mio)

Yoshifumi Saito · Dominique Delcourt ·

Masafumi Hirahara · Stas Barabash ·

Nicolas André · Takeshi Takashima ·

Kazushi Asamura · Shoichiro Yokota ·

Martin Wieser · Masaki N. Nishino ·

Mitsuo Oka · Yoshifumi Futaana · Yuki

Harada · Jean-André Sauvaud · Philippe

Louarn · Benoit Lavraud · Vincent

Génot · Christian Mazelle · Iannis

Dandouras · Christian Jacquey · Claude

Aoustin · Alain Barthe · Alexandre

Cadu · Andréi Fedorov · Anne-Marie

Frezoul · Catherine Garat · Eric Le

Comte · Qiu-Mei Lee · Jean-Louis

Médale · David Moirin · Emmanuel

Penou · Mathieu Petiot · Guy Peyre ·

Jean Rouzaud · Henry-Claude Séran ·

Zdeněk Němeček · Jana Šafránková ·

Maria Federica Marcucci · Roberto Bruno ·

Giuseppe Consolini · Wataru Miyake · Iku

Shinohara · Hiroshi Hasegawa · Kanako

Seki · Andrew J. Coates · Frédéric

Leblanc · Christophe Verdeil · Bruno

Katra · Dominique Fontaine · Jean-Marie

Illiano · Jean-Jacques Berthelier ·

Jean-Denis Techer · Markus Fraenz ·

Henning Fischer · Norbert Krupp ·

Joachim Woch · Ulrich Bührke · Björn

Fiethe · Harald Michalik · Haruhisa

Matsumoto · Tomoki Yanagimachi ·

Yoshizumi Miyoshi · Takefumi Mitani ·

Manabu Shimoyama · Qiugang Zong ·

Peter Wurz · Herman Andersson · Stefan

Karlsson · Mats Holmström · Yoichi

Kazama · Wing-Huen Ip · Masahiro

Hoshino · Masaki Fujimoto · Naoki

Terada · Kunihiro Keika · BepiColombo

Mio/MPPE Team

Y. Saito

Institute of Space and Astronautical Science, Japan Aerospace Exploration Agency, 3-1-1

Yoshinodai, Chuo, Sagamihara, Kanagawa 252-5210, Japan

Tel.: +81-5033624632

Fax: +81-427598456

E-mail: saito@stp.isas.jaxa.jp

D. Delcourt, F. Leblanc, B. Katra, D. Fontaine, J.-M. Illiano, J.-D. Techer

LPP-CNRS-Sorbonne Université-Ecole Polytechnique, 4 place Jussieu, 75252 Paris, France

M. Hirahara, Y. Miyoshi

ISEE, Nagoya University, Furo-cho, Chikusa-ku, Nagoya 464-8601, Japan

S. Barabash, M. Wieser, H. Andersson, S. Karlsson, M. Holmström, Y. Futaana, M. Shimoyama

Swedish Institute of Space Physics, Box 812, 98128, Kiruna, Sweden

N. André, J. A. Sauvaud, P. Louarn, B. Lavraud, V. Génot, C. Mazelle, I. Dandouras, C. Jacquey, C. Aoustin, A. Fedorov, E. Le Comte, Q.-M. Lee, J.-L. Médale, E. Penou, M. Petiot , J. Rouzaud, H.-C. Séran, C. Verdeil

IRAP, CNES, CNRS, Université de Toulouse, Toulouse, France

T. Takashima, K. Asamura, M. N. Nishino, I. Shinohara, H. Hasegawa, T. Mitani, M. Fujimoto

Institute of Space and Astronautical Science, Japan Aerospace Exploration Agency, 3-1-1 Yoshinodai, Chuo, Sagamihara, Kanagawa 252-5210, Japan

S. Yokota

Osaka University, 1-1 Machikaneyama-cho, Toyonaka-shi, Osaka 560-0043, Japan

M. Oka

Space Sciences Laboratory, University of California, Berkeley, 7 Gauss Way, Berkeley, CA 94720, U.S.A

Y. Harada

Kyoto University, Kitashirakawa Oiwakecho, Sakyo-ku, Kyoto, 606-8502, Japan

—————————————————

A. Barthe

AKKA Technologies, Toulouse, France

A. Cadu

ISAE, Toulouse, France

A.-M. Frezoul

Microtec, groupe AGORA Industries, Labège, France

C. Garat, D. Moirin

NEXEYA, Toulouse, France

G. Peyre

COMAT, groupe AGORA Industries, Flourens, France

Z. Němeček, J. Šafránková

Charles University, Faculty of Mathematics and Physics, V Holešovičkách 2, 180 00 Prague 8,

Czech Republic

M. F. Marcucci, R. Bruno, G. Consolini

INAF, Istituto di Astrofisica e Planetologia Spaziali, Roma, Italy

W. Miyake

Tokai University, 4-1-1 Kitakaname, Hiratsuka-shi, Kanagawa, Japan

K. Seki, M. Hoshino, K. Keika

University of Tokyo, 7-3-1 Hongo, Bunkyo, Tokyo 113-0033, Japan

────────────────────────

A. J. Coates

MSSL, University College London, Holmbury St Mary, Dorking RH5 6NT, UK

J.-J. Berthelier

LATMOS-CNRS-IPSL, 4 place Jussieu, 75252 Paris, France

M. Fraenz, H. Fischer, N. Krupp, J, Woch, U. Bührke

MPS, Justus-von-Liebig Weg 3, 37077 Goettingen, Germany

B. Fiethe, H. Michalik

IDA, Hans-Sommer-Str. 66, D-38106 Braunschweig, Germany

H. Matsumoto

JAXA, Sengen 2chome, Tsukuba, Ibaraki 305-8505, Japan

T. Yanagimachi

Rikkyo University, 3-34-1 Nishi-Ikebukuro, Toshima-ku, Tokyo 171-8501, Japan

Q. Zong

Peking University, North Physics Building, Peking University, Beijing, 100871, China

P. Wurz

University of Bern,CH-3012, Bern, Switzerland

Y. Kazama

Academia Sinica Institute of Astronomy and Astrophysics, No.1, Sec. 4, Roosevelt Rd, Taipei 10617, Taiwan

Abstract BepiColombo Mio (previously called MMO: Mercury Magnetospheric Orbiter) was successfully launched by Ariane 5 from Kourou, French Guiana on October 20, 2018. The Mercury Plasma/Particle Experiment (MPPE) is a comprehensive instrument package onboard Mio spacecraft used for plasma, high-energy particle and energetic neutral atom measurements. It consists of seven sensors

W.-H. Ip

IASS, National Central University, Chung-Li, 32054 Taiwan

N. Terada

Tohoku University, Aramaki-aza-aoba, Aoba-ku, Sendai, Miyagi 980-8578, Japan

BepiColombo Mio/MPPE Team

Y. Saito, M. Hirahara, S. Barabash, D. Delcourt, A. Coates, N. André, T. Takashima, K. Asamura, C. Aoustin, J.-A. Sauvaud, P. Louarn, M.Blanc, C. Jacquey, C. Mazelle, I. Dandouras, V. Genot, D. Toublanc, C. Peymirat, A. Fedorov, E. Amata, R. Bruno, M. B. Cattaneo, G. Consolini, M. F. Marcucci, Z. Němeček, B. Lavraud, L. Griton, S. Aizawa, H.-C. Seran, J. Rouzaud, Q. M. Lee, E. Le Comte, E. Penou, M. Petiot, D. Moirin, S. Machida, I. Shinohara, W. Miyake, T. Terasawa, C. Owen, A. Fazakerley, T. Nagatsuma, K. Seki, T. Nagai, A. Ieda, H. Hasegawa, J.-J. Berthelier, D. Fontaine, N. Krupp, J. Woch, S. Yokota, M. Fraenz, H. Krueger, H. Michalik, L. Hadid, R. Modolo, B. Fiethe, B. Katra, F. Leblanc, C. Verdeil, H. Fischer, J.-D. Techer, D. Reisenfeld, R. Elphic, H. Funsten, D. McComas, M. Grande, H. Matsumoto, T. Yanagimachi, T. Obara, Y. Miyoshi, Y. Ebihara, M. Nose, F. Tsuchiya, T. A. Fritz, Q. Zong, T. Mitani, S. Kasahara, M. Shimoyama, Y. Kazama, M. Yamauchi, M. Holmström, Y. Futaana, R. Lundin, P. Wurz, M. Wieser, H. Andersson, S. Karlsson, W. Benz, W.-H. Ip, L.-N. Hau, M. Hoshino, M. Fujimoto, K. Maezawa, N. Terada, P. Trávníček, R. Smets, R. Modolo, F. Leblanc, R. Lallement, L. Zelenyi, H. Malova, M. N. Nishino, Y.-C. Wang, M. Oka, M. Yagi, Y. Harada, L. Xie, J. Zhong, J. Vaverka, K. Keika, W. Sun, L. Wang

including two Mercury Electron Analyzers (MEA1 and MEA2), Mercury Ion Analyzer (MIA), Mass Spectrum Analyzer (MSA), High Energy Particle instrument for electron (HEP-ele), High Energy Particle instrument for ion (HEP-ion), and Energetic Neutrals Analyzer (ENA). Significant efforts were made pre-flight to calibrate all of the MPPE sensors at the appropriate facilities on the ground. High voltage commissioning of MPPE analyzers was successfully performed between June and August 2019 and in February 2020 following the completion of the low voltage commissioning in November 2018. Although all of the MPPE analyzers are now ready to begin observation, the full service performance has been delayed until Mio's arrival at Mercury. Most of the fields of view (FOVs) of the MPPE analyzers are blocked by the thermal shield surrounding the Mio spacecraft during the cruising phase. Together with other instruments on Mio including Magnetic Field Investigation (MGF) and Plasma Wave Investigation (PWI) that measure plasma field parameters, MPPE will contribute to the comprehensive understanding of the plasma environment around Mercury when BepiColombo/Mio begins observation after arriving at the planet Mercury in December 2025.

Keywords Mercury · Magnetosphere · Solar Wind · Exosphere · Ion · Electron · Energetic Neutral Atom

1 Introduction

Our knowledge of Mercury's plasma environment has significantly increased during the past decade owing to new observations made by the Mercury orbiter MESSENGER. However, many questions remain. To provide greater detail on this plasma environment, BepiColombo Mio was successfully launched by Ariane 5

from Kourou, French Guiana on October 20, 2018 as part of a joint mission between European Space Agency (ESA) and Institute of Space and Astronautical Science/Japan Aerospace Exploration Agency (ISAS/JAXA).

When BepiColombo Mission began about 15 years ago, Mercury was one of the least explored planets of our solar system. No spacecraft had visited Mercury since Mariner 10 made three fly-bys past the planet in 1974 and 1975. Mariner 10 discovered that Mercury possesses an intrinsic magnetic field with very weak intensity compared with that of other magnetized planets in our solar system (Ness et al., 1974; Ogilvie et al., 1974). About 30 years after Mariner 10 visited Mercury, MESSENGER made its first fly-by observation in 2008. In 2011, MESSENGER was inserted into Mercury's orbit to become the world's first Mercury orbiter, which continued observation for more than four years.

Mariner 10 discovered the dominance of the dipole term in the spherical harmonic expansion of Mercury's magnetic field. This suggests that the interaction between the solar wind and Mercury's magnetosphere should be " Earth-like ", in contrast to the cases of Mars and Venus in which the planetary magnetic fields have negligible intensity or have only local effects on the interaction. The MESSENGER observation revealed that the dipole moment of Mercury is deviated from its center northward by about 20% of the planet's radius (Anderson et al., 2011). Because the magnetic field reflects the internal structure and its dynamics, detailed observation of Mercury's magnetic field is one of the most important targets of BepiColombo.

Mercury's small size and low gravity result in environmental characterisctics that differ significantly from those of Earth. MESSENGER clearly showed the extremely dynamic behavior of Mercury's magnetosphere where substorm-like phe-

nomena repeat with very short time scales (Imber and Slavin, 2017). MESSEN-
GER also proved the existence of large amounts of heavy elements in the magne-
tosphere (Zurbuchen et al., 2011). BepiColombo/Mio will make exhaustive mea-
surements of Mercury's magnetosphere including comprehensive measurements of
plasma and particles. Such observation of plasma and particles from spinning
spacecraft covering a 4π FOV with a time resolution as high as a few seconds
will reveal the mechanism of the substorm-like phenomena occurring in Mercury's
magnetosphere to clarify similarity and difference between Earth and Mercury. In
addition, the ion energy mass spectrometer on Mio has high mass resolution that
can distinguish between the species of planetary heavy ions. This will help to ex-
plain the contribution of heavy ions on the magnetospheric processes in Mercury's
magnetosphere.

The Mercury Plasma/Particle Experiment (MPPE) is a comprehensive instru-
ment package used for plasma, high-energy particle and energetic neutral atom
measurements. It consists of seven sensors including two Mercury Electron Ana-
lyzers (MEA1 and MEA2), Mercury Ion Analyzer (MIA), Mass Spectrum Analyzer
(MSA), High Energy Particle instrument for electron (HEP-ele), High Energy Par-
ticle instrument for ion (HEP-ion), and Energetic Neutrals Analyzer (ENA).

Together with other instruments onboard Mio including Magnetic Field In-
vestigation (MGF) and Plasma Wave Investigation (PWI) that measure plasma
field parameters, MPPE will contribute to the comprehensive understanding of the
plasma environment around Mercury when BepiColombo/Mio begins observation
after arriving at the planet Mercury in December 2025.

2 Science Objectives of MPPE

2.1 Structure, dynamics, and physical processes occurring in Mercury's

magnetosphere

Because the intrinsic magnetic field is weaker and the dynamic pressure of the so-
lar wind is stronger at Mercury than at Earth, solar wind can sometimes directly
interact with the dayside planetary surface in the low-latitude region. Recent MES-
SENGER observations indicate that the high dynamic pressure of the solar wind
causes the compression and magnetic flux transfer by reconnection, which can
completely erode the dayside magnetosphere (Slavin et al., 2019). Even when the
solar wind dynamic pressure is not so strong, the solar wind plasma can directly
penetrate until reaching the planetary surface through the cusp regions. Another
important characteristic of Mercury's magnetic field is the offset of the dipole. The
fly-bys by Mariner 10 suggested the possibility of northward offset of the magnetic
dipole by 0.2 R_M (Whang, 1977), which was confirmed by MESSENGER obser-
vations (Anderson et al., 2011). This means that the planetary magnetic field at
the surface is stronger at the northern pole than at the southern pole, and that
the solar wind plasma can more easily access the planetary surface in the southern
polar region. In addition, heavy ions and neutrals sputtered from the planetary
surface are major observation targets of MPPE. The effects of the direct inter-
action of the space plasma and the planetary surface on the remaining planetary
processes can be investigated only in Mercury's environment.

Despite the qualitative similarities of the global structures of the Mercury
and Earth magnetospheres, many differences remain between them. The small
dimensions of Mercury's magnetosphere imply short time scales of the dynamic

phenomena occurring therein. The magnetospheric convection, potentially driven by dayside reconnection, is expected to complete its circulation within just a few minutes, which is only 1/30 of the corresponding time scale at Earth (e.g., Slavin (2004)). Flux transfer events (FTEs) are frequently detected in rapid succession at Mercury's magnetopause with much shorter time scales than those at Earth (Slavin et al., 2012; Imber et al., 2014). The small magnetosphere also implies that kinetic behavior of plasma is particularly important. Because the typical scale of Mercury's magnetospheric structures are on the order of the proton Larmor radius, the ideal magnetohydrodynamics (MHD) approximation could be inadequate for describing the global dynamics of the magnetosphere. This is exemplified by MESSENGER observations, which showed that a typical proton gyroradius in Mercury's plasma sheet is $\sim$380 km (DiBraccio et al., 2015) and that the thickness of the plasma sheet is comparable to the proton gyroradius (Sun et al., 2017). For zero or weak guide magnetic fields, ion scale current sheets with a thickness comparable to the ion inertia length or the ion Larmor radius are predicted to become highly unstable for the current driven instabilities, which lead to quick triggering of magnetic reconnection (Shinohara and Fujimoto, 2005).

Many questions remain about the substorms in Mercury's magnetosphere. Because the concept of storage and sudden release of energy is likely universal, efforts to asnswer these questions enable us to examine the ubiquitous problems of magnetized plasmas. One of these questions is related to the dawn-dusk asymmetry in the plasma sheet associated with substorm activities (Sun et al., 2017). In particular, proton energization and heating through substorm activities occur more often on the dawnside than on the duskside, which is opposite that occurring in Earth's magnetosphere. The cause of the dawn-dusk asymmetry remains to be

studied using BepiColombo data. The questions related to the Mariner 10 observation events such as drift echoes have been considered in the context of substorms. These particle phenomena need to be studied with an unbiased attitude and a complete field of view. Specifically, all substorm-like events at Mercury should be studied in the context of solar wind-magnetosphere interaction and particle acceleration processes. In this context, measurements such as those by MPPE will be of paramount importance.

Recent theoretical studies suggest that efficient plasma transport can be achieved within highly rolled-up vortices that form owing to the velocity shear at the tail-flank boundary (Hasegawa et al., 2004; Nakamura et al., 2017). It is widely accepted that Kelvin-Helmholtz (K-H) instability operates at Earth's magnetopause and plays a significant role in transporting mass and energy from the solar wind to the magnetosphere. MESSENGER observations showed that K-H vortices develop predominantly on the duskside (Gershman et al., 2015). K-H waves as sources of these vortices are also detected mainly at dusk (Liljeblad et al., 2014). A possible contribution of heavy ions to K-H instability will be explored by analyzing the BepiColombo data.

The study of large amplitude electromagnetic waves around the magnetopause is also important in terms of particle transport, diffusion and acceleration. Anisotropic particle distribution and accelerated particle beams can excite various electromagnetic waves. The mapping of characteristic waves and particle velocity distribution functions, and their comparison with those found on other planets are also important.

The existence of Na ions in Mercury's magnetosphere is another interesting factor. The heavy mass of these ions combined with the weak magnetic field result in

large Larmor radii in the Mercury magnetosphere. The turbulence discussed here is basically of MHD nature but the large Larmor radius is comparable to the scale of the vortices and efficient heating of Na ions by turbulence is expected. Heated Na ions carry non-negligible pressure and thus play a role in determining the shape and dynamics of the magnetosphere (Gershman et al., 2014). Such a significant contribution of heavy ions would be an analog to large storms in Earth's magnetosphere although this could be the average state of the Mercury magnetosphere. Comprehensive observations of both the tail-flank turbulence and the large-scale convection powered by the reconnection in the small-scale magnetosphere are thus quite interesting from the perspectives of basic magnetohydrodynamics and magnetospheric physics. MPPE includes required plasma detectors with good time resolution and a mass spectrometer with sufficiently wide energy coverage.

The energization mechanism of magnetospheric plasma at Mercury has been unsolved since the Marinar 10 era. Although intense bursts of energetic charged particles >35 keV likely associated with substorm activities have been detected by Mariner 10 (Simpson et al., 1974), their species, flux, and energy spectrum for the events were not precisely determined owing to instrument limitations. Recent observations by EPS onboard MESSENGER revealed that the bursts of energetic charged particles are composed of high-energy electrons (Ho et al., 2011). This finding combined with the indications of MESSENGER/GRNS data suggest that the major components of the energetic bursts are electrons of several tens to $\sim$100 keV (Slavin et al., 2018). Although the most plausible mechanism of the electron energization is magnetic reconnection in Mercury's magnetotail associated with substorm activities, the lack of low-energy electron observations by MESSENGER prevents us from making a conclusion on this topic. However, observations of

electrons in a wide energy range by MPPE and other instruments will enable us to

identify the generation mechanisms of the high-energy electrons around Mercury.

2.2 Interaction among magnetosphere, exosphere, surface, and interior of Mercury

The Mercury environment can be characterized by complicated interaction among the surface, exosphere, and magnetosphere (Milillo et al., 2005). The lack of a thick atmosphere allows the space plasma to directly reach the surface. The surface materials are then ejected into space to form the exosphere, part of which is ionized and governed by the electro-magnetic environment of Mercury or magnetosphere. This complex system occurs in all objects in the Solar System with no atmosphere. In particular, the Moon provides an appropriate environment for understanding this coupling (e.g., Futaana et al. (2018)). Although it does not have a global magnetic field, the Moon's lacks of atmosphere and strong ionosphere affects the plasma-surface interaction, exosphere formation, and interaction with the upstream plasma. However, part of the Moon is magnetized where the dynamic plasma physics is in operation. Recent measurements of the Moon by several orbiters and fly-bys (e.g., Nozomi, Lunar Prospector, Kaguya, Chang'E, Chandrayaan-1, Artemis, and LADEE) have significantly increased our knowledge of the lunar environment, part of which can be applied to understand these interactions at Mercury.

Mercury's surface releases Na, O, H, He, K, Ca, and possibly other compositions by photon-stimulated desorption, thermal desorption, micrometeoric impacts, chemical sputtering, and ion sputtering, to form a highly extended tenuous

atmosphere or exosphere. The exosphere of Mercury will be investigated by instruments on MPO with a relatively lower orbiting altitude. However, the exospheric ions circulate along the convection of the magnetosphere and then partially re-enter Mercury's surface-exosphere system to further sputter the surface material. Conversely, the exospheric ions affect the magnetospheric convection. These facts indicate that Mercury's exosphere is not a single system, rather it strongly interacts with other regions, constituting a surface-exosphere-magnetosphere system. Among the release processes, ion sputtering is mostly related to magnetospheric processes. As a result of magnetospheric dynamics, the magnetospheric and solar wind ions precipitate on Mercury's surface resulting in atom and ion sputtering (Killen et al., 2001). The sputtered ions and exospheric photoions feed the magnetosphere, which affects its dynamics.

Ions originating directly from solar wind, those accelerated in the tail, and energized planetary ions, all precipitate onto Mercury's surface, which results in extensive sputtering (Grande, 1997; Wurz and Lammer, 2003; Mura et al., 2009). No reservoir of trapped particles exists near Mercury because the planet occupies a large portion of its inner magnetosphere; in this case, accelerated energetic particles hit the surface easily and become lost quickly (Delcourt et al., 2003; Yagi et al., 2017). The Mercury magnetosphere does not include a ring current region such as that present in Earth's inner magnetosphere which enables quasi-trapped Na ions to exist in the low-latitude region near the planet as indicated by simulation (Yagi et al., 2010) and MESSENGER observation (Schriver et al., 2011). The energetic particles in the magnetosphere should precipitate to the planetary surface/exosphere directly through pitch angle scattering by wave-particle interactions and field line curvature. The sputtering by particle precipitation is an escape

266 process of heavy ions from the planetary surface: the direct interaction of precipi-

267 tating particles with the planetary surface is important for the evolution of particle

268 circulation in the Mercury magnetosphere (Ip, 1986). Therefore, investigation of

269 the loss processes of high-energy particles and the relationship between the ener-

270 getic particle and the planetary surface is also an important objective of the MPPE

271 observations. The integrated energy spectrum of the sputtered products falls off

272 as E^{-2}, reflecting the Thompson-Sigmund formula (e.g., Sigmund et al. (1982))

273 and results in relatively high fluxes at energies greater than 10 - 100 eV (Massetti

274 et al., 2003). Measuring these low-energy neutral atoms (LENA) by MPPE-ENA

275 while monitoring precipitating ions by MPPE-MSA and MPPE-MIA are crucial

276 for understanding the contribution of sputtering to the formation of Mercury's

277 exosphere, which reveals dynamical and spatial variations of the sputtering source

278 (Fatemi et al., 2020).

279   In addition to magnetosphere-exosphere coupling, MESSENGER observation

280 revealed a possible magnetosphere-exosphere-interior system. The MESSENGER/MAG

281 observation provided evidence of field aligned currents (FACs) at Mercury, where

282 a weak Region 1 current system exists but no Region 2 current does (Anderson

283 et al., 2014). The existence of a Region 1 current system suggests the possibility

284 of electric current closure through conductive material at the depth of the outer

285 core, which strongly depends on the electric conductivity at the planet's surface

286 and interior region. Direct measurement of FAC carriers by MPPE is highly antic-

287 ipated. In addition, the balance between the magnetic reconnection and induction

288 at the dayside magnetopause could provide clues for understanding the planetary

289 interior (Heyner et al., 2016).

The dynamic response of the Mercury magnetosphere to solar wind variation is sometimes regarded as a possible explanation for the variability in the Na exosphere both spatially and temporally on timescales less than one day as observed by ground-based remote sensing measurement. Model calculations show that solar wind ions and the exospheric ions energized in the magnetosphere very non-uniformly affect Mercury's surface, which includes various impact regions such as auroral impact, cusp impact, and nose impact regions (Kallio and Janhunen, 2003; Delcourt et al., 2003). However, such calculations also indicate that the impact regions and the effects of ion flux are rather sensitive to the magnetospheric dynamics and particle environment. MESSENGER discovered an X-ray aurora accompanied by electron precipitation (Lindsay et al., 2016; Dewey et al., 2017). Observation of precipitating electrons by MPPE-MEA and MPPE-HEP-ele will also contribute to understading the magnetosphere-exosphere coupling.

The highly eccentric orbit of Mercury generates significant variation in the planetary environment between the perihelion and aphelion. Recent MESSENGER observations have shown that the Na exosphere is surprisingly constant in terms of annual variation, with no strong episodic variation or surface dependence noted (Cassidy et al., 2015). However, the Na intensity showed a strong seasonal variation that contradicts previous ground-based observation reported by Leblanc and Johnson (2010). The ionization frequencies of the exospheric neutrals by photoionization, electron impact ionization, and charge exchange interaction, which depend on the solar flux and the solar wind density and velocity, vary by a factor of two. These differences can cause a significant alteration of the dynamics of Mercury's magnetosphere-exosphere-surface-interior system. To understand this

system, it is necessary to observe the planet's particle environment by MPPE

observation for at least a few Mercury years.

2.3 Shocks and the inner heliosphere

A new era of inner heliosphere exploration began with the launch of the Parker

Solar Probe in 2018 (Fox et al., 2016), followed by that of the Solar Orbiter in

2020 (Müller et al., 2013). Mio will play an important role in this heliosphere-

wide, multi-mission exploration by its placement in Mercury's orbit. Following the

successes of other missions such as Helios 1 and 2 in the 1980s, MESSENGER

in 2008 - 2015, and the recent Parker Solar Probe, Mio is expected to achieve

comprehensive in-situ measurement of plasmas in the inner-heliosphere by taking

advantage of the spin-stabilized configuration of the spacecraft and a suite of

modern instruments. Mio is expected to make a wide range of discoveries regarding

collisionless shocks, solar wind, pickup ions of interstellar-origin, solar energetic

particles (SEPs), the modulation of galactic cosmic rays and other phenomena.

Particles are accelerated to very high, non-thermal energies at astrophysical

shocks, as evidenced by emission from astrophysical sources such as supernova

remnants, extragalactic jets, and galaxy clusters. Particles are also accelerated

at shocks in space such as planetary bow shocks and interplanetary shocks. In-

situ measurement of shocks in various plasma environments is thus crucial for

understanding of the generality and scaling-law of particle acceleration at shocks.

Mercury is unique in that it is closer than any other planet to the sun. Thus

its orbit offers the greatest chance of detecting very fast interplanetary shocks

particularly in extreme cases of solar eruptive events such as coronal mass ejection

(CME) and solar flares. The shock speed can reach up to 4000 km/s and the Alfvén Mach number can exceed several tens in value, as demonstrated combined observations and modeling (Smart and Shea, 1985; Cliver et al., 1990). In fact, statistical analysis of MESSENGER data has confirmed that the shock transit speed is substantially higher in Mercury's orbit (Winslow et al., 2015) than that of Earth, which is consistent with earlier reports (Wang et al., 2005). Therefore, MPPE data combined with information obtained from other instruments on Mio will likely provide opportunities to study high-speed and/or high-Mach-number shocks well before they are substantially decelerated.

A key point in this research is that previously observed features of particle acceleration at shocks are often inconsistent with the standard diffusive shock acceleration (DSA) scenario. In DSA, the particle flux increases exponentially prior to the arrival of the shock, reaches its maximum at the shock front, and exhibits a power law with the power-law index as a function of the compression ratio only. In reality, however, shocks often do not exhibit a significant flux increase and, even if they are present, the power-law index does not match that predicted from the observed compression ratio. Such discrepancies have been reported for both ion acceleration (e.g., van Nes et al. (1984); Lario et al. (2003); Desai et al. (2004); Lario (2005); Fisk and Gloeckler (2012)) and electron acceleration (Shimada et al., 1998; Ho et al., 2008). Moreover, for electrons, pre-energizing to non-thermal energies is required for the DSA process to begin, although the precise mechanism of such a process remains unclear (e.g., Tsurutani and Lin (1985); Oka et al. (2019); Amano et al. (2020)). To address these problems, MPPE will provide comprehensive analyses of ion/electron velocity and pitch-angle distributions, associated

waves and turbulence, ion composition, and ion charge states before, during and after shock/CME passages.

The bow shock and magnetosheath signatures in Mercury's orbit are important targets of BepiColombo. The solar wind flow in Earth's orbit is usually super-Alfvénic with typical Alfvén Mach numbers of $5 < M_A < 10$. According to the standard solar wind model by Parker (1958), the Alfvén Mach number in Mercury's orbit is statistically lower than that in Earth's orbit (e.g., Slavin et al. (2018)). We expect to detect super-Alfvénic solar wind with very low M_A ($1 < M_A < 2$) and sub-Alfvénic solar wind ($M_A < 1$) in Mercury's orbit because BepiColombo will arrive at Mercury in 2025 when the solar activity is likely to be at its peak in Solar Cycle 25. For the bow shock under the lower but still super-Alfvénic solar wind ($M_A > 1$), the MESSENGER mission has already revealed significantly smaller magnetic "overshoots" (i.e., intensifications of the magnetic field magnitude within the shock transition layer) at Mercury's bow shock compared with that at Saturn (Masters et al., 2014). The differences in overshoot structure of the bow shocks is consistent with the expectations, which demonstrats the applicability of the scaling law based on the solar wind model. In addition, the lower M_A solar wind yields unusual interaction between the magnetosheath and the magnetosphere, that depends strongly on the direction of the interplanetary magnetic field (IMF) (Lavraud and Borovsky, 2008; Nishino et al., 2008). If the solar wind becomes sub-Alfvénic, the bow shock will alter to a slow-mode shock, and its shape and structure could differ significantly from that normally expected for a fast-mode bow shock (Hundhausen et al., 1987). An irregular bow shock can be detected by comparing the data with the typical shape/location of the bow shock established by MESSENGER (Winslow et al., 2013). Another candidate for sub-

Alfvénic interaction of Mercury's magnetosphere with the extreme solar wind is the formation of Alfvén wings (Sarantos and Slavin, 2009), which can be compared with sub-Alfvénic interaction of the Galilean moons with Jupiter's magnetosphere.

3 Instrument Description and Pre-flight Calibration

3.1 Overview of MPPE Instrument Suite

3.1.1 MPPE Instrument Suite for Plasma/Particle Measurements

As illustrated in Figure 1, the MPPE suite is a comprehensive instrument package developed to achieve the scientific objectives described in section 2. As previously discussed, it consists of seven sensors including MEA1, MEA2, MIA, MSA, HEP-ele, HEP-ion, and ENA (Saito et al., 2010a). These sensors measure plasma, high-energy particles and energetic neutral atoms with sufficiently high time resolution, wide energy and dynamic ranges, wide angle coverage, and high mass resolution.

Specifically, MEA1 and MEA2 measure the 3D phase space density of low energy electrons between 3 eV and 26 keV and were developed by the Research Institute in Astrophysics and Planetology (IRAP) in France. MIA measures 3D phase space density of low energy ions between 15 eV/q and 29 keV/q and was developed by ISAS/JAXA in Japan. MSA measures the mass identified 3D phase space density of low energy ions between 1 eV/q and 38 keV/q and was developed by the Laboratory of Plasma Physics (LPP) in France, the Max Planck Institute for Solar System Research (MPS) and Institute of Computer and Network Engineering (IDA)/Technical University of Braunschweig in Germany and ISAS/JAXA in Japan. HEP-ele and HEP-ion measure the energy spectra of high energy elec-

408 trons between 30 keV and 700 keV and the mass identified ion energy spectra of

409 high energy ions between 30 keV and 1.5 MeV, respectively, and were developed

410 by Institute for Space-Earth Environmental Research (ISEE)/Nagoya University

411 and ISAS/JAXA in Japan. ENA measures the mass identified energetic neutral

412 atoms between 10 eV and 3.3 keV and was developed by the Swedish Institute

413 of Space Physics (IRF)-Kiruna in Sweden, University of Bern in Switzerland and

414 ISAS/JAXA in Japan.

415   Figure 2 shows the locations of the MPPE sensors on Mio. The four low-

416 energy sensors MEA1, MEA2, MIA, and MSA are referred to as low-energy particle

417 (LEP) sensors. The LEP sensors have ring shaped FOVs in which the center axis is

418 perpendicular to the spin axis of the spinning Mio spacecraft. The LEP sensors are

419 installed on the four diagonal corners of the octagonal Mio spacecraft to minimize

420 the interference of the spacecraft body in measuring low energy charged particles.

421 MEA1 and MEA2, the two electron sensors, and MIA and MSA, the two ion

422 sensors, are installed $90°$ apart to fulfill the requirements of the high time resolution

423 measurements. The other MPPE sensors, including HEP-ion, HEP-ele and ENA

424 are installed on the side panels of the Mio spacecraft. HEP-ion has a conical FOV,

425 whereas HEP-ele and ENA have radial FOVs. To minimize the thermal input

426 under the severe thermal conditions of Mercury's orbit, all the MPPE sensors

427 are equipped with individual thermal shields in which the surface is coated with

428 electrically conductive white paint.

429   A commonly used data processor Mission Data Processor 1 (MDP1) (Kasaba

430 et al., 2020) controls all of the MPPE sensors and is responsible for processing

431 the data sent from them. In addition, it formats the telemetry data, calculates

432 the velocity moments (VMs), and reduces the quantity of data by adding, select-

ing, or compressing the data. Depending on the total telemetry rate of the Mio

spacecraft, three different data rates of high, medium, and low are defined. The

MPPE sensors are allocated to 72.5, 5.5, and 0.8 kbps as high, medium, and low

data rates, reflected by H-mode, M-mode, and L-mode, respectively. The L-mode

data are continuously available during the orbital period of about 9.4 h. The LEP

sensors produce VMs of electrons and ions (density, velocity, temperature), and

compressed E-t spectrograms with limited angle, mass, energy, and time resolu-

tion as L-mode data. The HEP sensors also produce count data with limited angle,

mass, and energy resolution as L-mode data. ENA produces only L-mode data.

The M-mode data are available during only about 25% of the entire observation

period. The LEP and HEP sensors produce 3D counts with selected angle and time

resolution or 2D counts as M-mode data. Although full 3D counts are produced

as H-mode data, this mode is available only during limited periods.

3.2 MEA

3.2.1 Instrument Description of MEA

The MEA instrument is composed of two sensors MEA1 and MEA2, which com-

bine the selection of incoming electrons according to their energies by electrostatic

deflection in symmetrical toroidal analyzers. These instruments provide a uniform

angle energy response with a fast imaging particle detection system (Sauvaud

et al., 2010). MEA2 is illustrated in Figure 3. One of the key and novel features

of the MEA sensors is the implementation of an electronic device that enables

the geometrical factor (G-factor) to vary by a factor of 1000 in the top-hat elec-

trostatic analyzer to measure the solar wind and magnetospheric electron fluxes within more than six decades.

Figure 4 illustrates the identical electron optic design of MEA1 and MEA2 except for the entrance aperture, which is discussed subsquently. The electrostatic analyzer (ESA) consists of a $95°$ toroidal deflector with two concentric electrodes and a spherical top section. Whereas the outer electrode and the top-hat are at signal ground, the two parts of the inner electrode can be set at the same voltage (Uan = Utop) as for a classical top-hat analyzer with an analyzer constant k = E/V = 9.6. When the central part of the inner electrode (Utop) is biased with voltages lower than those applied to the toroidal part (Uan), the energy and angular acceptance are both reduced leading reduction of the G-factor.

Figure 5 shows the microchannel plate (MCP) in a chevron stack configuration, which are used to multiply the incident electrons. Figure 6 shows the 16 discrete anodes of $22.5°$ each of which is used for position encoding that are connected to amplifiers/discriminators followed by Amptek A111F counters with a detection threshold of 10^5 electrons.

Figure 7 shows the entrance of the electrostatic analyzer of MEA, which includes four baffles for reducing the penetration of ultraviolet light (UV) in the hemispherical spheres. The generation of photoelectrons inside the instrument is further limited by the use of golden, polished parts that also serve to decrease the heat flux into the instrument.

Figure 8 illustrates the use of scalloping on the outer and inner plates of the toroidal deflector and the top-hat, for reducing the transmission of secondary electrons and UV photons. The analyzer plates are further coated with Cu_2S black to efficiently absorb stray light, as obtained from Collini (https://www.collini.eu).

480   Figure 9 shows the high voltage board which provides two sweeping voltages

481 of 0 - 3000 V for the analyzer, and a static power supply from 0 - 3400 V for the

482 MCPs. To select the energy of incident electrons, we vary the deflection voltages

483 of the inner plates of the electrostatic analyzer logarithmically with 128 equally

484 spaced steps in synchronization with the spacecraft spin period. MEA measures

485 the full 4π electron distributions with a single analyzer in 1/2 of the spacecraft

486 spin period or with the two analyzers in 1/4 of the period.

487   Figure 10 shows the field-programmable gate array (FPGA) board with two Ac-

488 tel RT54SX72SU components used to control all functionalities of the instrument.

489 The first controls the sensor head and accumulates the counting rates, and the

490 second transmits/receives data/commands from the data processing unit (MDP1)

491 shared by all MPPE instruments using the spacewire protocol.

492   A multi-layer insulator (Figure 11) and a thermal shield (Figure 12) coated

493 with white paint are used to ensure the thermal protection of the sensors. The

494 peak temperatures near Mercury reach 140°C on the thermal shield, 85°C on the

495 spheres, and 60°C on the MCPs and electronic boards when operating.

496   Table 1 summarizes the key parameters of the MEA sensors, and Figure 13

497 shows a block diagram of the instrument.

498 *3.2.2 Operation Mode and Data Products of MEA*

499 MEA includes versatile and easily programmable operating modes and data pro-

500 cessing routines for optimizing the data collection for specific scientific studies

501 and widely varying plasma regimes. Depending on the telemetry mode, MEA can

502 transmit several MDP1 data products, including those listed below.

503   1. Electron omnidirectional fluxes (Et-OMN).

2. Electron VM. The instrument transmits the temperature, heat flux vector, and number density calculated in several energy bands. The position of the boundaries of each energy band is defined by commands.

3. Electron pitch angle distribution for four selected energies (Et-PAP). MEA uses the magnetic field vector as the external input for this mode and transmits the 2D angle-energy distribution.

4. Full 3D electron distribution. The instrument transmits a complete angular-energy spectrum accumulated for a minimum of 1/4 of the spacecraft spin.

MEA uses different energy tables to adapt to the various space environment conditions encountered by the Mio spacecraft. The choice of energy table used is defined by commands. The four energy tables available for MEA include

1. 3–300 eV

2. 3-25000 eV

3. 3-3000 eV

4. 3000-25000 eV

In addition, MEA has unique data modes that can be defined by commands, depending on the number of channels (16 or 32) and energies (16, 32 or 64).

Table 2 shows the various MPPE data mode names and the corresponding data products of MEA1 and MEA2 together with the time resolution depending on the telemetry mode of the Mio spacecraft. Tables 3, 4, and 5 detail the properties of MEA data products for each Mio telemetry mode.

All MEA data products will be available in Common Data Format (CDF, https://cdf.gsfc.nasa.gov) files.

3.2.3 Pre-Flight Calibration of MEA

The calibration of the two MEA sensors and a flight spare model was conducted at the IRAP Toulouse vacuum facilities. The parameters shown in Table 6 will be used to describe the various calibration setups, procedures, and results.

The pre-flight calibration of the MEA sensors consisted of full calibration of the sensors, the characterization of the MCP detectors of the sensors, and sensor testing for UV contamination. To derive the calibration parameters for a configuration as close as possible to that of the sensors in space, full calibration was performed with a realistic simulator of the instrument thermal shield and with the magnetic field of Earth inside the vacuum chamber compensated by Helmholtz coils. Figure 14 shows the MEA1 sensor installed in the setup and its simulator for the thermal shield, the beam monitor, and the magnetometer, which continuously measures the residual magnetic field in the vicinity of the sensor. The measurements of the magnetometer are automatically used to adjust the residual magnetic field below a maximum value of 0.5 μT. For each calibration step, absolute measurements of the properties of the employed electron beam were taken.

The counts for each MCP anode as a function of MCP HV are shown in Figure 15. The working point of both MCP detectors for MEA1 and MEA2 was set to 2750 V as delineated by the red vertical line in the figure. The working point is defined here by the bias voltage applied to the MCP needed for reaching a plateau in the MCP counts.

The UV contamination test results are shown in Figure 16. The strong count at the small energies show the photoelectrons emitted inside the instrument and

550 the vacuum chamber. The maximal background was less than 1 per second per

551 anode.

552   Full calibration of the MEA1 and MEA2 sensors was conducted in the coordi-

553 nate frame shown in Figure 17. The electron beam properties are given below.

554 − For each azimuth angle Φ, a scan was made over elevation angle Θ.

555 − For each angular position, the set of G-factors was tested.

556 − For each value of G-factor, the analyzer voltage was scanned.

557   Figures 18 and 19 show the energy, elevation and azimuthal responses for

558 different anodes and G-factor levels. The dashed curves in these plots show the

559 polynomial fit that enabled definition of $\Delta E/E$ and $\Delta\Omega$ with high accuracy. When

560 the central part of the inner electrode (Utop) is biased with voltages lower than

561 those applied to the toroidal part (Uan), the analyzer accepts particles coming from

562 a slightly higher azimuth. The energy and angular acceptance are both reduced

563 leading to a reduction of the G-factor. The G-factor for each anode versus the value

564 of Utop/Uan is shown in Figure 20, where the theoretical profile obtained from

565 the numerical simulation is represented by a dashed curve. MEA2 has a maximum

566 GF0/GF ratio of 1000, whereas that of MEA1 is only 60 because it includes a

567 grid attenuator with 5% transparency at its entrance. Table 7 summarizes the

568 calibration results for MEA1 and MEA2.

569 *3.2.4 Near-Earth Commissioning Results of MEA*

570 On July 1 and 2, 2019, the two MEA sensors were turned on, respectively, when

571 the BepiColombo spacecraft was about 29 million km from Earth. MEA1 and

572 MEA2 have perfectly responded to our commands up to their nominal working

573 point of 2750 V applied to their MCPs. Hence, the very first electron spectra

574 in the solar wind have been successfully obtained, even though Mio is behind

575 the MOSIF thermal shield. Figures 21 and 22 show the MEA1 and MEA2 data,

576 respectively. The solar wind electron moments were estimated from MEA1 3D

577 data after noise removal (Figure 23). The density calculated from the MEA1 data

578 when integrated over all energies, including both core and halo (above 100 eV)

579 solar wind electrons (1.9 cm^{-3}), and the first eleven energies for the core solar

580 wind electrons (0.9 cm^{-3}), and the temperature (13 eV), agree well with expected

581 values at the location of the Mio spacecraft as well as those with a Maxwellian

582 distribution with a density of 0.6 cm^{-3} and temperature of 10 eV.

583   The very first data obtained during the near-Earth orbit phase commissioning

584 of the MEA instrument confirm that both MEA1 and ME2 are working normally.

585 In the near future the MEA instrument will be turned on again during Earth,

586 Venus, and Mercury fly-bys and during the cruise phase to enable multipoint

587 measurements of electrons in the solar wind together with electron spectrometers

588 onboard the Solar Orbiter and Parker Solar Probe missions.

589 3.3 MIA

590 *3.3.1 Instrument Description of MIA*

591 MIA as shown in Figure 24 was developed to understand the structure and plasma

592 dynamics of Mercury's magnetosphere; Mercury – solar wind interaction; atmo-

593 spheric abundances, structures, and generation/loss processes; and the solar wind

594 between 0.3 and 0.47 AU (Miyake et al., 2009). To achieve these research objec-

595 tives, MIA should be able to measure both the 3D distribution function of solar

596 wind ions around Mercury (0.3 – 0.47 AU) and the planet's magnetospheric ions.

597 Figure 25 shows a block diagram of MIA, which consists of the (A)spacecraft

598 interface board, (B)positive high volatge board, (C)negative high voltage board,

599 and (D)analyzer. As shown in Figure 25(D), MIA is a top-hat type electrostatic

600 analyzer with toroidal deflectors (Saito et al., 2010a). Figure 26 shows the "top-

601 cap" and upper part of the entrance collimator (panel (a)) and inner sphere and

602 lower part of the entrance collimator (panel (b)). The surface of the analyzer is

603 gold plated or blackened by copper sulfide black. The blackening process "Ul-

604 traviolet Absorbing Black plating" was developed by Mitsuya Co. Ltd. in Japan

605 (https://www.mitsuya-plating.com). In addition, the inner and outer spheres are

606 serrated with the tip-to-root length and tip angle of the sawtooth serrations at 0.5

607 mm and $60°$, and the light traps are placed at the top part of the outer sphere to

608 minimize the solar UV entering the detector(MCP). MIA measures 3D ion distri-

609 bution function utilizing the spin motion of the spacecraft. The diameters of the

610 inner and outer toroidal electrodes are 32 mm and 35 mm, respectively, with the

611 center shifted 5mm toward the radial direction. The resultant analyzer constant

612 is 5.66.

613   Stepping high voltage between 0 V and -5 kV is applied to the inner toroidal

614 electrode. Figure 27 shows the spacecraft interface board. On the rear side (panel

615 (a)), two MDM connectors are shown including a 9-pin checkout connector and

616 a 25-pin SpaceWire/power supply interface connector. On the front side (panel

617 (b)), two Hypertac connectors are placed including one connected to the high

618 voltage boards and the other connected to the application specific integrated cir-

619 cuit (ASIC) on the MCP anode. Figure 28 shows the negative high voltage board

620 installed in the chassis of MIA (Figure 25(C)). Among the three electronics boards

621 (Figure 25(A)-(C)) shielding plates are installed to reduce the electrical noise and

622 the risk of electrical discharge among the electronics boards. Ions enter the ana-

623 lyzer by passing through the collimator and are attracted down toward the inner

624 electrode by receiving Coulomb force from the electric field between the "top-cap"

625 and the inner electrode. Ions with specific energy ranges determined by the high

626 voltage applied to the inner electrode can pass through the troidal analyzer, enter

627 the Z-stack MCP and become multiplied to generate detectable amounts of charge

628 clouds. A grid having the same voltage as the input surface of the MCP is placed

629 between the MCP and the troidal analyzer.

630 The charge clouds from the MCP are detected by a 63-channel discrete anode

631 (Saito et al., 2017). The incident azimuthal directions of the ions correspond to

632 the positions at which the charge clouds are detected. The detected charge clouds

633 are fed into a newly developed ASIC of which the bare chip is installed at the back

634 side of the discrete MCP anode. The ASIC consists of 64-channel discriminators,

635 64-channel fast preamplifiers, and 64-channel counters (Saito et al., 2017).

636 MIA should measure both intense solar wind ions and tenuous Mercury magne-

637 tospheric ions. Therefore, the required dynamic range for detecting low-energy ion

638 flux is as wide as 10^6 (Mukai et al., 2004). To measure both solar wind ions with-

639 out saturation and Mercury magnetospheric ions with sufficient counting statistics,

640 MIA includes an attenuation grid with 10% transmission placed at limited chan-

641 nels (one of the two $\pm 60°$ angular ranges centered at the spin plane) of the entrance

642 part of the analyzer. Figure 29 shows a schematic diagram of the attenuation grid

643 pattern.

644 In addition, MIA includes a function for reducing the geometrical factor elec-

645 trically for solar wind ion measurement. The sensitivity of the analyzer can be

reduced by applying positive high voltage to the "top-cap" insulated from the surrounding structures. By applying stepping high voltage between 0 V and +5 kV and synchronizing with the inner sphere voltage, the G-factor can be reduced to ∼1/50 (Miyake et al., 2009).

To reduce the strong thermal input to MIA on Mercury orbit, MIA is equipped with its own thermal shield (Figure 30). The thermal shield is composed of titanium and the surface is painted with electrically conductive white paint.

According to our knowledge of Earth's magnetosphere, full 3D measurements of low-energy ions with high time resolution are indispensable for understanding the structure and dynamics of the magnetosphere. Because no full 3D low-energy ion data have been obtained around Mercury, the low-energy ion data obtained by MIA together with MSA on Mio will provide unique opportunity for understanding the detailed structure and dynamics of the Mercury magnetosphere.

3.3.2 Operation Mode and Data Products of MIA

After its insertion into Mercury's orbit, MIA will continue its observation during all orbital phases except for periods in which MIA should be turned off owing to thermal/power constraints. Because the operation of all science instruments on Mio should be synchronized, the scientific operation of MIA obeys that of the Mio instrument suite. MIA has three operational modes: solar wind (SW), magnetospheric ion high angular resolution (MIHAR), and magnetospheric ion low angular resolution (MILAR) modes. The SW mode is used for fine angular resolution measurement of the solar wind around Mercury; the MIHAR mode is used for high angular resolution measurements of the Mercury magnetospheric ions; and the MILAR mode is used for low angular resolution measurements of the

670 Mercury magnetospheric ions. These modes are changed depending on the satellite

671 position and telemetry data rate by real-time commanding or stored commands.

672 The MDP1 onboard software can also be used to change the mode. Table 8 shows

673 the MIA operation mode and the data rate sent from MIA to MDP1. MIA always

674 acquires data with a fixed sampling time of ∼2 ms, a fixed spin angular sector of

675 5.625° (64 equally divided spin sectors: 360°/64 sectors = 5.625°), and 64 ASIC

676 channels. The 64 ASIC channels are connected to the 62-channel discrete anode

677 that detects the position of the energy analyzed ions and an annular anode that is

678 used for monitoring the high-energy particle background (Saito et al., 2017). One

679 ASIC channel is left open to monitor the electrical background noise (Figure 36).

680 Therefore MIA always acquires 64 channels × 64 spin sectors × 32 energy steps

681 = 131072 data for 1 spin.

682   Since this data quantity is too large for processing by MDP1, the FPGA in

683 MIA will add adjacent counts (spin sectors and ASIC channels) depending on

684 the MIA's data mode (modes 0, 1 and 2). The data sent from MIA to MDP1

685 are processed by MDP1 and the telemetry data are transmitted to the ground

686 according to the MPPE data mode described in Section 4.

687   Table 9 shows six different MIA energy sweep modes. Mode 0 and 1 are used

688 mainly for solar wind ion observation. The energy range between ∼100 eV/q and

689 ∼10 keV/q is exponentially divided into 128 energy steps. To cover the full energy

690 range, four spin-periods (nominally 16 s) are necessary. The difference between

691 energy sweep modes 0 and 1 is that the sensitivity control function is either OFF

692 or ON. For mode 1, the sensitivity is controlled by applying positive high voltage

693 to the "top-cap" to reduce the G-factor. Energy sweep mode 2 is referred to as the

694 MCP protection mode, which is used for protecting part of the MCP that detects

ions from the analyzer azimuthal sector with no mechanical attenuation grid. The energy range is determined not to measure intense main component of the solar wind. Energy sweep modes 3, 4, and 5 are used mainly for magnetospheric ion observation. Energy sweep mode 3 is a "wide energy range mode" that covers the full energy range between ∼20 eV/q and ∼25 keV/q with 32 exponentially divided steps. Energy sweep mode 4 is a low energy range mode that covers the low energy range between ∼20 eV/q and ∼5 keV/q with 32 exponentially divided steps. Energy sweep mode 5 is a high energy range mode that covers the high-energy range between ∼5 keV/q and ∼25 keV/q with 32 exponentially divided steps. Different energy sweep modes can be selected for eight spin sector groups, where spin sector group 0 is from spin sector 0 to 7, group 1 is from spin sector 8 to 15,..., and group 7 is from spin sector 56 to 63. Spin sector 0 occurs when the axis of rotational symmetry of MIA is pointing away from the Sun (Figure 31). In this case, the solar wind channel with the mechanical attenuation grid observes solar wind at spin sector groups 1 and 2. Table 10 shows examples of the energy sweep mode allocated to the spin sector group. Numbers from 0 to 5 in the "waveform allocation" correspond to energy sweep modes 0 to 5 in Table 9.

The energy sweep of MIA is as follows: (1) 1 spin (4 s) is equally divided into 64 spin angle sectors; (2) 32 energy steps are swept in each spin angle sector resulting in a sampling time of 4 s/64 spin sectors/32 energy steps = ∼2 ms); and (3) 128 energy steps are swept by accumulating 4-spin sets of 32 energy steps/spin. Figure 32 (left) shows an energy sweep waveform of MIA, specifically the voltage applied to the inner sphere for solar wind observation (energy sweep mode 0 or 1). In the solar wind, 4 spins are necessary to cover the full energy range with 128 steps. The full energy range with 32 steps is covered in each spin (energy coverage has

some gaps). In this case, 32 steps in 4 different spins are slightly shifted so that 64 energy steps are covered with 2 consecutive spins, and 128 energy steps are covered with 4 consecutive spins. Concerning the attenuation factor, only one pre-defined "top-cap" voltage/inner sphere voltage ratio ($V_t/|V_i| = 1.0$) is used because the G-factor varies too rapidly when the ratio exceeds 1.0. When we use energy sweep mode 1, the attenuation is applied to all energy steps to reduce the flux of the solar wind ions. Figure 32 (right) shows the voltage applied to the inner sphere and the "top-cap" for solar wind observation (energy sweep mode 1). Electrical attenuation is enabled by applying the same voltage to the inner sphere and the "top-cap".

According to the MIA mode (modes 1-3; Table 8), the MIA application in the MDP1 continuously computes the VM data and energy spectra (Et) for the mission packets of the L-mode, whereas medium-resolution 3D distribution functions (3D-L2 or SW-L2) are generated for the M-mode. The L-mode mission packets also contain 3D distribution functions (3D-LL), although they are provided in long intervals of (600-3600 s) (Table 11). For the H-mode mission packets, high-resolution 3D distribution functions (SW-L, 3D-L2, or 3D-H) are generated each spin (4 s). The VM consists of the density (n), net flux vector (nV), and pressure tensor (P), which are computed using a lookup table. The detailed format, size and rate of each data product shown in Table 11 are shown in Table 12. For the 3D count data products in the M-mode mission packets, 3D-L2-M1 and 3D-L2-M3, and in the H-mode mission packets, 3D-L2-M1, 89 directions (DIR) are selected from eight spin sectors (SC) $\times 17$ channel (CH) directions. The VM consists of density n; net flux vectors nVx, nVy, nVz; and pressure tensors Pxx, Pyy, Pzz, Pxy, Pyz, Pxz. EN in the table represents energy.

3.3.3 Pre-Flight Calibration of MIA

Pre-flight calibration of the MIA sensor was performed at a calibration facility at the Institute of Space and Astronautical Science/Japan Aerospace Exploration Agency (Wüest et al., 2007). MIA was installed in a vacuum chamber and nitrogen ions were injected. Figure 33 shows schematic diagram of the calibration experiment configuration. The sensor under calibration was installed on a rotation table 1, which had a rotation axis parallel to the sensor's axis of rotational symmetry. This rotation table was installed on another rotation table rotation table 2 in which the rotarion axis was perpendicular to both the beam line and the rotation axis of rotation table 1. Most of the data were obtained using 6 keV nitrogen ion beams because the beam profile was uniform and stable.

Table 13 gives a summary of MIA performance data determined by pre-flight calibration. The definition for the quantities in this table is general and is the same as that used by Wüest et al. (2007). Figure 34(a) and (b) compares the E-α characteristics of MIA with and without electrical attenuation. When electrical attenuation is enabled, both the angular spread and energy spread become narrower and the measured ion energy increases. Since angular resolution and energy resolution become higher, electrical attenuation is appropriate for solar wind ion observation. The G-factor is reduced to about 1/50 where the mechanical attenuation grid is installed. Figure 34(b) and (c) compares the E-α characteristics of MIA with and without a mechanical attenuation grid. It is clear that part of the E-α contour with large α angle is reduced by the mechanical attenuation grid. Because the attenuation grid is placed only at the bottom part of the entrance aperture and the upper part is closed as shown in Figure 29, the ions entering

MIA with large α angles are blocked. Consequently, the center of the measured α angle becomes smaller and that of the measured energy becomes lower compared to those without a mechanical attenuation grid.

Figure 35(a) shows the θ (azimuthal angle) resolution of MIA. The θ angle coverage of all anode channels are shown when electrical attenuation is OFF (left panel) and ON (right panel). It is clear that the sensitivity is reduced where the mechanical attenuation grid is installed at the entarance of the analyzer (CH38 – CH57). Figure 35(b) and (c) shows the θ angle coverage in greater detail. When the electrical attenuation is ON (panel (c)), the θ angular resolution becomes much higher than that when the electrical attenuation OFF (panel (b)).

Figure 36 shows the G-factor of MIA for all 64 channels. MIA has physical supports across the entrance aperture every $120°$. The light and thick blue boxes indicate the channels affected by these physical supports (CH15, CH16, CH36, CH37, CH58 and CH59). The G-factor is reduced to about 1/50 where the mechanical attenuation grid is installed (CH38 – CH57). Although the geometrical attenuation factor of the mechanical grid is 1/10 (Figure 29(c)), the G-factor reduction is $\sim$1/50 because the mechanical grid also changes the angular and energy characteristics of MIA as shown in Figure 34. Slight variation of the G-factor also exists among the different channels without the mechanical attenuation grid with large values around CH0 and small values around CH31. The variation of the analyzer constant was also occurred simultaneously with the variation of the G-factor. This variation can be explained by the slight inclination of the inner sphere with respect to the outer sphere where the inclination angle was as small as $0.2°$ that is within the manufacturing tolerance.

3.3.4 Near-Earth Commissioning Results of MIA

The low voltage part of MIA was turned on for the first time on November 25, 2018, about one month after the launch. No problems were identified during the low voltage function tests, which included calibration pulse injection into all channels of the pre-amplifier.

The high voltage tests were performed on July 3 and 4, 2019, about eight months after the launch when Mio was in the solar wind. High voltage up to +2500 V, -3610 V, and -2471 V were successfully tested for stepping high voltage power supply connected to the "top-cap" (SVG), stepping high voltage power supply connected to the inner sphere (SVS), and high voltage power supply connected to the MCP detector (MHV), respectively. Dark counts of the MCP were observed indicating that the detector part of MIA was functioning normally. Because Mio is surrounded by the MMO Sunshield and Interface Structure (MOSIF) during the cruise phase, most parts of the MIA's FOV is blocked by MOSIF. Although all of the high voltage necessary for observation were successfully applied to MIA, no solar wind ion signature was observed because the solar wind ion thermal velocity was much lower than its bulk velocity, and MOSIF blocked the solar wind ions to enter MIA.

Because MIA is able to measure hot plasmas in the magnetospheres of Earth and Mercury and near-Venus when the plasma thermal velocity is higher than its bulk velocity, MIA will be turned on during the Earth fly-by and the Venus/Mercury fly-bys before arriving at Mercury in December 2025.

3.4 MSA

3.4.1 Instrument Description of MSA

MSA, part of the MPPE particle consortium, is dedicated to plasma composition measurement onboard Mio (Delcourt et al., 2016). The main objectives of this instrument are (1) to study the role and efficiency of the solar wind and planetary surface as sources of plasma for the Hermean magnetosphere; (2) to study the transport, acceleration and loss of plasma in the Hermean magnetosphere, particularly for investigating the dynamics of heavy ions of planetary origin that have large gyroradii and large gyroperiods as compared to the characteristic scales of the magnetosphere; (3) to contribute to the understanding of magnetosphere electrodynamics, substorms, and the nature of current carriers; (4) to analyze the interaction of magnetospheric plasma with the planetary surface and to study the processes by which particles escape from the surface and access the magnetosphere; (5) to provide data that will help to identify Mercury's surface composition; (6) to monitor the solar wind and to study interstellar pick-up ions. To achieve these issues, MSA will provide 3D distribution functions in one Mio spin (4 s). In addition, in contrast to Earth where ions of planetary origin are essentially O^+ and He^+, a wide variety of species populate Mercury's magnetosphere owing to various interaction processes with the planet surface (such as solar wind sputtering, micro-meteoritic bombardment, and thermal desorption). To characterize these populations, a spectrometer with enhanced mass resolution capability is necessary; hence, the "reflectron" design was adopted for MSA.

As summarized in Figure 37, MSA is the result of collaboration of four different teams : (1) ISAS (Sagamihara, Japan; PI), which provided the amplifier board

and spacewire interface; (2) LPP (Palaiseau, France; Co-PI), which provided the

electrostatic optics; (3) MPS (Göttingen, Germany), which provided the high volt-

age power supplies; and (4) IDA (Braunschweig, Germany), which provided the

dedicated central processing unit (CPU) board. A block diagram of MSA is shown

in Figure 38. MSA has dimensions of 325 mm × 287 mm × 232 mm, a weight of

4.46 kg, and medium telemetry mode power of 9.1 W.

This instrument, which is derived from CAPS-IMS onboard CASSINI (Young

et al., 2004), consists of a 2D mass spectrometer of cylindrical symmetry with

respect to the main axis as illustrated in Figure 39. It operates over a large energy

range of ∼1 eV/q to ∼38 keV/q with an instantaneous FOV of $5° × 260°$. The

MSA entrance (blackened for UV rejection) features 32 angular sectors of $11.25°$,

9 of which are blinded by the Mio magnetometer mast. After MSA entrance, a

spherical analyzer enables measurement of the full range of ion energies in 1/32

of Mio spin. The grounded external electrode of this analyzer is designed in three

mechanical parts, including polarization of the central one leading to de-focusing

(thus, effective control) of the incoming ion flux. After the energy analysis, ions

are accelerated (±12 kV in maximum operation voltage) toward a time of flight

(TOF) chamber polarized with a linear electric field (LEF) along the instrument's

main axis. This leads to isochronous (independent of energy) TOF for reflected

ions up to ±12 keV for maximum operation voltage (Delcourt et al., 2016), hence,

enhanced mass resolution ($m/\Delta m > 40$) over a large range of masses up to 60

amu. The straight-through (ST) particles are collected at the bottom end of the

MSA TOF chamber, and a lower mass resolution is obtained that is somewhat

improved using the central detector with reduced path lengths rather than the

external one (Figure 39). Details of the TOF signal of MSA has been described by Saito et al. (2017).

Figure 40 shows the thermal shield of MSA. Some selected parts of the MSA electrostatic optics are shown in Figures 41 and 42. In particular, Figure 42 shows the 21 angular sectors of entry equipped with carbon foils at the TOF chamber entrance. This figure also shows the bi-metallized Hamamatsu MCP at the back of the energy analyser, which enables differentiation of the MCP gain on the outer edge, where START electrons are collected, from that in the inner part, where LEF counts are obtained.

The MSA high voltage power Supply (HVPS Figures 43 and 44) has 10 different sub-units supplying voltages of 30 V to +/- 12 kV. These voltages can be individually modified by commands during flight. A radiation hard Actel RTSX FPGA controls the output-voltage of each sub-unit, whereas monitoring and commanding of the voltages are performed by the MSA CPU. The sub-units comprise the power supplies for (i) the 2 MCP stacks of MSA, (ii) the adjustable MCP anode-voltages, (iii) the two flux spoilers, (iv) MSA reflectron with an operational voltage range up to +/-12 kV, and (v) a stepping voltage for the energy analyzer with a dynamic range between 0.1 V and 5.6 kV and a settling time <1 ms.

The CPU (Figures 45 and 46) performs instrument control and dedicated data processing. The advanced design is based on the AT697, a 48 MHz LEON2-FT fault tolerant SPARC processor architecture implemented in radiation hard ASIC, including Triple Modular Redundancy(TMR) and advanced Error Detection And Correction(EDAC) against SEU errors. Together with a radiation hardened, one-time programmable FPGA (Microsemi RTAX), the processor is employed for high-level instrument control and monitoring, control of sensor electronics and compres-

sion of scientific data. All internal interfaces and glue logic are embedded in the radiation hardened RTAX system FPGA to achieve the highest reliability. Program code images can be uploaded to the non-volatile memory and executed in the EDAC protected SDRAM module.

Figure 47 shows the top view (panel (a)) and bottom view (panel (b)) of the amplifier board and spacewire interface. Five charge signals from the MCP anodes are fed into five fast transistor amplifiers and the amplified signals are discriminated by constant fraction discriminators. A custom gate array with a titanium radiation shield calculates and buffers the signal timing with a time resolution of 781.25 ps. An FPGA Actel RTAX2000 that communicates with the CPU interfaces with MDP1, controls the custom gate array, and processes the signal timing calculated by the custom gate array.

The performance of the MSA instrument are given in Table 14. Its capability is summarized as follows. (1) ST data: high temporal resolution, high sensitivity measurements and medium mass resolution ($m/\Delta m$ up to $\sim$10) to focus on major ion species and allow rapid analysis of magnetospheric phenomena, which makes MSA appropriate for plasma analysis. (2) LEF data: high mass resolution measurements with $m/\Delta m$ up to 60 for ions with energies smaller than the MSA operation voltage, up to a maximum of 12 kV because ions with larger energies cannot be turned around by the LEF and are detected on the ST MCP. This process focuses on ions of planetary origin and enables precise composition measurement, which demonstrates the appropriateness of MSA for planetology studies.

910 *3.4.2 Operation Mode and Data Products of MSA*

911 MSA energy sampling features 32 energy steps over the full energy range (1 eV/q

912 to 38 keV/q) of the instrument during one spin sector: 1/32 spin = 125 ms. To

913 more effectively cover the wide energy range of MSA, two distinct sets of in-

914 terleaved energy steps are used during two consecutive spins. At the exit of the

915 energy analyzer, ions enter the TOF chamber, and secondary electrons collected as

916 START pulses are emitted upon crossing the carbon foils. Upon impact of the ions

917 on either the LEF or ST detectors, STOP pulses are recorded and the resulting

918 coincidences (i.e., the given STOP signal associated with the given START signal)

919 provide information on the particle TOF or, equivalently, on their mass to charge

920 (m/q) ratio.

921   Owing to the differences in ST and LEF spectra, two different approaches are

922 implemented. For LEF particles, TOF spectra with 2 x 32 energies (corresponding

923 to the two distinct sets of interleaved steps described above) are produced every 16

924 spins (64 s). For ST particles, once the STOP-START calculations are completed,

925 allocation of the ion mass is performed onboard using fixed mass groups. In total,

926 15 count rate matrices are built. The first four are "all ions" or "all START

927 counts", H^+, He^{2+}, and heavy ions including all ions with m/q ratios larger than

928 2. These matrices are produced at each 4 s interval and only these first four count

929 rate matrices are transmitted in the Mio low telemetry mode. The next 11 count

930 rate matrices relate to He^+, C^-, O^-, C, N, O, Na, Si, S, K, and Fe ions and

931 are produced at each 16 spins (64 s). Please note that negative ions here are not

932 external ions (the voltage configuration of MSA energy analyzer does not admit

933 negative ions) but ions produced via charge exchange during crossing of the carbon

934 foil (e.g., Funsten et al. (2001)). Using this mass identification, the moments are

935 subsequently calculated by MSA DPU (assuming Na mass for heavy ions because

936 this latter group of ions corresponds to all ions with m/q ratios larger than 2).

937 MSA internal products thus contain two types of count rate matrices : (i)

938 TOF matrices with no angular information for LEF data, and (ii) mass matrices

939 as described above for ST data. These internal matrices are then transformed to

940 external matrices for telemetry. In the latter matrices, energy sampling is reduced

941 to eight steps in the LEF data. For ST data, angular resolution is reduced to 36

942 view directions per spin. These external matrices are then transmitted according

943 to different modes selected on a scientific basis; normal mode (default mode) as

944 described in Table 15, high angular resolution mode (Table 16), and high time

945 resolution mode (Table 17). Other modes (not shown) include event mode and

946 burst mode (similar to Table 17 but with a higher production frequency).

947 The data downlink includes three distinct telemetry rates for Mio data: L-mode

948 (L) available most of the time, M-mode (M) during ∼25% of the time, and H-mode

949 (H) in some very limited portions of the Mio orbit. MSA is part of the MPPE

950 particle consortium; thus, the data modes are defined for specific MPPE science

951 research targets (e.g., survey mode, solar wind or exosphere dedicated modes,

952 reconnection mode) which is consistent with the modes adopted for the other

953 particle instruments. Table 18 shows the MSA data that will be transmitted in

954 the various Mio telemetry regimes depending upon the targeted research (Medium

955 A for survey, Medium C for solar wind or exosphere analysis). Since the MSA

956 possesses a CPU board that processes the mission data into the mission products

957 such as moment data, the MSA application in the MDP1 relays them to the data

958 recorder. The MSA application removes the dummy data and packs only effective

959 data into the mission packets.

3.4.3 Pre-Flight Calibration of MSA

961 Because the MSA instrument is a collaborative effort between four different teams,

962 both the Flight Model and the Spare Model were assembled at the PI institute

963 (ISAS, Sagamihara, Japan). Numerous test campaigns including pre-flight calibra-

964 tion were subsequently conducted at this institute. The present section provides a

965 summary of the calibration results.

966   Downstream of the MSA entrance, ions travel through the spherical energy

967 analyser, which has an external electrode at ground potential. On the inner elec-

968 trode of the analyzer, the voltage applied varies up to a maximum value of -5.6 kV,

969 which enables selection of ions with specific energy per charge (E/q) ratios. This

970 is illustrated in Figure 48, which shows the voltage applied to this inner electrode

971 for a 2 keV N^+ beam. In the figure, the voltage median value is approximately

972 -292 V, yielding an analyzer constant k of $\sim$6.85. With minimum and maximum

973 voltages of -0.2 V and -5.6 kV, respectively, MSA can thus operate from a few

974 electron volts per charge (eV/q) up to $\sim$38 keV/q. The figure also shows a mod-

975 ulation of the ion count rate within each of the 21 entrance windows owing to

976 the partition walls at each 11.25° step. Further analysis of the energy analyzer

977 response revealed energy resolution of $\sim$8.5%. Finally, the figure shows the MSA

978 response as a function of azimuth or, equivalently, the entrance windows. In the

979 other dimension (i.e., elevation or polar angle), the MSA FOV is centered at $\sim$5°

980 with an angular resolution (full width at half maximum, FWHM) of $\sim$5°. This

is illustrated in Figure 49, which shows particle counts versus voltage and polar

angle (elevation).

At exit of the energy analyzer, ions are accelerated toward the entrance of
the TOF chamber with nominal operation voltages of ± 11 kV corresponding to
85% of the MSA qualification voltages; the maximum operation voltages are ± 12
kV. Notably a grid, effectively acting as an electrostatic lens polarized at 1 kV
located near the exit of the energy analyzer prevents the large accelerating electric
field from penetrating deep into this analyzer and has a detrimental effect on ion
trajectories. Upon entry to the TOF chamber, ions interact with thin (~ 1 μg/cm^2)
carbon foils, which leads to emission of one or several secondary electrons in both
forward and backward directions. With the help of an electrode tailored for this
purpose, forward electrons are deflected toward the outer part of the LEF MCP
(Figure 39). At the back of this MCP, electrons are collected on a delay line and
the START pulse obtained is used to trigger TOF measurement. That is, the
START pulse opens a TOF window of ~ 1560 ns during which a STOP pulse
is expected; in practice, up to three STOP pulses can be recorded. Moreover,
the position of the electron impact on the delay line provides information on
the azimuthal sector of the incoming ion. This is illustrated in Figure 50, where
the color map shows data obtained between the 60 delay line sectors and the 21
entrance windows (or azimuth). Similar to that shown in Figure 48, the modulation
of the ion count rate is attributed to the regularly spaced partition walls at the
entrance of the instrument. Measurements of the START rate in the different delay
line sectors yield the 3D angular and energy distributions of the ions without mass
identification but with high temporal resolution.

To protect MCP from the potentially intense solar wind flux, a "spoiler" capability has been included in the design of the energy analyzer. As previously mentioned, the external electrode of this analyzer has been designed in three mechanical parts, with the capability to polarize the central one independently from the other two for de-focusing or spoiling the incoming ion beam. When the ion count rate over one spin exceeds 10^3 START events in one energy bin and one entrance window, the voltage on the central electrode is increased by one step at the end of the spin. Conversely, when the count rate drops below 5×10^2 START events, the spoiler voltage is decreased by one step. At the first switch-on of the spoiler, the voltage value used is that corresponding to 10% efficiency (56% of the inner electrode voltage) to effectively protect the MCP. Subsequently, the spoiler voltage is further increased (decreased) if the count rate is excessively high (low).

After crossing the carbon foils, the ions travel inside the TOF chamber and impact either the LEF MCP or ST MCP depending on their charge state; hence, a STOP pulse can be associated with the corresponding START to derive the particle TOF and its m/q ratio. As previously mentioned, LEF data are characterized by low count rates owing to the small fraction of ions that remain positively charged after crossing the carbon foils but a high mass resolution, which is of primary interest for planetology science. In contrast, ST data are characterized by high count rates (owing to the large fraction of ions neutralized during carbon foil crossing) but lower mass resolution, although this mass resolution can be improved to some degree by considering a small collection area at the center of the ST MCP. An example of the TOF data obtained is provided in Figure 51. The top panel in the figure shows LEF data for different ion species of N^+, O^+, Na^+ and K^+. Notably, the width of the measured spectra is narrow regardless of the ion mass.

The bottom panel of the figure shows ST data for conditions similar to those in the top panel. These ST spectra, which resemble those of MESSENGER FIPS, clearly contrast with those of LEF (top panel) with larger count rates and much lower mass resolution. In particular, the spectrum achieved for K^+ ions that spreads over a large TOF interval, owing to large angular diffusion and energy straggling upon crossing the carbon foils, cannot be clearly identified in the long TOF tail. As expected, the center panel of Figure 51 that shows the TOF spectra obtained on the central ST exhibits a somewhat enhanced mass resolution and lower count rates. Moreover, different ghost peaks appearing in the figure are attributed to secondary emissions inside the TOF chamber (Figure 10 of Delcourt et al. (2016)). Generally, these ghost peaks are less pronounced at larger operation voltages.

Tables 19 and 20 provide a more quantitative view of the results obtained from TOF chamber calibration. As an example, Table 19 shows the TOF parameters obtained for two different energies and two different operation voltages for He^+, Na^+ and K^+ ions. For a given operation voltage (± 8 kV or ± 11 kV), the isochronous nature of the LEF spectra is clearly apparent with similar T_m values regardless of the ion energy. In addition, the narrow width of the spectra led to enhanced mass resolution (computed as $T_m/\Delta T$) of at least 100.

In contrast to that in Table 19, the ST results in Table 20 clearly exhibit T_m values that decrease with increasing energy, regardless of ion species (He^+ or K^+) or operation voltage (± 8 or ± 11 kV). Moreover, the TOF spectra width increased significantly for K^+, exemplifying the poor mass resolution capability of ST for heavy ions.

A global view of the MSA TOF-mass mapping is provided in Figure 52, which shows the TOF intervals used to identify the ion species depending upon their energy.

3.4.4 Near-Earth Commissioning Results of MSA

In contrast to MPO, the Mio spacecraft will spin (4 s) during the orbit phase at Mercury. During the seven-year cruise, Mio is hidden behind the MOSIF thermal shield to avoid harsh solar radiation. As a result, MPPE particle instruments have narrow FOVs pointing along the Mio spin axis; thus, very limited data are expected throughout the cruise phase. In contrast to electrons that are nearly isotropic, the highly collimated solar wind ions cannot be recorded in the cruise phase configuration, because the solar wind direction is obstructed by MOSIF; only dark counts can be obtained. To simulate ions entering the energy analyzer, MSA features a calibration pulse that can be parameterized with different frequencies and delay line sectors. This START-like calibration pulse was used during near-Earth commissioning to check the MSA status and data flow.

Similar to that for other MPPE instruments, near-Earth commissioning of MSA has been organized in two sequences, with the first in November 2018 to check basic functionalities, and the second in June 2019 to check high voltages. Owing to the transmission of data via the MPO spacecraft during the cruise, only the L-mode telemetry regime is available. A problem was encountered during the first MSA commissioning sequence that appeared nominal until a calibration pulse triggered was not followed by L-mode data reception. Debriefing was performed and possible causes including hardware failure were explored according to fault tree analysis scheme. The second MSA commissioning sequence provided new information on

this problem because the L-mode data acquisition was successful in June 2019 but was contingent upon rebooting of MDP1, the MPPE dedicated DPU, before operating MSA. Although this rules out a hardware failure, the reason for this faulty behavior is not yet understood and still is under investigation.

Throughout the commissioning and operations, voltages are monitored through MSA dedicated CPUs via comparison of HK values with the command values. If both values are not consistent (with 15% margin) after one spin, an error message is produced in the corresponding Mission Data packet, if such an error message is obtained during four consecutive spins, an emergency MSA shutdown is issued. HV monitoring is initiated via upload of the On-board Command Language (OCL) procedure from EEPROM. When this HV monitoring is correctly enabled, the HK return value is "ON". Prior to HV setup, nine commands are sent to enable measurements and to set thresholds for START and STOP signals. The HV setup procedure is then conducted according to six different procedures corresponding to ± 8 kV, ± 10 kV and ± 11 kV in normal or safe modes with execution times varying among the procedures. As a general rule, safe mode is used during preliminary MSA operations. In chronological order, MSA HVs are set on LEF MCPs, ST MCPs, TOF chamber, and floating MCP. The TOF chamber and floating MCP voltages are then adjusted before triggering the energy analyzer sweep. During the second MSA commissioning sequence in June 2019, the following results were obtained.

− Nominal voltage (1500 V) on the LEF MCP stack

− Nominal voltage (2250 V) on the ST MCP stack

− Nominal voltage (450 V) on the floating MCP

– Half-initial operation voltage (±4 kV) in the TOF chamber

– Fixed voltage (500 V) in the energy analyzer

To finalize the MSA HV tests, delta commissioning was scheduled in August 2019, but was postponed until early 2020. Delta HV commissioning of MSA was performed at ESOC on February 4 and 5, 2020. All nominal voltages were successfully applied, including TOF chamber VHV (±8 kV), which will be used in the first phase of MSA operations. The energy analyzer sweep was also successfully triggered, making MSA ready for operations, although L-mode data transmission issue still is under investigation.

3.5 HEP-ele and HEP-ion

3.5.1 Instrument Description of HEP

The high-energy particle instruments for electrons and ions onboard Mio consist of two sensor heads, HEP-electron(HEP-ele) and HEP-ion. Figure 53 shows photographs of these instruments in a clean bench in the calibration facility at Nagoya University. Non-flight items(blue) protected the flight models during transportation before the final calibrations in April-May, 2014, as will be discussed in section 3.5.3. The specifications of HEP-ele and HEP-ion are summarized in Tables 21 and 22, respectively.

Both instruments are based on the new high-energy particle detection technology developed in Japanese research communities, for the X-ray astrophysics and space physics groups for space missions. The newest space exploration satellite in Japan, the ERG satellite, is also carrying a similar type of high-energy particle detection system using a single-sided strip silicon solid-state detector(SSSD)

1124 and an ASIC (VA32TA, IDEAS, Norway: Mitani et al. (2018)) as well as the

1125 Japanese X-ray Astrophysics mission, Astro-H(Hitomi) (Watanabe et al., 2014).

1126 In the HEP instruments onboard Mio, the strip system is not used for position de-

1127 tection, rather, it is used for noise reduction of SSDs owing to the small capacitance

1128 and dark current in each strip. In the case of the flight-model HEP-ele onboard

1129 Mio, similar to HEP onboard ERG, the SSSD-ASIC system is applied to obtain

1130 angular directions of incident electrons used together with a pinslit type aper-

1131 ture. The SSSD-ASIC system reduces the noise level(dark currents) by separating

1132 into 158 strip-shaped areas with small capacitance connected and controlled by 5

1133 ASICs. Figure 54 depicts two sections of HEP-ele, in which two separate assem-

1134 blies of this combination of an SSSD and five ASICs cover up- and down-looking

1135 FOVs from the spacecraft spin plane, respectively. Each SSSD-ASIC assembly has

1136 a rectangular SSSD forming a one-layered stack with 158 strips and 5 ASICs to

1137 cover $18° \times 57°$ in total, and an angular resolution of $18° \times 11°$ is achieved by

1138 binning these 158 strips into 5 directions according to their ASIC connections.

1139 The accumulated pulse height levels corresponding to the deposited energies in

1140 the neighboring three strips are used to calculate the incident particle energy.

1141 These slow-shaped pulse height signals from the 10 total ASICs are processed in

1142 an analogue-digital converter(ADC) board and an FPGA in the HEP-ele sensor

1143 head electronics. Another FPGA is designated for the space-wire interface to the

1144 mission data processor (MDP). The analogue-digital conversion of the pulse height

1145 for the neighboring three strips is conducted sequentially by the ADC, and their

1146 accumulation for the total energy analysis is performed in the FPGA. The in-

1147 cidence direction for each particle detection is also identified and tagged in the

1148 FPGA using the ASIC fast-shaped signals. Figure 55 shows the SSSD-ASIC as-

semblies for HEP-ele in which 158 strips on the SSSDs and 5 ASICs are connected by wire bonding. To avoid contamination by heavier space particles with energies less than several hundreds of kilo electronvolts for protons and stray solar photons, the incident areas of SSSD are coated by Al with an appropriate thickness of 100 μm. The inner walls of the detector section are blackened with conductive paint for decreasing the reflected stray photons(Figure 56). This black carbon painting was developed by Nishiura Paint Industry in Japan (https://www.nishiura-p.com) and was also applied to the plasma particle instruments in the previous Japanese space exploration missions, e.g., PSA-ESA on Nozomi(Planet-B) (Machida et al., 1998) and MAP-PACE on Kaguya(SELENE) (Saito et al., 2010b). The entire sensor head of HEP-ele contains high-voltage supply and front-end processing boards behind the detector section that consists of the pinslit aperture and two SSSD-ASIC assemblies. These components and data/signals are controlled/processed by two FPGAs, as schematically illustrated in the block diagram in Figure 57. The on-board calibration signals and the bias voltages for the pulse discrimination in each ASIC are also issued via DACs from the FPGA. For preventing the intense solar irradiation near the Mercury orbit from entering the detector section through the pinslit aperture, a rectangular thermal shield is equipped in the Mio spin plane in the overall FOV of HEP-ele at the outside of the aperture(Figure 58). Therefore, the angular area of $\pm 4°$ from the spin plane is blocked from the effective HEP-ele FOV by two SSSD-ASIC assemblies as a dead angle range.

The HEP-ion sensor has two measurement capabilities for energy and TOF analyses for the incident ions. These measurement principles, as schematically given in Figure 59, are essentially the same as those introduced by Saito et al. (2010a). Some structures and performances have been simplified and omitted ac-

cording to the weight reduction requirement from the viewpoint of the overall

spacecraft mission management. The energy/TOF measurement section of the

flight-model HEP-ion has five types of components: a conic-shaped collimator, an

ultra-thin carbon foil with $0.5~\mu g/cm^2$ put on electroformed mesh folder with trans-

mission of 66%, two assemblies consisting of three SSSD-ASIC pairs and electron

leading meshes, an electrostatic mirror as one of outer structures of the sensor, an

MCP assembly with an electron attracting mesh, a TOF start-signal anode and

six TOF stop-signal anodes. The optimal voltages in the TOF analysis unit are

also shown in Figure 59 by red. The SSSD incident surface of the engineering-type

model is presented in Figure 60, in which the electron leading meshes are not set

up. As illustrated in Figure 61, the number of the HEP-ion FOV directions is six,

each of which corresponds to one of six SSSD-ASIC pairs for the energy analysis

measurement mode or TOF stop-signal anodes of the MCP assembly for the TOF

analysis measurement mode. Similar to the data processing in the HEP-ele sensor

head, the energy/TOF analysis results are sorted into eight steps. Different from

the collimator of HEP-ele, the collimator system of HEP-ion is more complicated

because the total FOV configuration of HEP-ion is nearly half of a conical shape

rather than a planar type. The closure of the inner conical part of the collima-

tor is designed to protect the ultra-thin carbon foil with a 2-cm diameter from

the acoustic vibrations/shocks during the spacecraft launch operation. A biphenyl

block sublimable in vacuum is loaded in the cylinder to keep the inner conical

collimator closed before the launch operation. Several days after the spacecraft

launch, the biphenyl block is sublimated in space to release the inner conical col-

limator to the measurement position by the extension of a mechanical spring(not

shown in Figure 61). The collimator and the measurement section of HEP-ion are

also blackened with the same black paint as that used for HEP-ele(Figure 62). Because the aperture size of the conical collimator of HEP-ion is much larger than that of HEP-ele, as shown in Figures 54 and 61, the large thermal shield for HEP-ion is installed on Mio(Figure 63). The dead angle range is $\pm 12.5°$ with respect to the spin plane because a side stay blocks the center of the effective HEP-ion FOV between two SSSD-ASIC assemblies. Figure 64 illustrates a block diagram of HEP-ion, in which the TOF analysis circuit is added to the HEP-ele diagram. It should also be noted that the numbers of the high-voltage supply units(three for HEP-i, one for HEP-e) and the ASICs(six for HEP-i, ten for HEP-e) are different from those of HEP-ele.

3.5.2 Operation Modes and Data Products of HEP-ele and HEP-ion

Because of the severe restriction of the telemetry data allocation to HEP-ele and HEP-ion observations, the energy/TOF analysis data need to be compressed by using accumulation over several FOV directions and observational intervals. The measurements themselves are quite simple compared with those of other instruments of MPPE such as MPPE-MSA. As described in section 3.5.1, HEP-ele originally had 10 FOV directions in the spinning spacecraft frame, corresponding to the polar angles in the direction perpendicular to the spin plane, and eight energy steps. However, the spin motion is divided into 16 sectors, which indicates that the raw count data in 10(polar angle) $\times$ 8(energy) $\times$ 16(sector) bins are produced with every spin motion. Whereas HEP-ion has a similar raw count data structure, the number of FOVs is six. The measurement modes of HEP-ion could be switched between the energy and TOF analyses by changing the high voltages applied in the measurement section. These count data could be compressed in MDP1 ac-

cording to three spacecraft operation modes, e.g., L- and M-modes. The H-mode of HEP-i is not allocated in the current observational plan for reducing the total HEP data because the HEP-e observations and their data with the high data rates are considered to be more important. Tables 23 and 24 show the data modes for HEP-ele and HEP-ion, respectively, in which the values in round brackets indicate the angle resolutions for the polar(FOV) and sector directions. The energy channels for HEP-ele and HEP-ion and the TOF channels of HEP-ion depend on the energy/TOF binning tables selectable by operation commands.

3.5.3 Pre-Flight Calibration of HEP

The standalone SSSD-ASIC systems of HEP-ele and HEP-ion were calibrated with a radioactive source(^{137}Cs) emitting high-energy electrons with energies of more than 600 keV to check the basic performance including the readout capabilities of the ASIC. Figure 65 presents the pulse-height analysis results obtained with 2 of the 158 strips in the SSSD-ASIC assembly for HEP-ele. Two separate peaks are clear near the uppermost channels corresponding to electric charges produced in the depletion layer of the SSSD by the incident electrons with 624 keV and 656 keV, respectively. Broad distributions spreading over lower channels are caused by contaminations by a continuum component composed of high-energy photons(X-rays and gamma rays) and scattered electrons in a wide range of energy originating from the radioactive source used for the calibration. This type of readout signal from SSSD by ASIC could be analyzed according to the pulse heights for all 158 $\times$ 2 = 316 strips in the 2 SSSD-ASIC assemblies and determines the total energy and incident direction for each of the incident electrons.

The electron/ion beamlines in the calibration facility at Nagoya University(Figure 66) were also used to check the performance in the lower-energy ranges of the HEP-ele and HEP-ion measurements. The energy ranges used for the HEP instruments were 40-100 keV for electrons and 60-140 keV for protons, and ions of He and N. To check the instrumental response according to the incident angles, we rotated the HEP-ele or HEP-ion instrument around three independent axes in the vacuum chamber during the beamline calibrations. Using a multi-axial turntable system, the FOV direction was set parallel to or oblique by aimed angle with respect to the charged particle beam with diameters of a few tens of millimeters at a given energy. Figure 67 shows the HEP-ion instrument with the harness set on the turntable system in the vacuum chamber.

The histograms showing the pulse height distributions produced by irradiating electrons with the energy of 100 keV are given in Figure 68, in which six plots are correspondent to incident (polar) angles identified by the strip and ASIC numbers of HEP-ele. In each plot, two distinct peaks present a so-called pedestal(background noise level) owing to the SSSD-ASIC characteristics and an actual signal distribution for the 100-keV electron energy deposits in the depletion layer of the SSSD(e.g., Mitani et al. (2018); Kasahara et al. (2009)). The channel numbers of the peak distributions in the abscissa are not always identical for all six plots because the dark current levels measured in the 10 ASICs could be different. These level differences among the 10 ASICs are subtracted after the pulse height analyses in the HEP-ele FPGA procedures to achieve sufficient energy discrimination capability over the entire energy range of HEP-ele. Similar calibrations have been performed for two SSSD-ASIC assemblies in HEP-ion by emitting typical types of ion species with several levels of energies. Figure 69 shows examples of

the pulse height analyses for 140-keV protons, in which six panels correspond to six FOV directions, each of which is detected by the corresponding ASIC. The lower portions of the energy distributions for the 140-keV proton beams overlap with the pedestal distributions at lower channels than the proton distributions, which is different from the distributions in Figure 68. This occurred because the energies of ions injected into the solid state detectors with a certain thickness of the dead layer can be reduced more significantly than those of electron cases. Similar to the HEP-ele energy distributions in Figure 68, the energy and pedestal peaks are not identical for six ASICS of HEP-ion regarding the energy channels in the abscissas. These channel discrepancies among the ASICs can be reduced by the onboard routine process for channel difference subtraction in the FPGA of HEP-ion, which is also similar to the HEP-ele procedures.

The HEP-ion instrument has the capability to measure the velocities of the injected particles by using the TOF unit, as described in the previous subsection. We also checked the TOF performance with the ion beamlines at Nagoya University and JAXA. Figure 70 summarizes the TOF experimental results for four different energies(60, 120, 250, 1000 keV) and three ion species(proton, singly-charged He and N). Because the heavy ion beams were not applicable beyond 150 keV owing to the JAXA high-energy beamline facility performance, the TOF distributions were measured only for H^+. The incident FOV directions were changed in these measurements so that the maximum peaks were obtained in the different ASIC assemblies as indicated by different colors in the histograms.

1293 *3.5.4 Near-Earth Commissioning Results of HEP*

1294 The first in-flight operations for HEP-ele and HEP-ion were conducted during the

1295 near-Earth commissioning phase of the BepiColombo mission. High-voltage up to

1296 98.2 V was supplied to two SSSD assemblies of HEP-ele. We confirmed the normal

1297 HK status including the instrument currents and significantly low dark counts.

1298 The six HEP-ion SSSDs were also checked to be activated by the operation with

1299 the high-voltage up to 99.7 V, in which the instrument currents and HK status

1300 were confirmed to be normal. The activation of the TOF unit of HEP-ion was

1301 performed safely to obtain the normal HK status with the high-voltages supplied

1302 up to 990 V and 2271 V to the mesh system deriving the start/stop electrons

1303 and the MCP assemblies, respectively. The dark counts were measured steadily as

1304 constant MCP noise.

1305 3.6 ENA

1306 *3.6.1 Instrument Description of ENA*

1307 The ENA instrument is based on the surface conversion/reflection technique and

1308 consists of four subsystems, including an ion rejection system, ionization surface,

1309 photon rejection system that also performs crude energy analysis, and velocity

1310 analysis section (Kazama et al., 2009). Figures 71, 72, 73, and 74 show the concept,

1311 schematic view, flight model of the instrument, and sun shield mounted on the

1312 spacecraft, respectively.

1313 Neutrals enter the sensor through an electrostatic charged particle deflector,

1314 which rejects ambient charged particles by a static electric field. The incoming

neutrals are then converted to positive ions on an ionization surface and then pass through an electrostatic analyzer of a specific (wave) shape that effectively blocks photons. The electrostatic analyzer also provides crude energy analysis. The "wave" electrostatic analysis design is similar to that used in the MTOF sensor of the CELIAS instrument on the SOHO spacecraft (Hovestadt et al., 1995), which provides a photon rejection factor of 2×10^{-8}. Because the instrument must be capable of measuring masses up to Fe, no foils can be used in the following TOF section. To measure the particle velocity (mass), we useed the particle reflection principle developed for and utilized in the Neutral Particle Detector (NPD) of the ASPERA-3 and - 4 experiments (Barabash et al., 2006, 2007) for ESA's Mars and Venus express missions. After exiting the electrostatic analyzer, ions originally neutrals that were converted to ions by the ionization surface are post accelerated up to an energy of 1.5 keV and impact the START surface under a grazing angle of $15°$. During the impact, kinetic secondary electrons are emitted and the particles are reflected toward the STOP MCPs, where they are detected and produce a STOP pulse. The secondary electrons from the START surfaces are guided to the START MCPs and produce a START pulse. The START and STOP timing gives the particle velocity. Combining the TOF measurements and electrostatic analyzer settings one determines the LENA energy and mass. Measuring the radius and azimuth of the neutral hit on the START surface by position sensitive START MCPs enables accurate determination of the TOF length and the arrival azimuth of the incoming neutrals. Figure 75 shows the ENA block-diagram. The instrument electronics include two boards, interface electronics (IFE) and HVPS. The DC/DC converters and digital processing are provided externally. The ENA sensor characteristics are summarized in Table 25.

The ENA sensor comprises six key elements: (1) conversion surface, (2) photon absorbing surfaces, (3) START and STOP MCP assemblies, (4) START surface, (5) IFE, which provides front-end-electronics functions, sensor control, and interface with the MPPE DPU (MDP1), and (6) HVPS.

(1) Conversion surface

After passing the electrostatic analyzer, LENAs hit a conversion surface under a grazing angle of $15°$, where they are converted to positive ions. The surface is Al_2O_3 (alumina) deposited on a polished (highly smooth) substrate, such as a silicon wafer. A photograph of the conversion surface is shown in Figure 76. The temperature of the conversion surface is controlled to stay above $+50°C$ throughout the mission to avoid a stack of contaminating materials that would decrease the efficiency of neutral to ion conversion. The conversion surface element has two heater systems. One is operated by the heater control system onboard MMO. The other is powered by MPO and is controlled by the ENA heater control and temperature monitoring system (ENA HCS) installed in the ENA instrument. This is necessary because MMO is turned off most of the time during the cruising phase to Mercury. The power for ENA HCS is separated from the other ENA electronics.

(2) Photon absorbing surfaces

The large electrodes in the wave electrostatic analyzer are specially designed coated plates with high photon absorbing surfaces. The grooves on the plates follow the design for the PLASTIC instrument on SOHO (Galvin et al., 2008). The coating is CuS. This structure serves as a very efficient trap for photons. The total UV transmittance of the system before the TOF section is $< 10^{-9}$.

(3) START and STOP MCP assemblies

The START MCPs are used for both START timing and the determination of the START hit position (radius and azimuth). A chevron of annular MCP plates with an outer diameter 100 mm is used. The electron cloud exiting the back of the MCP is split between a grid and a plate discrete anode. The grid is divided into seven decoupled sectors to give seven azimuths and seven START timings. The plate anode is divided into four concentric rings to provide determination of the TOF length, where the TOF path length range is from 34 mm to 60 mm. For each individual case, uncertainty of about ± 5 mm is present owing to the different orientations of the START surface and the STOP MCP front planes. The STOP MCPs are used for STOP timing and determination of the STOP hit position (only azimuth), with four identical assemblies used. The anode behind each MCP assembly is divided into two parts, giving eight independent outputs. Figure 77 shows the channel definition of the MCP anodes.

(4) START surface

The START surface provides effective reflection of the particles (high reflection coefficient, narrow scattering angle) and high secondary electron yield. The secondary electron yield can be optimized by increasing the post acceleration voltage, and the reflection coefficient can be increased by choosing materials for the START surface with high atomic numbers. The START surface is mono-crystalline tungsten. Figure 78 shows a photograph of the START surface installed in the electrode structure of the TOF section.

(5) Interface electronics

The IFE has the following functions:

− Amplification of MCP output signals

1388 – Measurement of the time between START and STOP signals

1389 – Generation of calibration pulse

1390 – HVPS control and monitoring its output levels

1391 – Communication with MDP1 (reception of commands and transmission of mea-
1392   sured data)

1393   IFE has 19 charge sensitive preamplifiers – shapers including seven fast pream-
1394 plifiers for seven START sectors, eight fast preamplifiers for eight STOP plates and
1395 four slow preamplifiers for four START rings. One TOF unit accepts START sig-
1396 nals from any of the seven START sectors and STOP signals from any of the eight
1397 STOP plates. IFE also contains the necessary ADC and DAC (analog-to-digital
1398 and digital-to-analog converters) needed for HVPS control.

1399 **(6) HVPS**

1400   One double (positive/negative) supply provides the high voltages applied to
1401 the sensor electrodes and bias voltages for MCPs, which is then regulated by
1402 optocouplers to the nominal values. Figure 79 shows a photograph of the assembled
1403 configuration of HVPS, the STOP MCP assembly, and the preamplifier/digital
1404 processing electronics boards.

1405 *3.6.2 Operation Mode and Data Products of ENA*

1406   **Operation mode of the ENA sensor**

1407 The ENA sensor has mostly full solid angle coverage (12.0 sr FOV) for ENA
1408 detection by using spacecraft spin motion. To obtain angular resolution for the
1409 spinning direction, the spin period (Ts: nominally 4 s) is divided into 16 spin
1410 sectors, where the energy scan of 8 steps is performed for each spin sector. ENA

sends a data packet with fixed size (3,072 byte = 384 byte × 8 energy steps) to MDP1 every spin sector.

The ENA sensor has four operation modes: (1) coincidence mode, (2) counter mode, (3) engineering mode, and (4) table read mode. The coincidence mode provides the count and TOF values shown in Table 26. When the ENA sensor detects ENA signals, it gets four types of information such as ID of sectors (START SECTOR, START RING, and STOP SECTOR), which detect the signals, and TOF value for the time interval between the signal detection at START and STOP sectors. The ENA sensor generates raw data that contain this information in 20 bits (TOF event data, Table 27) for each event of particle detection. However, if the occurrence rate of the particle detection events is too high, the sensor cannot send all of them to MDP1, where the reported data are the first 136 events per energy step. Therefore, the data packet of the coincidence mode contains counter values in which all of the corresponding events are counted. The counter mode provides the detailed counter data shown in Table 28, although the maximum number of TOF event data sent to MDP1 is limited to 100 for each energy step.

When the ENA sensor is in the engineering mode, housekeeping (HK) and status data are sent to MDP1. On the other hand, the reference table of sweeping high voltages (SVs) for the energy scan is sent via the table read mode.

Data processing in MDP1

The MDP1 receives 24576 bit = 3072 byte/read cycles, which includes scientific data but excludes HK data. The contents of the scientific data change according to the sensor mode. After receiving the data, MDP1 decodes and reformats both types of data. The format of the data is dependent on the telemetry mode. All

telemetry data transferred to the S/C must have timing information added. The time-tagging provides the acquisition time of the data.

The instrument has four telemetry modes that define the data format and data processing before transmission to ground. The MDP1 processes the data collected from the sensor and generates data sets compatible with one of the four telemetry modes. The data sets are either down-linked to ground or are stored in temporary memory on the S/C side. The telemetry modes are given below.

a) Mass accumulation mode

b) TOF accumulation mode

c) Count accumulation mode

d) Non process mode (The sensor data are downlinked with no processing in MDP1)

e) Idle mode (No telemetry data are generated)

There are limitations for possible combinations of the telemetry mode and the sensor mode. Table 29 summarizes the allowable combinations.

In the Mass, TOF, and Count accumulation modes, the memory in the MDP1 is allocated for count data accumulation. Data originating from the sensor is sorted by look-up tables and is categorized into two types of accumulation matrices during a time period specified by commands. One is the accumulation matrix as described below.

Contents:

Event data integrated during a sampling period

Dimensions:

Four dimensions (E, P, C, M) for the mass accumulation mode,

1459   Two dimensions (E, TOF) for the TOF accumulation mode,

1460   Three dimensions (E, P, X) for the count accumulation mode,

1461   where E is the energy group, C is the channel group, P is the phase group, M is the

1462   mass group, TOF is time of flight, and X is the type of counters, namely START

1463   ring, START sector, STOP plate, STOP coincidence, or START coincidence count.

1464   The other matrix is the accumulation scaling matrix, as described below.

1465   Contents:

1466   Counter data summed during a sampling period

1467   Dimensions:

1468   Three dimensions (E, P, Y) for the mass accumulation mode,

1469   Two dimensions (E, Y) for TOF accumulation mode,

1470   Not needed for the count accumulation mode,

1471   where Y is the type of counters, namely total START count, total STOP count,

1472   coincidence STOP count, coincidence START and STOP counters (seven + eight).

1473   The numbers of bins in each element can be set by commands. Possible numbers

1474   of bins are given below.

1475   n(C)   1 or 7;

1476   n(E)   1, 2, 4, or 8;

1477   n(P) 1, 2, 4, 8, 16, or 32;

1478   n(M) 1, 2, 4, 8, 16, 32, 64 or 128;

1479   n(TOF) 1024;

1480   where n(XX) means the number of bins for XX. The numbers of bins in E and P

1481   are coupled and are not independent:

1482   If n(E) = 1, 2 or 4   then n(P) = 1, 2, 4, 8, 16, or 32

1483   If n(E) = 8   then n(P) = 1, 2, 4, 8 or 16

1484 The total number of elements in the accumulation matrix should not exceed 8192

1485 owing to memory space limitations. Any mode requiring a larger accumulation

1486 matrix is invalid.

Mass accumulation mode

1488   This mode is used to obtain ENA data with mass information and will com-

1489 monly be used in the orbit. This telemetry mode requires the coincidence mode

1490 as the sensor mode. Coincidence data from the sensor are sorted and accumu-

1491 lated into a matrix. The accumulation matrix has four dimensions: E (energy), C

1492 (channel), P (phase), and M (mass). An accumulation is made during a specified

1493 time interval, which is defined by a command. To compensate for high count rates,

1494 where not enough space is available to transmit all coincidence events, the total

1495 number of START, STOP, and coincidence STOP counts is added up for each

1496 combination of n(P) and n(E) in the accumulation scaling matrix. This matrix

1497 enables scaling of the accumulation matrix during the data analysis on ground.

1498 When the mass accumulation mode is set, the coincidence mode is always needed

1499 as the sensor mode. In this case MDP1 receives event entries of coincidence counts

1500 in each energy step. It then obtains its mass group (M), incoming direction (C),

1501 and energy (E) for every coincidence event and accumulates them into the accumu-

1502 lation matrix. This accumulation is made over a certain time set by a command.

1503 Finally, MDP1 sends to S/C the contents of the accumulation matrix and other

1504 information after the accumulation.

1505   A schematic data calculation flow diagram of the mass accumulation mode is

1506 shown in Figure 80. A mass group M is calculated from the START ring, START

sector, STOP plate and TOF by using look-up tables. The energy group E as well as the phase group P are calculated from the slot number of each sensor data packet. The channel group C corresponds directly to START sector. For every event obtained, the MDP1 increments the counters specified by E, P, C and M in the accumulation matrix. The numbers of bins for each parameter can be set by commands. The total counter data included in sensor data are accumulated in the accumulation scaling matrix. This matrix only has two dimensions; energy group E and phase group P.

MDP1 Data processing method on the mass accumulation mode

Data processing on MDP1 for each event consists of five steps, as given below.

Step 1 Obtain index of energy depending on sweep pattern

This index will later be used to obtain the actual value of the energy from the SVE table

Energy-index:

E-index = SVM-Table[SV-index, Energy-step],

where SV-index is selected from table ID for the SV reference table during the observation.

Step 2 Obtain derived data for mass calculation by look-up tables

a) Square root of energy: En = SVE-Table[E-index] (10 bit values)

b) Inv. of path length: L_{inv} = LT[sector, ring, plate, E-index] (12 bit values)

c) Flight time: t_1 = TT[tof] (10 bit values)

The SVE-table returns the actual particle energy corresponding to an Energy-index. Consequently, the values returned from the SVM- and SVE- tables must

reflect the particle energy selected in the SV table. If L_{inv} is zero, it is regarded as

an invalid event by the onboard software. When an anomaly is found on a specific

START SECTOR – START RING – STOP SECTOR pair at a specific energy, it

can be rejected from the onboard calculation by setting $L_{inv} = 0$ on the LT-table.

Therefore, the LT-table is designed as energy dependent. The LT-table can also

compensate for a possible energy dependent energy loss on the START surface.

In this case, the tof-path-length used in the mass calculation would be artificially

extended for energies that have a higher relative energy loss. This was not used,

however, based on the calibration results. Therefore all the path lengths used from

the LT-table were the same for all energies. The TT-table returns the tof value

only when tof $\leq$ 0x3ef. If tof $\geq$ 0x3f0, it returns 0 which is regarded as invalid

event in the onboard calculation (Table 27).

Step 3 Calculate mass

Mass calculation is accomplished using 32 bit unsigned integer operations. The

values of the tables in step 2 guarantee that no overflow occurs.

$$\text{mass\_0\_5} = \big(\{(\text{En} \times t_1 \times L_{inv})/65536\} \times \text{Factor}\big)/65536 \tag{1}$$

where Factor = 3340. If the calculated value for mass_0_5 is larger than 255, a

value of 255 must be assigned to mass_0_5 prior to further processing. The value

calculated here is actually proportional to the square root of the mass.

Step 4 Bin the data according to the binning parameters set

$$\text{a) mass group M} = \text{MT[mass\_0\_5]}/\{128/n(M)\} \tag{2}$$

$$\text{b) channel group C} = \text{sector}/\{7/n(C)\} \tag{3}$$

$$\text{c) energy group E} = \text{Energy\_step modulo } n(E) \tag{4}$$

$$\text{d) phase group P} = (\text{phase - phasemin})/\{32/n(P)\} \tag{5}$$

Where phasemin contains the first spin phase value to be considered, whereas phasemax is the last phase value to be considered. To use all phase values, phasemin = 0, phasemax = 31. All divisions in equations (2) ? (5) are integer divisions.

Step 5 Update the accumulation and the accumulation scaling matrix

Accumulation matrix (M, C, E, P) = Accumulation matrix (M, C, E, P) + 1

Accumulation scaling matrix (E, P, Y) = Accumulation matrix (E, P, Y) + 1

This calculation is required for all events in a packet.

Count accumulation mode

This mode is used to obtain the detailed signal count at each MCP plate and is similar to the mass accumulation mode, except that counter data are summed. When count accumulation mode is set, the sensor always needs to be set to the counter mode. In this mode, instead of receiving coincidence events, MDP1 receives detailed total counts on each MCP anode during one energy step. Then the total count data are summed as the accumulation matrix. This accumulation is made over a particular time set by a command, and the contents of the accumulation matrix are sent to S/C.

TOF accumulation mode

This mode is used to obtain raw TOF distributions without mass information. The primary uses of the raw TOF data are to analyze the performance of the instrument and to calibrate the on-board mass calculations. This mode is similar to the mass accumulation mode, except that TOF data are accumulated instead of mass data. In TOF accumulation mode, the mass is not calculated, and the raw TOF data are directly used for the accumulation instead of the mass. The accumulation matrix in this mode has two dimensions: E (energy) and T (TOF). MDP1 does not use the other parameters of P (phase) and C (channel). Because TOF data have 10 bits, the number of TOF bins is always 1024.

3.6.3 Pre-Flight Calibration of ENA

The instrument was calibrated at the Messkammer für Flugzeitinstrumente und Time-of-flight (MEFISTO) calibration facility (Marti et al., 2001) at the University of Bern. The facility produces an energetic neutral atom beam by neutralizing a collimated ion beam on a conversion surface (Wieser and Wurz, 2005). The beam neutralizer is an integral part of the MEFISTO facility and produces a neutral beam of known composition, well-characterized in angle and energy. For the instrument calibration, neutral H, neutral He and neutral O beams were produced in an energy range from 30 – 3000 eV per particle. During the calibration the instrument was mounted on the MEFISTO hexapod turntable, which enabled rotation and translation of instrument relative to the fixed energetic neutral atom beam. An additional thermal heating/cooling plate enabled performance investigation at different temperatures (Figure 81).

The calibration was split into four phases between 2012 and 2014 with interspersed calibration data analysis phases. This approach enabled to repeat measure-

ments that had insufficient statistics and other quality problems detected during the data analysis. The calibration tasks were separated into establishing energy response, angular response and mass response.

Energy response

The energy response of ENA is determined by the electrostatic wave energy analysis system and the energy loss function on the conversion surface. The latter strongly depends on species and energy, which makes the energy response species and energy dependent. To simplify operations, only 16 different energy settings were characterized, with each identified by an index and nominal center energy for bookkeeping purposes. The actual peak energy of each energy bin is species dependent (Table 30). The actual energy sweep in the instrument consisted of eight energy settings selected from this table. The width of the energy pass band ΔE for hydrogen is energy independent with $\Delta E/E = 100\%$, with E as the nominal center energy. The energy pass bands for oxygen have a tail toward higher energies owing to the more prominent energy loss at the conversion surface. The quantitative extent of this effect needs further analysis.

Angular response

The angular response was determined by rotating the instrument relative to an incident neutral hydrogen beam in a grid like pattern. The count rates obtained from each START sector were then fitted with 2D angular Gaussian profiles. Table 31 shows the bore sight directions and widths of each of the seven viewing directions corresponding to the seven START sectors. θ_0 denotes the center in azimuth, β_0 is the center in the elevation direction, and $\Delta\theta$ and $\Delta\beta$ are the FWHM values of the fitted peak widths. The coordinate system used is shown in Figure 72.

The azimuthal resolution $\Delta\theta$ varies linearly between $32.5°$ at sector 0 and $22.9°$ at sector 6, and the elevation resolution $\Delta\beta$ decreases linearly between $11.6°$ at sector 0 and $7.1°$ at sector 6. We believe this trend to be a result of a mechanical misalignment between the wave system and the TOF cell. The angular response is in first order not energy dependent.

Mass response

The TOF values measured onboard are converted to a nearly energy independent mass number M in the range from $0 - 255$. Before reporting to telemetry, M is converted to a mass group number compatible with the selected binning parameters by using a mass lookup table and possible further division by using a constant, as shown in Figure 80. For calibration data analysis the mass number M was used to establish the shapes of the different mass peaks in the mass spectrum. The shape of the hydrogen mass peak is shown in Figure 82(a). Owing to its larger mass, oxygen might generate hydrogen recoils at the conversion surface, which can result in an additional hydrogen peak even when the conversion surface is hit by oxygen only (Figure 82(b)). The intensity of the additional hydrogen signal depends mainly on the amount of water absorbed on the conversion surface. The mass spectrum to neutral helium is more complicated because both recoil hydrogen and recoil oxygen atoms appear. For the case of incident neutral oxygen, a mass comprehensive cross-talk matrix could be generated, which enables separation of the individual recoil contributions. The matrix for incident neutral helium is sparser owing to limited calibration time available for helium.

Geometric factor

In its simplest form the geometric factor G is expressed as

$$G = \Delta E/E \times \Delta\Omega \times \Delta A \times \epsilon \qquad (6)$$

where $\Delta E/E$ is the energy resolution, ΔA is the effective aperture area, $\Delta\Omega = \Delta\theta \times \Delta\beta$ is the angular acceptance, and ϵ is the detection probability. The first two factors energy response and angular response are well established. The detection probability for both START and STOP detectors is obtained from the START and STOP rates in the TOF cell (Funsten et al., 2005). Typical observed values for hydrogen are 1% at 100 eV increasing to 30% at 1000 eV. The best estimates for the geometric factor for neutral hydrogen are listed in Table 32:

3.6.4 Near-Earth Commissioning Results of ENA

The temperature of the conversion surface is controlled to remain above $+50^\circ$C throughout the mission to avoid a stack of contaminating materials which would decrease the efficiency of neutral to ion conversion. So far, the temperature has been successfully maintained above $+50^\circ$C, except for some cases of short duration that did not affect the conversion performance because the temperature was still greater than that of the surrounding structures. The power for the ENA heater control and temperature monitoring system (ENA HCS) is separated from the other ENA electronics.

Except for a high-voltage unit, ENA was activated on November 25, 2018 for the first time after the launch. No problems were found during the test. The ENA function tests with the HVPS were conducted on June 27 and 28, 2019; August 20 and 22, 2019; and February 6 and 7, 2020. These tests were conducted when the spacecraft was in the solar wind. During the testing, all of the high-voltage outputs

were gradually increased up to their nominal settings for the actual observation. For the input surface of START and STOP MCPs, -2300 V and -2600 V were applied, respectively, where dark counts were successfully detected by all input channels of the pre-amplifiers. For the other electrodes, voltage sweeping for energy analysis was also tested with no problems detected. However, no valid ENA counts were identified during the testing, because the FOV of ENA is mostly blocked by MOSIF during the cruising phase. Although part of the FOV of ENA is not blocked by MOSIF, the unblocked direction is not pointed toward the Sun. In this case, faint ENA flux is expected in the solar wind.

ENA will be activated during the Earth and Venus fly-bys before the Merculy orbit insertion to measure ENAs generated by charge-exchange interactions between hot ions and cold atmospheric neutrals.

4 Data Products of MPPE

To conduct coordinated observation between the MPPE sensors and to control the total telemetry data rate, the MPPE data mode is defined. The operation mode of LEP and HEP sensors are determined so that they generate the data products depending on the MPPE data mode. Because ENA generates only L-mode data with fixed data rates, it is operated independently of the MPPE data mode. Six MPPE data modes are defined: default observation mode, exospheric mode, solar wind mode/IP shock local mode, IP shock macro mode/bow shock mode, reconnection mode, and magnetospheric mode. Figures 33 – 35 show the MPPE data mode and the corresponding data products of LEP and HEP sensors for L-mode, M-mode, and H-mode data, respectively.

5 Conclusion

All of the MPPE analyzers have concluded initial commissioning with no significant problems reported. Because MOSIF blocks most of the FOVs of the MPPE sensors, it will be difficult for the ion sensors (MIA, MSA, and HEP-ion) to measure the solar wind during the cruise phase before arriving at Mercury. Only the low energy electron sensors MEA1 and MEA2 can measure part of the solar wind electron phase space density because the thermal speed of electrons is higher than the solar wind bulk velocity. During the Earth, Venus, and Mercury fly-bys, we expect most of the MPPE sensors to be turned on. If BepiColmbo will pass through magnetosphere, the ion sensors might also be able to measure natural counts. Therefore, events provide good opportunities to check the analyzer functions including the data processing software using natural data.

During the Venus fly-bys scheduled in October 2020 and August 2021, we plan to use MEA1, MEA2, MIA, MSA, HEP-ele, and ENA to make observations. MEA1 and MEA2 will be able to observe electrons in the solar wind and around Venus, and ENA might be capable of measuring the energetic neutral atoms from Venus. Although it may be difficult for MIA and MSA to obtain meaningful ion data, activating the instrument and operating the analyzers will refresh the instrument operation skills and facilitate observation immediately after arriving at Mercury. During the Mercury fly-bys scheduled in October 2021, June 2022, June 2023, September 2024, December 2024 and January 2025, the MPPE sensors will be activated; detailed observation plans will be considered in the future. After arriving at Mercury in December 2025, all of the MPPE analyzers will make continuous

observations except for periods in which the operations are limited owing to the thermal constraints of the spacecraft.

Conflict of interest

The authors declare that they have no conflict of interest.

References

Amano T, Katou T, Kitamura N, Oka M, Matsumoto Y, Hoshino M, Saito Y, Yokota S, Giles BL, Paterson WR, Russell CT, Le Contel O, Ergun RE, Lindqvist PA, Turner DL, Fennell JF, Blake JB (2020) Observational evidence for stochastic shock drift acceleration of electrons at the earth's bow shock. Phys Rev Lett 124:065101, DOI 10.1103/PhysRevLett.124.065101, URL https://link.aps.org/doi/10.1103/PhysRevLett.124.065101

Anderson BJ, Johnson CL, Korth H, Purucker ME, Winslow RM, Slavin JA, Solomon SC, McNutt RL, Raines JM, Zurbuchen TH (2011) The global magnetic field of mercury from messenger orbital observations. Science 333(6051):1859–1862, DOI 10.1126/science.1211001, URL https://science.sciencemag.org/content/333/6051/1859, https://science.sciencemag.org/content/333/6051/1859.full.pdf

Anderson BJ, Johnson CL, Korth H, Slavin JA, Winslow RM, Phillips RJ, McNutt Jr RL, Solomon SC (2014) Steady-state field-aligned currents at mercury.

Geophysical Research Letters 41(21):7444–7452, DOI 10.1002/2014GL061677,

URL https://agupubs.onlinelibrary.wiley.com/doi/abs/10.1002/2014GL061677,

https://agupubs.onlinelibrary.wiley.com/doi/pdf/10.1002/2014GL061677

Barabash S, Lundin R, Andersson H, Brinkfeldt K, Grigoriev A, Gunell H, Holm-
ström M, Yamauchi M, Asamura K, Bochsler P, Wurz P, Cerulli-Irelli R, Mura
A, Milillo A, Maggi M, Orsini S, Coates AJ, Linder DR, Kataria DO, Cur-
tis CC, Hsieh KC, Sandel BR, Frahm RA, Sharber JR, Winningham JD,
Grande M, Kallio E, Koskinen H, Riihelä P, Schmidt W, Säles T, Kozyra
JU, Krupp N, Woch J, Livi S, Luhmann JG, McKenna-Lawlor S, Roelof EC,
Williams DJ, Sauvaud JA, Fedorov A, Thocaven JJ (2006) The analyzer of
space plasmas and energetic atoms (aspera-3) for the mars express mission.
Space Science Reviews 126(1):113–164, DOI 10.1007/s11214-006-9124-8, URL
https://doi.org/10.1007/s11214-006-9124-8

Barabash S, Sauvaud JA, Gunell H, Andersson H, Grigoriev A, Brinkfeldt K,
Holmström M, Lundin R, Yamauchi M, Asamura K, Baumjohann W, Zhang
T, Coates A, Linder D, Kataria D, Curtis C, Hsieh K, Sandel B, Fedorov
A, Mazelle C, Thocaven JJ, Grande M, Koskinen HE, Kallio E, Säles T,
Riihela P, Kozyra J, Krupp N, Woch J, Luhmann J, McKenna-Lawlor S,
Orsini S, Cerulli-Irelli R, Mura M, Milillo M, Maggi M, Roelof E, Brandt
P, Russell C, Szego K, Winningham J, Frahm R, Scherrer J, Sharber J,
Wurz P, Bochsler P (2007) The analyser of space plasmas and energetic
atoms (aspera-4) for the venus express mission. Planetary and Space Science
55(12):1772 – 1792, DOI https://doi.org/10.1016/j.pss.2007.01.014, URL
http://www.sciencedirect.com/science/article/pii/S003206330700013X,   the
Planet Venus and the Venus Express Mission, Part 2

Cassidy TA, Merkel AW, Burger MH, Sarantos M, Killen RM, McClintock WE, Vervack RJ (2015) Mercury's seasonal sodium exosphere: Messenger orbital observations. Icarus 248:547 – 559, DOI https://doi.org/10.1016/j.icarus.2014.10.037, URL http://www.sciencedirect.com/science/article/pii/S0019103514005843

Cliver EW, Feynman J, Garrett HB (1990) An estimate of the maximum speed of the solar wind, 1938-1989. Journal of Geophysical Research: Space Physics 95(A10):17103–17112, DOI 10.1029/JA095iA10p17103, URL https://agupubs.onlinelibrary.wiley.com/doi/abs/10.1029/JA095iA10p17103, https://agupubs.onlinelibrary.wiley.com/doi/pdf/10.1029/JA095iA10p17103

Delcourt D, Saito Y, Leblanc F, Verdeil C, Yokota S, Fraenz M, Fischer H, Fiethe B, Katra B, Fontaine D, Illiano JM, Berthelier JJ, Krupp N, Buhrke U, Bubenhagen F, Michalik H (2016) The mass spectrum analyzer (msa) on board the bepicolombo mmo. Journal of Geophysical Research: Space Physics 121(7):6749–6761, DOI 10.1002/2016JA022380, URL https://agupubs.onlinelibrary.wiley.com/doi/abs/10.1002/2016JA022380, https://agupubs.onlinelibrary.wiley.com/doi/pdf/10.1002/2016JA022380

Delcourt DC, Grimald S, Leblanc F, Berthelier JJ, Millilo A, Mura A, Orsini S, Moore TE (2003) A quantitative model of the planetary na$^+$ contribution to mercury's magnetosphere. Annales Geophysicae 21(8):1723–1736, DOI 10.5194/angeo-21-1723-2003, URL https://www.ann-geophys.net/21/1723/2003/

Desai MI, Mason GM, Wiedenbeck ME, Cohen CMS, Mazur JE, Dwyer JR, Gold RE, Krimigis SM, Hu Q, Smith CW, Skoug RM (2004) Spectral properties of heavy ions associated with the passage of interplanetary shocks at 1

AU. The Astrophysical Journal 611(2):1156–1174, DOI 10.1086/422211, URL https://doi.org/10.1086/422211

Dewey RM, Slavin JA, Raines JM, Baker DN, Lawrence DJ (2017) Energetic electron acceleration and injection during dipolarization events in mercury's magnetotail. Journal of Geophysical Research: Space Physics 122(12):12,170–12,188, DOI https://doi.org/10.1002/2017JA024617, URL https://agupubs.onlinelibrary.wiley.com/doi/abs/10.1002/2017JA024617, https://agupubs.onlinelibrary.wiley.com/doi/pdf/10.1002/2017JA024617

DiBraccio GA, Slavin JA, Imber SM, Gershman DJ, Raines JM, Jackman CM, Boardsen SA, Anderson BJ, Korth H, Zurbuchen TH, McNutt RL, Solomon SC (2015) Messenger observations of flux ropes in mercury's magnetotail. Planetary and Space Science 115:77 – 89, DOI https://doi.org/10.1016/j.pss.2014.12.016, URL http://www.sciencedirect.com/science/article/pii/S0032063314004085, solar wind interaction with the terrestrial planets

Fatemi S, Poppe AR, Barabash S (2020) Hybrid simulations of solar wind proton precipitation to the surface of mercury. Journal of Geophysical Research: Space Physics 125(4):e2019JA027706, DOI 10.1029/2019JA027706, URL https://agupubs.onlinelibrary.wiley.com/doi/abs/10.1029/2019JA027706, e2019JA027706 10.1029/2019JA027706, https://agupubs.onlinelibrary.wiley.com/doi/pdf/10.1029/2019JA027706

Fisk LA, Gloeckler G (2012) Particle acceleration in the heliosphere: Implications for astrophysics. Space Science Reviews 173(1):433–458, DOI 10.1007/s11214-012-9899-8, URL https://doi.org/10.1007/s11214-012-9899-8

Fox NJ, Velli MC, Bale SD, Decker R, Driesman A, Howard RA, Kasper JC, Kinnison J, Kusterer M, Lario D, Lockwood MK, McComas DJ, Raouafi NE, Szabo A (2016) The solar probe plus mission: Humanity's first visit to our

star. Space Science Reviews 204(1):7–48, DOI 10.1007/s11214-015-0211-6, URL
https://doi.org/10.1007/s11214-015-0211-6

Funsten HO, Ritzau SM, Harper RW (2001) Negative helium ions exiting a carbon
foil at kev energies. Phys Rev B 63:155416, DOI 10.1103/PhysRevB.63.155416,
URL https://link.aps.org/doi/10.1103/PhysRevB.63.155416

Funsten HO, Harper RW, McComas DJ (2005) Absolute detection efficiency
of space-based ion mass spectrometers and neutral atom imagers. Re-
view of Scientific Instruments 76(5):053301, DOI 10.1063/1.1889465, URL
https://doi.org/10.1063/1.1889465, https://doi.org/10.1063/1.1889465

Futaana Y, Barabash S, Wieser M, Wurz P, Hurley D, Horányi M, Mall U,
Andre N, Ivchenko N, Oberst J, Retherford K, Coates A, Masters A, Wahlund
JE, Kallio E (2018) Selma mission: How do airless bodies interact with space
environment? the moon as an accessible laboratory. Planetary and Space
Science 156:23 – 40, DOI https://doi.org/10.1016/j.pss.2017.11.002, URL
http://www.sciencedirect.com/science/article/pii/S0032063317302799, dust,
Atmosphere, and Plasma Environment of the Moon and Small Bodies

Galvin AB, Kistler LM, Popecki MA, Farrugia CJ, Simunac KDC, Ellis L, Möbius
E, Lee MA, Boehm M, Carroll J, Crawshaw A, Conti M, Demaine P, Ellis S,
Gaidos JA, Googins J, Granoff M, Gustafson A, Heirtzler D, King B, Knauss U,
Levasseur J, Longworth S, Singer K, Turco S, Vachon P, Vosbury M, Widholm
M, Blush LM, Karrer R, Bochsler P, Daoudi H, Etter A, Fischer J, Jost J,
Opitz A, Sigrist M, Wurz P, Klecker B, Ertl M, Seidenschwang E, Wimmer-
Schweingruber RF, Koeten M, Thompson B, Steinfeld D (2008) The plasma and
suprathermal ion composition (plastic) investigation on the stereo observatories.
Space Science Reviews 136(1):437–486, DOI 10.1007/s11214-007-9296-x, URL

1827   https://doi.org/10.1007/s11214-007-9296-x

1828   Gershman DJ, Slavin JA, Raines JM, Zurbuchen TH, Anderson BJ,
1829   Korth H, Baker DN, Solomon SC (2014) Ion kinetic properties in
1830   mercury's pre-midnight plasma sheet. Geophysical Research Letters
1831   41(16):5740–5747, DOI https://doi.org/10.1002/2014GL060468, URL
1832   https://agupubs.onlinelibrary.wiley.com/doi/abs/10.1002/2014GL060468,
1833   https://agupubs.onlinelibrary.wiley.com/doi/pdf/10.1002/2014GL060468

1834   Gershman DJ, Raines JM, Slavin JA, Zurbuchen TH, Sundberg T, Board-
1835   sen SA, Anderson BJ, Korth H, Solomon SC (2015) Messenger observa-
1836   tions of multiscale kelvin-helmholtz vortices at mercury. Journal of Geophys-
1837   ical Research: Space Physics 120(6):4354–4368, DOI 10.1002/2014JA020903,
1838   URL https://agupubs.onlinelibrary.wiley.com/doi/abs/10.1002/2014JA020903,
1839   https://agupubs.onlinelibrary.wiley.com/doi/pdf/10.1002/2014JA020903

1840   Grande M (1997) Investigation of magnetospheric interactions with
1841   the hermean surface. Advances in Space Research 19(10):1609
1842   – 1614, DOI https://doi.org/10.1016/S0273-1177(97)00374-8, URL
1843   http://www.sciencedirect.com/science/article/pii/S0273117797003748, pro-
1844   ceedings of the BO.1 Symposium of COSPAR Scientific Commission B

1845   Hasegawa H, Fujimoto M, Phan TD, Rème H, Balogh A, Dunlop MW, Hashimoto
1846   C, TanDokoro R (2004) Transport of solar wind into earth's magnetosphere
1847   through rolled-up kelvin–helmholtz vortices. Nature 430(7001):755–758, DOI
1848   10.1038/nature02799, URL https://doi.org/10.1038/nature02799

1849   Heyner D, Nabert C, Liebert E, Glassmeier KH (2016) Concerning reconnection-
1850   induction balance at the magnetopause of mercury. Journal of Geophysi-
1851   cal Research: Space Physics 121(4):2935–2961, DOI 10.1002/2015JA021484,

URL https://agupubs.onlinelibrary.wiley.com/doi/abs/10.1002/2015JA021484,

https://agupubs.onlinelibrary.wiley.com/doi/pdf/10.1002/2015JA021484

Ho GC, Lario D, Decker RB, Smith CW, Hu Q (2008) Transient shocks and associated energetic particle distributions observed by ace during cycle 23. AIP Conference Proceedings 1039(1):184–189, DOI 10.1063/1.2982443, URL https://aip.scitation.org/doi/abs/10.1063/1.2982443, https://aip.scitation.org/doi/pdf/10.1063/1.2982443

Ho GC, Krimigis SM, Gold RE, Baker DN, Slavin JA, Anderson BJ, Korth H, Starr RD, Lawrence DJ, McNutt RL, Solomon SC (2011) Messenger observations of transient bursts of energetic electrons in mercury's magnetosphere. Science 333(6051):1865–1868, DOI 10.1126/science.1211141, URL https://science.sciencemag.org/content/333/6051/1865, https://science.sciencemag.org/content/333/6051/1865.full.pdf

Hovestadt D, Hilchenbach M, Bürgi A, Klecker B, Laeverenz P, Scholer M, Grünwaldt H, Axford WI, Livi S, Marsch E, Wilken B, Winterhoff HP, Ipavich FM, Bedini P, Coplan MA, Galvin AB, Gloeckler G, Bochsler P, Balsiger H, Fischer J, Geiss J, Kallenbach R, Wurz P, Reiche KU, Gliem F, Judge DL, Ogawa HS, Hsieh KC, Möbius E, Lee MA, Managadze GG, Verigin MI, Neugebauer M (1995) Celias - charge, element and isotope analysis system for soho. Solar Physics 162(1):441–481, DOI 10.1007/BF00733436, URL https://doi.org/10.1007/BF00733436

Hundhausen AJ, Holzer TE, Low BC (1987) Do slow shocks precede some coronal mass ejections? Journal of Geophysical Research: Space Physics 92(A10):11173–11178, DOI 10.1029/JA092iA10p11173, URL https://agupubs.onlinelibrary.wiley.com/doi/abs/10.1029/JA092iA10p11173,

https://agupubs.onlinelibrary.wiley.com/doi/pdf/10.1029/JA092iA10p11173

Imber SM, Slavin JA (2017) Messenger observations of magnetotail loading and unloading: Implications for substorms at mercury. Journal of Geophysical Research: Space Physics 122(11):11,402–11,412, DOI 10.1002/2017JA024332, URL https://agupubs.onlinelibrary.wiley.com/doi/abs/10.1002/2017JA024332, https://agupubs.onlinelibrary.wiley.com/doi/pdf/10.1002/2017JA024332

Imber SM, Slavin JA, Boardsen SA, Anderson BJ, Korth H, McNutt Jr RL, Solomon SC (2014) Messenger observations of large dayside flux transfer events: Do they drive mercury's substorm cycle? Journal of Geophysical Research: Space Physics 119(7):5613–5623, DOI 10.1002/2014JA019884, URL https://agupubs.onlinelibrary.wiley.com/doi/abs/10.1002/2014JA019884, https://agupubs.onlinelibrary.wiley.com/doi/pdf/10.1002/2014JA019884

Ip WH (1986) The sodium exosphere and magnetosphere of mercury. Geophysical Research Letters 13(5):423–426, DOI 10.1029/GL013i005p00423, URL https://agupubs.onlinelibrary.wiley.com/doi/abs/10.1029/GL013i005p00423, https://agupubs.onlinelibrary.wiley.com/doi/pdf/10.1029/GL013i005p00423

Kallio E, Janhunen P (2003) Solar wind and magnetospheric ion impact on mercury's surface. Geophysical Research Letters 30(17), DOI 10.1029/2003GL017842, URL https://agupubs.onlinelibrary.wiley.com/doi/abs/10.1029/2003GL017842, https://agupubs.onlinelibrary.wiley.com/doi/pdf/10.1029/2003GL017842

Kasaba Y, Takashima T, Matsuda S, Eguchi S, Endo M, Miyabara T, Taeda M, Kuroda Y, Kasahara Y, Imachi T, Kojima H, Yagitani S, Moncuquet M, Wahlund JE, Kumamoto A, Matsuoka A, Baumjohann W, Yokota S, Asamura K, Saito Y, Delcourt D, Hirahara M, Barabash S, Andre N, Kobayashi

M, Yoshikawa I, Murakami G, Hayakawa H (2020) Mission data processor aboard the bepicolombo mio spacecraft: Design and scientific operation concept. Space Science Reviews 216(3):34, DOI 10.1007/s11214-020-00658-x, URL https://doi.org/10.1007/s11214-020-00658-x

Kasahara S, Mitani T, Ogasawara K, Takashima T, Hirahara M, Asamura K (2009) Application of single-sided silicon strip detector to energy and charge state measurements of medium energy ions in space. Nuclear Instruments and Methods in Physics Research Section A: Accelerators, Spectrometers, Detectors and Associated Equipment 603(3):355 – 360, DOI https://doi.org/10.1016/j.nima.2009.02.004, URL http://www.sciencedirect.com/science/article/pii/S0168900209003441

Kazama Y, Barabash S, Wieser M, Asamura K, Wurz P (2009) A lena instrument onboard bepicolombo and chandrayaan?1. AIP Conference Proceedings 1144(1):109–113, DOI 10.1063/1.3169273, URL https://aip.scitation.org/doi/abs/10.1063/1.3169273, https://aip.scitation.org/doi/pdf/10.1063/1.3169273

Killen RM, Potter AE, Reiff P, Sarantos M, Jackson BV, Hick P, Giles B (2001) Evidence for space weather at mercury. Journal of Geophysical Research: Planets 106(E9):20509–20525, DOI 10.1029/2000JE001401, URL https://agupubs.onlinelibrary.wiley.com/doi/abs/10.1029/2000JE001401, https://agupubs.onlinelibrary.wiley.com/doi/pdf/10.1029/2000JE001401

Lario D (2005) Advances in modeling gradual solar energetic particle events. Advances in Space Research 36(12):2279 – 2288, DOI https://doi.org/10.1016/j.asr.2005.07.081, URL http://www.sciencedirect.com/science/article/pii/S0273117705009865, space

1927   Weather

1928   Lario D, Ho GC, Decker RB, Roelof EC, Desai MI, Smith CW (2003)
1929   Ace observations of energetic particles associated with transient in-
1930   terplanetary shocks. AIP Conference Proceedings 679(1):640–643, DOI
1931   10.1063/1.1618676, URL https://aip.scitation.org/doi/abs/10.1063/1.1618676,
1932   https://aip.scitation.org/doi/pdf/10.1063/1.1618676

1933   Lavraud B, Borovsky JE (2008) Altered solar wind-magnetosphere interaction
1934   at low mach numbers: Coronal mass ejections. Journal of Geophysical Re-
1935   search: Space Physics 113(A9), DOI https://doi.org/10.1029/2008JA013192,
1936   URL https://agupubs.onlinelibrary.wiley.com/doi/abs/10.1029/2008JA013192,
1937   https://agupubs.onlinelibrary.wiley.com/doi/pdf/10.1029/2008JA013192

1938   Leblanc F, Johnson R (2010) Mercury exosphere i. global cir-
1939   culation model of its sodium component. Icarus 209(2):280
1940   – 300, DOI https://doi.org/10.1016/j.icarus.2010.04.020, URL
1941   http://www.sciencedirect.com/science/article/pii/S0019103510001776

1942   Liljeblad E, Sundberg T, Karlsson T, Kullen A (2014) Statistical investigation of
1943   kelvin-helmholtz waves at the magnetopause of mercury. Journal of Geophys-
1944   ical Research: Space Physics 119(12):9670–9683, DOI 10.1002/2014JA020614,
1945   URL https://agupubs.onlinelibrary.wiley.com/doi/abs/10.1002/2014JA020614,
1946   https://agupubs.onlinelibrary.wiley.com/doi/pdf/10.1002/2014JA020614

1947   Lindsay ST, James MK, Bunce EJ, Imber SM, Korth H, Martindale A,
1948   Yeoman TK (2016) Messenger x-ray observations of magnetosphere–
1949   surface interaction on the nightside of mercury. Planetary and Space
1950   Science 125:72–79, DOI https://doi.org/10.1016/j.pss.2016.03.005, URL
1951   http://www.sciencedirect.com/science/article/pii/S0032063315301501

Machida S, Saito Y, Ito Y, Hayakawa H (1998) Instrumental characteristics of the electron spectrum analyzer (esa) onboard the planet-b mission and observational perspectives of the electron measurements. Earth, Planets and Space 50(3):207–211, DOI 10.1186/BF03352105, URL https://doi.org/10.1186/BF03352105

Marti A, Schletti R, Wurz P, Bochsler P (2001) Calibration facility for solar wind plasma instrumentation. Review of Scientific Instruments 72(2):1354–1360, DOI 10.1063/1.1340020, URL https://aip.scitation.org/doi/abs/10.1063/1.1340020, https://aip.scitation.org/doi/pdf/10.1063/1.1340020

Massetti S, Orsini S, Milillo A, Mura A, Angelis ED, Lammer H, Wurz P (2003) Mapping of the cusp plasma precipitation on the surface of mercury. Icarus 166(2):229 – 237, DOI https://doi.org/10.1016/j.icarus.2003.08.005, URL http://www.sciencedirect.com/science/article/pii/S0019103503002562

Masters A, Phan TD, Badman SV, Hasegawa H, Fujimoto M, Russell CT, Coates AJ, Dougherty MK (2014) The plasma depletion layer in saturn's magnetosheath. Journal of Geophysical Research: Space Physics 119(1):121–130, DOI 10.1002/2013JA019516, URL https://agupubs.onlinelibrary.wiley.com/doi/abs/10.1002/2013JA019516, https://agupubs.onlinelibrary.wiley.com/doi/pdf/10.1002/2013JA019516

Milillo A, Wurz P, Orsini S, Delcourt D, Kallio E, KILLEN RM, Lammer H, Massetti S, Mura A, Barabash S, Cremonese G, Daglis IA, De Angelis E, Di Lellis AM, Livi S, Mangano V, Torkar K (2005) Surface-exosphere-magnetosphere system of mercury. Space Science Reviews 117(3):397–443, DOI 10.1007/s11214-005-3593-z, URL https://doi.org/10.1007/s11214-005-3593-z

Mitani T, Takashima T, Kasahara S, Miyake W, Hirahara M (2018) High-energy electron experiments (hep) aboard the erg (arase) satellite.

1977 Earth, Planets and Space 70(1):77, DOI 10.1186/s40623-018-0853-1, URL
1978 https://doi.org/10.1186/s40623-018-0853-1

1979 Miyake W, Saito Y, Harada M, Saito M, Hasegawa H, Ieda A, Machida S, Nagai
1980 T, Nagatsuma T, Seki K, Shinohara I, Terasawa T (2009) Mercury ion analyzer
1981 (mia) onboard mercury magnetospheric orbiter: Mmo. Advances in Space Re-
1982 search 43(12):1986 – 1992, DOI https://doi.org/10.1016/j.asr.2009.03.011, URL
1983 http://www.sciencedirect.com/science/article/pii/S0273117709001951

1984 Mukai T, Ogasawara K, Saito Y (2004) An empirical model of the plasma
1985 environment around mercury. Advances in Space Research 33(12):2166
1986 – 2171, DOI https://doi.org/10.1016/S0273-1177(03)00443-5, URL
1987 http://www.sciencedirect.com/science/article/pii/S0273117703004435, mer-
1988 cury, Mars and Saturn

1989 Müller D, Marsden RG, St Cyr OC, Gilbert HR, Team TSO (2013) So-
1990 lar orbiter. Solar Physics 285(1):25–70, DOI 10.1007/s11207-012-0085-7, URL
1991 https://doi.org/10.1007/s11207-012-0085-7

1992 Mura A, Wurz P, Lichtenegger HI, Schleicher H, Lammer H, Delcourt D, Milillo
1993 A, Orsini S, Massetti S, Khodachenko ML (2009) The sodium exosphere of
1994 mercury: Comparison between observations during mercury's transit and model
1995 results. Icarus 200(1):1 – 11, DOI https://doi.org/10.1016/j.icarus.2008.11.014,
1996 URL http://www.sciencedirect.com/science/article/pii/S0019103508004107

1997 Nakamura TKM, Hasegawa H, Daughton W, Eriksson S, Li WY, Nakamura R
1998 (2017) Turbulent mass transfer caused by vortex induced reconnection in col-
1999 lisionless magnetospheric plasmas. Nature Communications 8(1):1582, DOI
2000 10.1038/s41467-017-01579-0, URL https://doi.org/10.1038/s41467-017-01579-0

van Nes P, Reinhard R, Sanderson TR, Wenzel KP, Zwickl RD (1984) The energy spectrum of 35- to 1600-kev protons associated with interplanetary shocks. Journal of Geophysical Research: Space Physics 89(A4):2122–2132, DOI 10.1029/JA089iA04p02122, URL https://agupubs.onlinelibrary.wiley.com/doi/abs/10.1029/JA089iA04p02122, https://agupubs.onlinelibrary.wiley.com/doi/pdf/10.1029/JA089iA04p02122

Ness NF, Behannon KW, Lepping RP, Whang YC, Schatten KH (1974) Magnetic field observations near mercury: Preliminary results from mariner 10. Science 185(4146):151–160, DOI 10.1126/science.185.4146.151, URL https://science.sciencemag.org/content/185/4146/151, https://science.sciencemag.org/content/185/4146/151.full.pdf

Nishino MN, Fujimoto M, Phan TD, Mukai T, Saito Y, Kuznetsova MM, Rastätter L (2008) Anomalous flow deflection at earth's low-alfvén-mach-number bow shock. Phys Rev Lett 101:065003, DOI 10.1103/PhysRevLett.101.065003, URL https://link.aps.org/doi/10.1103/PhysRevLett.101.065003

Ogilvie KW, Scudder JD, Hartle RE, Siscoe GL, Bridge HS, Lazarus AJ, Asbridge JR, Bame SJ, Yeates CM (1974) Observations at mercury encounter by the plasma science experiment on mariner 10. Science 185(4146):145–151, DOI 10.1126/science.185.4146.145, URL https://science.sciencemag.org/content/185/4146/145, https://science.sciencemag.org/content/185/4146/145.full.pdf

Oka M, Otsuka F, Matsukiyo S, Wilson LB, Argall MR, Amano T, Phan TD, Hoshino M, Contel OL, Gershman DJ, Burch JL, Torbert RB, Dorelli JC, Giles BL, Ergun RE, Russell CT, Lindqvist PA (2019) Electron scattering by low-frequency whistler waves at earth's bow shock. The Astrophysical Journal

886(1):53, DOI 10.3847/1538-4357/ab4a81, URL https://doi.org/10.3847/1538-4357/ab4a81

Parker E (1958) Dynamics of the Interplanetary Gas and Magnetic Fields. The Astrophysical Journal 128:664, DOI 10.1086/146579

Saito Y, Sauvaud J, Hirahara M, Barabash S, Delcourt D, Takashima T, Asamura K (2010a) Scientific objectives and instrumentation of mercury plasma particle experiment (mppe) onboard mmo. Planetary and Space Science 58(1):182 – 200, DOI https://doi.org/10.1016/j.pss.2008.06.003, URL http://www.sciencedirect.com/science/article/pii/S0032063308001529, comprehensive Science Investigations of Mercury: The scientific goals of the joint ESA/JAXA mission BepiColombo

Saito Y, Yokota S, Asamura K, Tanaka T, Nishino MN, Yamamoto T, Terakawa Y, Fujimoto M, Hasegawa H, Hayakawa H, Hirahara M, Hoshino M, Machida S, Mukai T, Nagai T, Nagatsuma T, Nakagawa T, Nakamura M, Oyama Ki, Sagawa E, Sasaki S, Seki K, Shinohara I, Terasawa T, Tsunakawa H, Shibuya H, Matsushima M, Shimizu H, Takahashi F (2010b) In-flight performance and initial results of plasma energy angle and composition experiment (pace) on selene (kaguya). Space Science Reviews 154(1):265–303, DOI 10.1007/s11214-010-9647-x, URL https://doi.org/10.1007/s11214-010-9647-x

Saito Y, Yokota S, Asamura K, Krieger A (2017) High-speed mcp anodes for high time resolution low-energy charged particle spectrometers. Journal of Geophysical Research: Space Physics 122(2):1816–1830, DOI 10.1002/2016JA023157, URL https://agupubs.onlinelibrary.wiley.com/doi/abs/10.1002/2016JA023157, https://agupubs.onlinelibrary.wiley.com/doi/pdf/10.1002/2016JA023157

Sarantos M, Slavin JA (2009) On the possible formation of alfvén wings at mercury during encounters with coronal mass ejections. Geophysical Research Letters 36(4), DOI 10.1029/2008GL036747, URL https://agupubs.onlinelibrary.wiley.com/doi/abs/10.1029/2008GL036747, https://agupubs.onlinelibrary.wiley.com/doi/pdf/10.1029/2008GL036747

Sauvaud JA, Fedorov A, Aoustin C, Seran HC, Comte EL, Petiot M, Rouzaud J, Saito Y, Dandouras J, Jacquey C, Louarn P, Mazelle C, Médale JL (2010) The mercury electron analyzers for the bepi colombo mission. Advances in Space Research 46(9):1139 – 1148, DOI https://doi.org/10.1016/j.asr.2010.05.022, URL http://www.sciencedirect.com/science/article/pii/S0273117710003674

Schriver D, Trávníček PM, Anderson BJ, Ashour-Abdalla M, Baker DN, Benna M, Boardsen SA, Gold RE, Hellinger P, Ho GC, Korth H, Krimigis SM, McNutt Jr RL, Raines JM, Richard RL, Slavin JA, Solomon SC, Starr RD, Zurbuchen TH (2011) Quasi-trapped ion and electron populations at mercury. Geophysical Research Letters 38(23), DOI 10.1029/2011GL049629, URL https://agupubs.onlinelibrary.wiley.com/doi/abs/10.1029/2011GL049629, https://agupubs.onlinelibrary.wiley.com/doi/pdf/10.1029/2011GL049629

Shimada N, Terasawa T, Hoshino M, Naito T, Matsui H, Koi T, Maezawa K (1998) Diffusive shock acceleration of electrons at an interplanetary shock observed on 21 feb 1994. Astrophysics and Space Science 264(1):481–488, DOI 10.1023/A:1002499513777, URL https://doi.org/10.1023/A:1002499513777

Shinohara I, Fujimoto M (2005) Formation of thin electron current layer associated with lower hybrid drift instability and its relation to quick reconnection triggering. In: Hoshohino M, Omura Y, Lanzerotti L (eds) Frontiers in Magnetospheric Plasma Physics, COSPAR Colloquia Series, vol 16, Perga-

mon, pp 123 – 129, DOI https://doi.org/10.1016/S0964-2749(05)80019-8, URL http://www.sciencedirect.com/science/article/pii/S0964274905800198

Sigmund P, Oliva A, Falcone G (1982) Sputtering of multicomponent materials: Elements of a theory. Nuclear Instruments and Methods in Physics Research 194(1):541 – 548, DOI https://doi.org/10.1016/0029-554X(82)90578-X, URL http://www.sciencedirect.com/science/article/pii/0029554X8290578X

Simpson J, Eraker J, Lamport J, Walpole P (1974) Electrons and protons accelerated in mercury's magnetic field. Science (New York, NY) 185:160–6, DOI 10.1126/science.185.4146.160

Slavin J (2004) Mercury's magnetosphere. Advances in Space Research 33(11):1859 – 1874, DOI https://doi.org/10.1016/j.asr.2003.02.019, URL http://www.sciencedirect.com/science/article/pii/S0273117704000092, comparative Magnetospheres

Slavin JA, Imber SM, Boardsen SA, DiBraccio GA, Sundberg T, Sarantos M, Nieves-Chinchilla T, Szabo A, Anderson BJ, Korth H, Zurbuchen TH, Raines JM, Johnson CL, Winslow RM, Killen RM, McNutt Jr RL, Solomon SC (2012) Messenger observations of a flux-transfer-event shower at mercury. Journal of Geophysical Research: Space Physics 117(A12), DOI 10.1029/2012JA017926, URL https://agupubs.onlinelibrary.wiley.com/doi/abs/10.1029/2012JA017926, https://agupubs.onlinelibrary.wiley.com/doi/pdf/10.1029/2012JA017926

Slavin JA, Baker DN, Gershman DJ, Ho GC, Imber SM, Krimigis SM, Sundberg T (2018) Mercury's dynamic magnetosphere. In: Mercury: The View after MESSENGER, Cambridge Planetary Science, Cambridge University Press, Cambridge, pp 461–496, DOI 10.1017/9781316650684.018

Slavin JA, Middleton HR, Raines JM, Jia X, Zhong J, Sun WJ, Livi S, Imber SM, Poh GK, Akhavan-Tafti M, Jasinski J, DiBraccio GA, Dong C, Dewey RM, Mays ML (2019) Messenger observations of disappearing dayside magnetosphere events at mercury. Journal of Geophysical Research: Space Physics 124(8):6613–6635, DOI 10.1029/2019JA026892, URL https://agupubs.onlinelibrary.wiley.com/doi/abs/10.1029/2019JA026892, https://agupubs.onlinelibrary.wiley.com/doi/pdf/10.1029/2019JA026892

Smart DF, Shea MA (1985) A simplified model for timing the arrival of solar flare-initiated shocks. Journal of Geophysical Research: Space Physics 90(A1):183–190, DOI 10.1029/JA090iA01p00183, URL https://agupubs.onlinelibrary.wiley.com/doi/abs/10.1029/JA090iA01p00183, https://agupubs.onlinelibrary.wiley.com/doi/pdf/10.1029/JA090iA01p00183

Sun WJ, Raines JM, Fu SY, Slavin JA, Wei Y, Poh GK, Pu ZY, Yao ZH, Zong QG, Wan WX (2017) Messenger observations of the energization and heating of protons in the near-mercury magnetotail. Geophysical Research Letters 44(16):8149–8158, DOI 10.1002/2017GL074276, URL https://agupubs.onlinelibrary.wiley.com/doi/abs/10.1002/2017GL074276, https://agupubs.onlinelibrary.wiley.com/doi/pdf/10.1002/2017GL074276

Tsurutani BT, Lin RP (1985) Acceleration of >47 kev ions and >2 kev electrons by interplanetary shocks at 1 au. Journal of Geophysical Research: Space Physics 90(A1):1–11, DOI 10.1029/JA090iA01p00001, URL https://agupubs.onlinelibrary.wiley.com/doi/abs/10.1029/JA090iA01p00001, https://agupubs.onlinelibrary.wiley.com/doi/pdf/10.1029/JA090iA01p00001

Wang C, Du D, Richardson JD (2005) Characteristics of the interplanetary coronal mass ejections in the heliosphere between 0.3 and 5.4 au. Journal of

Geophysical Research: Space Physics 110(A10), DOI 10.1029/2005JA011198, URL https://agupubs.onlinelibrary.wiley.com/doi/abs/10.1029/2005JA011198, https://agupubs.onlinelibrary.wiley.com/doi/pdf/10.1029/2005JA011198

Watanabe S, Tajima H, Fukazawa Y, Ichinohe Y, Takeda S, Enoto T, Fukuyama T, Furui S, Genba K, Hagino K, Harayama A, Kuroda Y, Matsuura D, Nakamura R, Nakazawa K, Noda H, Odaka H, Ohta M, Onishi M, Saito S, Sato G, Sato T, Takahashi T, Tanaka T, Togo A, Tomizuka S (2014) The si/cdte semiconductor compton camera of the astro-h soft gamma-ray detector (sgd). Nuclear Instruments and Methods in Physics Research Section A: Accelerators, Spectrometers, Detectors and Associated Equipment 765:192 – 201, DOI https://doi.org/10.1016/j.nima.2014.05.127, URL http://www.sciencedirect.com/science/article/pii/S0168900214008250, hSTD-9 2013 - Proceedings of the 9th International Hiroshima Symposium on Development and Application of Semiconductor Tracking Detectors

Whang YC (1977) Magnetospheric magnetic field of mercury. Journal of Geophysical Research (1896-1977) 82(7):1024–1030, DOI 10.1029/JA082i007p01024, URL https://agupubs.onlinelibrary.wiley.com/doi/abs/10.1029/JA082i007p01024, https://agupubs.onlinelibrary.wiley.com/doi/pdf/10.1029/JA082i007p01024

Wieser M, Wurz P (2005) Production of a 10 eV–1000 eV neutral particle beam using surface neutralization. Measurement Science and Technology 16(12):2511–2516, DOI 10.1088/0957-0233/16/12/016, URL https://iopscience.iop.org/article/10.1088/0957-0233/16/12/016

Winslow RM, Anderson BJ, Johnson CL, Slavin JA, Korth H, Purucker ME, Baker DN, Solomon SC (2013) Mercury's magnetopause and bow

shock from messenger magnetometer observations. Journal of Geophysical Research: Space Physics 118(5):2213–2227, DOI 10.1002/jgra.50237, URL https://agupubs.onlinelibrary.wiley.com/doi/abs/10.1002/jgra.50237, https://agupubs.onlinelibrary.wiley.com/doi/pdf/10.1002/jgra.50237

Winslow RM, Lugaz N, Philpott LC, Schwadron NA, Farrugia CJ, Anderson BJ, Smith CW (2015) Interplanetary coronal mass ejections from messenger orbital observations at mercury. Journal of Geophysical Research: Space Physics 120(8):6101–6118, DOI 10.1002/2015JA021200, URL https://agupubs.onlinelibrary.wiley.com/doi/abs/10.1002/2015JA021200, https://agupubs.onlinelibrary.wiley.com/doi/pdf/10.1002/2015JA021200

Wüest M, Evans D, Institute ISS, von Steiger R, Agency ES (2007) Calibration of Particle Instruments in Space Physics. ESA SR, ISSI, The International Space Science Institute, URL https://books.google.co.jp/books?id=hmBKNAAACAAJ

Wurz P, Lammer H (2003) Monte-carlo simulation of mercury's exosphere. Icarus 164(1):1 – 13, DOI https://doi.org/10.1016/S0019-1035(03)00123-4, URL http://www.sciencedirect.com/science/article/pii/S0019103503001234

Yagi M, Seki K, Matsumoto Y, Delcourt DC, Leblanc F (2010) Formation of a sodium ring in mercury's magnetosphere. Journal of Geophysical Research: Space Physics 115(A10), DOI 10.1029/2009JA015226, URL https://agupubs.onlinelibrary.wiley.com/doi/abs/10.1029/2009JA015226, https://agupubs.onlinelibrary.wiley.com/doi/pdf/10.1029/2009JA015226

Yagi M, Seki K, Matsumoto Y, Delcourt DC, Leblanc F (2017) Global structure and sodium ion dynamics in mercury's magnetosphere with the offset dipole. Journal of Geophysical Research: Space

Physics 122(11):10,990–11,002, DOI 10.1002/2017JA024082, URL https://agupubs.onlinelibrary.wiley.com/doi/abs/10.1002/2017JA024082, https://agupubs.onlinelibrary.wiley.com/doi/pdf/10.1002/2017JA024082

Young DT, Berthelier JJ, Blanc M, Burch JL, Coates AJ, Goldstein R, Grande M, Hill TW, Johnson RE, Kelha V, Mccomas DJ, Sittler EC, Svenes KR, Szegö K, Tanskanen P, Ahola K, Anderson D, Bakshi S, Baragiola RA, Barraclough BL, Black RK, Bolton S, Booker T, Bowman R, Casey P, Crary FJ, Delapp D, Dirks G, Eaker N, Funsten H, Furman JD, Gosling JT, Hannula H, Holm-lund C, Huomo H, Illiano JM, Jensen P, Johnson MA, Linder DR, Luntama T, Maurice S, Mccabe KP, Mursula K, Narheim BT, Nordholt JE, Preece A, Rudzki J, Ruitberg A, Smith K, Szalai S, Thomsen MF, Viherkanto K, Vilp-pola J, Vollmer T, Wahl TE, Wüest M, Ylikorpi T, Zinsmeyer C (2004) Cassini plasma spectrometer investigation. Space Science Reviews 114(1):1–112, DOI 10.1007/s11214-004-1406-4, URL https://doi.org/10.1007/s11214-004-1406-4

Zurbuchen TH, Raines JM, Slavin JA, Gershman DJ, Gilbert JA, Gloeckler G, Anderson BJ, Baker DN, Korth H, Krimigis SM, Sarantos M, Schriver D, McNutt RL, Solomon SC (2011) Messen-ger observations of the spatial distribution of planetary ions near mercury. Science 333(6051):1862–1865, DOI 10.1126/science.1211302, URL https://science.sciencemag.org/content/333/6051/1862, https://science.sciencemag.org/content/333/6051/1862.full.pdf

Table 1 Summary of MEA performance.

Field of view	$8° \times 360°$
Angular resolution	$22.5° \times 11.25°$
Energy range	3 eV–25,500 eV (Mercury mode)
	3 eV–3000 eV (solar wind mode)
Energy resolution	$\Delta E/E \sim 10\%$ (at full G-factor)
Stepping energies and cadence	Full energy sweep with 64 contiguous energy channels
	every 16 or 32 times per 4 s spin
Time resolution	Half a spin period, 2 s (using a single analyzer)
to obtain the full 3D	Quarter of a spin period, 1 s (using the two analyzers)
velocity distribution function	
Geometrical factor	
MEA1 max./min.	$4.0 \times 10^{-3}/6.7 \times 10^{-5}$ cm^2 sr eV/eV
MEA2 max./min.	$2.0 \times 10^{-4}/4.0 \times 10^{-6}$ cm^2 sr eV/eV
Mass	2.598 kg for MEA1+MEA2
	+ 0.460 kg for their thermal shields
Power	2.260 W (average for MEA1+MEA2)
	3.460 W (peak for MEA1+MEA2)
	1.880 W (stand-by for MEA1+MEA2)
Dimensions	177 mm $\times$ 120 mm ϕ (MEA1, MEA2)
Data rate	0.1 kbits/s (L-mdoe)
	2.5 kbits/s (M-mode)
	11 kbits/s (H-mode)
	after factor 3 compression
	for MEA1+MEA2

Table 2 MEA data products with time resolution as a function of MPPE mode and Mio telemetry mode.

MPPE MODE NAME	L-mode data products	M-mode data products	H-mode data products
	MEA1	**MEA1**	
1. Default Observation Mode	Et-OMN (4s)	Et-OMNm (4s)	N.A.
	Et-PAP (16s)	Et-PAP (4s)	
	VM (16s)	VM (4s)	
	3D-LL (640s)	3D-M (8s)	
		or 3D-M (4s)	
	MEA2	**MEA2**	
	Et-OMN (4s)	Et-OMNm (2s)	
	Et-PAP (16s)	Et-PAP (2s)	
	VM (16s)	VM (2s)	
	MEA1	**MEA1**	**MEA1**
2. Exospheric Mode	Et-OMN (4s)	Et-OMNm (4s)	3D-H (4s)
3. Solar Wind Mode	Et-PAP (16s)	Et-PAP (16s)	
/IP Shock Local Mode	VM (16s)	VM (4s)	
4. IP Shock Macro Mode	3D-LL (640s)	3D-M (8s)	
/Bow Shock Mode		or 3D-M (4s)	
5. Reconnection Mode			
6. Magnetospheric Mode	**MEA2**	**MEA2**	**MEA2**
	Et-OMN (4s)	Et-OMNm (2s)	3D-H (2s)
	Et-PAP (4s)	Et-PAP (2s)	
	VM (16s)	VM (2s)	

Table 3 MEA1 and MEA2 data products for the low-resolution telemetry mode (L-mode).

L-mode			
MEA1			
Data Product Name	**Description**	**Time Resolution (s)**	**Note**
Et-OMN	E-t count data 16 energy	4	
Et-PAP	E-t pitch angle data 4 energy × 16 pitch angle	16	
VM	velocity moment n (density) nVx, nVy, nVz (velocity) Pxx, Pyy, Pzz Pxy, Pyz, Pzx (pressure) qx, qy, qz (heat flux)	16	6 energy ranges 0: all energy steps above satellite potential * 2; 1-5: 5 energy steps below satellite potential * 2
3D-LL	3D count data 88 direction × 16 energy	640	
MEA2			
Data Product Name	**Description**	**Time Resolution (s)**	**Note**
Et-OMN	E-t count data 16 energy	4	
Et-PAP	E-t pitch angle data 4 energy x 16 pitch angle	16	
VM	velocity moment n (density) nVx, nVy, nVz (velocity) Pxx, Pyy, Pzz Pxy, Pyz, Pzx (pressure) qx, qy, qz (heat flux)	16	6 energy ranges 0: all energy steps above satellite potential * 2; 1-5: 5 energy steps below satellite potential * 2

Table 4 MEA1 and MEA2 data products for the medium-resolution telemetry mode (M-mode).

M-mode			
MEA1			
Data Product Name	**Description**	**Time Resolution (s)**	**Note**
Et-OMNm	E-t count data 32 energy	4	
Et-PAP	E-t pitch angle data 4 energy × 16 pitch angle	4	4 starting energy steps and width are selectable by commanding
VM	velocity moment n (density) nVx, nVy, nVz (velocity) Pxx, Pyy, Pzz Pxy, Pyz, Pzx (pressure) qx, qy, qz (heat flux)	4	6 energy ranges 0: all energy steps above satellite potential * 2; 1-5: 5 energy steps below satellite potential * 2
3D-M (8s)	3D count data 88 direction × 16 energy	8	(MPPE mode = 0 1 2 3 5)
3D-M (4s)	3D count data 88 direction × 16 energy	4	(MPPE mode = 4 6 7 8)
MEA2			
Data Product Name	**Description**	**Time Resolution (s)**	**Note**
Et-OMNm	E-t count data 32 energy	2	
Et-PAP	E-t pitch angle data 4 energy × 16 pitch angle	2	
VM	velocity moment n (density) nVx, nVy, nVz (velocity) Pxx, Pyy, Pzz Pxy, Pyz, Pzx (pressure) qx, qy, qz (heat flux)	2	6 energy ranges 0: all energy steps above satellite potential * 2; 1-5: 5 energy steps below satellite potential * 2

Table 5 MEA1 and MEA2 data products for the high-resolution telemetry mode (H-mode).

H-mode			
MEA1			
Data Product Name	**Description**	**Time Resolution (s)**	**Note**
3D-H	3D count data 88 direction × 32 energy	4	16 sectors, 8 channels
MEA2			
Data Product Name	**Description**	**Time Resolution (s)**	**Note**
3D-H	3D count data 88 direction × 32 energy × 2	2	16 sectors, 8 channels + 16 sectors, 8 channels

Table 6 Parameters used to describe the various calibration setups, procedures, and results.

E	Incident electron energy, eV
Θ	Elevation angle
Φ	Azimuth angle
Uan	Analyzer voltage
Utop	Top part of analyzer voltage
K	E=Uan $\cdot$ K
K0	Best K for the current Θ and Φ
ΔE/E	Energy resolution of the analyzer
P_{BEAM}	Electron beam flux $cm^{-2}s^{-1}$ as a function of the elevation angle
Ω_i	One azimuthal sector aperture, cm^2 for fixed Θ, Φ, Uan and Utop
Ci	Count rate, s^{-1} of one azimuthal sector
Gi	One sector G-factor, cm^2 sr eV/eV
G	Total G-factor of the instrument, cm^2 sr eV/eV
	(used for numerical simulation)
HV_{MCP}	MCP high voltage, V, measured at the HV unit level

Table 7 Summary of MEA1 (top) and MEA2 (bottom) calibration. GF corresponds to the geometrical factor of the instrument (cm^2 sr eV/eV), and GF0 corresponds to the GF when Utop = Uan. $\Delta\theta$ is the elevation FWHM. The remaining parameters are defined in Table 6.

MEA1				
Utop/Uan	0.8	0.42	0.34	0.27
GF cm^2 sr eV/eV	4e-3	6.7e-3	2.0e-3	6.7e-5
GF0/GF	1	6	20	60
Θ deg	1.8	7.0	8.2	9.0
$\Delta\Theta$ deg	5.9	4.5	3.0	3.6
K	8.67	8.48	8.57	8.51
ΔE/E	0.11	0.16	0.11	0.09

MEA2				
Utop/Uan	0.8	0.52	0.37	0.28
GF cm^2 sr eV/eV	2e-4	6.7e-5	1.6e-5	4.0e-6
GF0/GF	20	60	250	1000
Θ deg	1.8	6.3	7.5	9.0
$\Delta\Theta$ deg	5.9	5.0	3.0	3.5
K	8.67	8.62	8.57	8.51
ΔE/E	0.11	0.13	0.11	0.08

Table 8 MIA operation mode.

Mode	Produced data	Raw data rate
Solar Wind Mode	Count data	Max. 245760 bps
(DATA MODE 1)	1) $(8 + 8^{*1}(22.5°)$polar sectors	Average 98304 bps
	+2 background counters)	
	$\times 8(22.5°)$equatorial sectors	
	$\times 32$ energy steps/spin	
	2) $(8 + 8^{*1}(22.5°)$polar sectors	16 bits/data
	+2 background counters)	
	$\times 8(11.25°)$equatorial sectors	
	$\times 32$ energy steps/spin	
	3) $(8 + 4^{*2}(22.5°)$polar sectors	
	+2 background counters)	
	$\times 16(5.625°)$equatorial sectors	
	$\times 32$ energy steps / spin	
	(excluding 90deg. $\times$90deg. solar wind sector)	
	4)16 polar sectors $\times$16 equatorial sectors	
	$\times 128$ energy steps/4spins	
	(90deg. $\times$90deg. solar wind sector)	
Magnetospheric Ion	count data	139264 bps
High Angular	$(16 + 16^{*3}$ polar sectors	
Resolution Mode	+2 background counters)	16 bits/data
(DATA MODE 2)	$\times 32$ equatorial sectors	
	$\times 32$ energy steps/spin	
Magnetospheric Ion	count data	36864 bps
Low Angular	$(8 + 8^{*1}$ polar sectors	
Resolution Mode	+2 background counters)	16 bits/data
(DATA MODE 3)	$\times 16$ equatorial sectors	
	$\times 32$ energy steps/spin	

[*1]Sensitivity of about 120° in the eight polar sectors is reduced down to 1/50 with mechanical attenuation grid.

[*2]Sensitivity of about 30° in the four polar sectors is reduced down to 1/50 with mechanical attenuation grid.

[*3]Sensitivity of about 120° in the 16 polar sectors is reduced down to 1/50 with mechanical attenuation grid.

Table 9 MIA energy sweep.

Mode	Measurement	Sensitivity control	Spin/cycle	Energy range
0	Solar wind	OFF	4 (128 steps)	107 eV/q – 10.3 keV/q
1	Solar wind	ON	4 (128 steps)	123 eV/q – 11.6 keV/q
2	Solar wind	OFF	2 (64 steps) 2 (64 steps)	28.0 eV/q – 300 eV/q (32 steps) 3.10 keV/q – 25.8 keV/q (32steps)
3	Magnetosphere	OFF	1 (32 steps)	24.0 eV/q – 25.8 keV/q
4	Magnetosphere	OFF	1 (32 steps)	21.0 eV/q – 5.15 keV/q
5	Magnetosphere	OFF	1 (32 steps)	5.17 keV/q – 25.8 keV/q

Table 10 Examples of energy sweep – sector allocation of MIA.

Sector group	0	1	2	3	4	5	6	7
Sector	0-7	8-15	16-23	24-31	32-39	40-47	48-55	56-63
No. Measurement	Waveform allocation[1] (Mode)							
1 Solar wind	0	1	1	0	0	1	1	0
2 Solar wind	0	1	1	0	0	2	2	0
3 Magnetosphere	3	3	3	3	3	3	3	3
4 Magnetosphere	4	4	4	4	4	4	4	4
5 Magnetosphere	5	5	5	5	5	5	5	5

[1] One spin is divided equally into 64 sectors. Half of the MIA with (without) the mechanical attenuation grid faces the solar wind direction in sectors 8-23 (40-55).

Table 11 MIA mission data products in the L-mode, M-mode, and H-mode mission packets. Format of each product is shown in Table 12.

	MIA operation mode		
	MIA Mode 1	MIA Mode 2	MIA Mode 3
L-mode	Et-M1 (32s), VM-M1 (4s, 16s) 3D-LL-M1 (3600s)	Et-M2 (4s), VM-M2 (4s) 3D-LL-M2 (3600s)	Et-M3 (4s), VM-M3 (4s) 3D-LL-M3 (600s)
M-mode	3D-L2-M1 (8s) (MPPE mode = 0-5)	3D-L2-M2 (8s)	3D-L2-M3 (4s) (MPPE mode = 0-5)
M-mode	SW-L2-M1 (4s) (MPPE mode = 6-8)	3D-L2-M2 (8s)	3D-L2-M3 (8s) (MPPE mode = 6-8)
H-mode	SW-L-M1 (4s), 3D-L2-M1 (4s)	3D-H-M2 (4s)	3D-H-M3 (4s)

Table 12 Format, size and rate of the MIA data products. For the 3D count data products, 89 directions (DIR) are selected from 8 spin sectors (SC) ×17 channel (CH) directions. Velocity moments (VM) consist of density (n), net flux (nV)(x, y, z), and pressure (P)(xx, yy, zz, xy, yz, xz). EN represents energy.

Products	Format (16bits)	Size/Rate
Et-M1 (32s)	8 bits ×128 (EN)	640 B/160 bps
	(Solar wind direction)	
	8 bits ×128 (EN) ×4	
	(4-divided Omni direction)	
Et-M2, 3 (4s)	8 bits ×16 (EN) ×4	64 B/128 bps
	(4-divided Omni direction)	
VM-M1 (4s)	16-bit float ×10 (VM) ×2	40 B/80 bps
	(Solar wind and Omni)	
VM-M2,3 (4s)	16-bit float ×10 (VM)	20 B/40 bps
3D-LL-M1 (3600s)	16-bit counter ×16×17×32 (SC, CH, EN)	17 kB/39 bps
3D-LL-M2 (3600s)	16-bit counter ×32×17×32 (SC, CH, EN)	35 kB/77 bps
3D-LL-M3 (600s)	16-bit counter ×16×9×32 (SC, CH, EN)	8 kB/110 bps
3D-L2-M1 (8s)	16-bit counter ×89×32 (DIR, EN)	6 kB/6 kbps
	(Omni)	
SW-L2-M1 (4s)	16-bit counter ×4×17×32 (SC, CH, EN)	4 kB/9 kbps
	(Solar wind)	
3D-L2-M2 (8s)	16-bit counter ×16×9×32 (SC, CH, EN)	9 kB/9 kbps
3D-L2-M3 (8s)	16-bit counter ×89×32 (DIR, EN)	6 kB/6 kbps
3D-L2-M3 (4s)	16-bit counter ×89×16 (DIR, EN)	3 kB/6 kbps
SW-L-M1 (4s)	16-bit counter ×16×17×32 (SC, CH, EN)	17 kB/35 kbps
3D-L2-M1 (4s)	16-bit counter ×89×32(DIR, EN)	6 kB/11 kbps
3D-H-M2 (4s)	16-bit counter ×32×17×32 (SC, CH, EN)	35 kB/70 kbps
3D-H-M3 (4s)	16-bit counter ×16×17×32 (SC, CH, EN)	17 kB/34 kbps

Table 13 Summary of MIA performance.

Field of view	$3.8° \times 90°$ (high G-factor, solar wind)
	$5.1° \times 90°$ (low G-factor, solar wind)
	$9.6° \times 270°$ (high G-factor, Mercury ion)
	$6.4° \times 270°$ (low G-factor, Mercury ion)
Angular resolution	$5.625° \times 5.625°$ (solar wind)
	$22.5° \times 22.5°$ (Mercury ion)
Energy range	15 eV/q - 29 keV/q
Energy resolution	$\Delta E/E \sim 8.3\%$(FWHM, high G-factor, solar wind)
	$\Delta E/E \sim 2.2\%$(FWHM, low G-factor, solar wind)
	$\Delta E/E \sim 12.7\%$(FWHM, high G-factor, Mercury ion)
	$\Delta E/E \sim 3.6\%$(FWHM, low G-factor, Mercury ion)
Time resolution	(32 energy steps) 4 s/3D distribution function
	(128 energy steps) 16 s/3D distribution function
Geometrical factor	
High G-factor mode	3.39×10^{-6} cm^2 sr eV/eV (solar wind)
(5.625°:SW 22.5°:MI)	4.64×10^{-4} cm^2 sr eV/eV (Mercury ion)
Low G-factor mode	2.81×10^{-7} cm^2 sr eV/eV (solar wind)
(5.625°:SW 22.5°:MI)	1.23×10^{-5} cm^2 sr eV/eV (Mercury ion)
Mass	1.57 kg
Power	2.96 W
Dimensions	180 mm $\times$ 254 mm $\times$ 146 mm
Data rate	0.11 kbits/s (L-mode)
	2.5 kbits/s (M-mode)
	17 kbits/s (H-mode)
	after factor 3 compression

Table 14 Summary of MSA performance.

Field of view	$5° \times 260°$
Angular resolution	$5° \times 11.25°$
Energy range	1 eV/q – 38 keV/q
Energy resolution	$\Delta E/E = 8\%$
k-factor	6.85
Mass range	1–60 amu
Mass resolution	$m/\Delta m > 40$ (< 13 keV/q)
	$m/\Delta m = 10$ (> 13 keV/q)
Time resolution	3D distribution function in 4 s
	(32 energy steps)
	3D distribution function in 8 s
	(64 energy steps)
Geometrical factor (21 windows)	7×10^{-3} cm^2 sr eV/eV (ST)
	5×10^{-4} cm^2 sr eV/eV (LEF)
Mass	4.46 kg
Power	9.1 W
Dimensions	325 mm $\times$ 287 mm $\times$ 232 mm
Data rate	0.15 kbits/s (L-mode)
	1.4 kbits/s (M-mode)
	25 kbits/s (H-mode)
	after factor 10 compression

Table 15 MSA normal operation mode. M#: count rate matrix of given ion species; A: anode (or entrance window); S: spin sector (32 in one spin); E: energy step (32 in one spin sector); V: velocity direction (36 view directions); T: time of flight.

Name	Content	Internal (32 bit) Dimension	kbit	External (16 bit) Dimension	kbit	Time resolution Int	Med
M0	Starts	32S×32E×21A	688	36V×64E	37	4 s	24 s
A0	Starts			21A×32S	11	64s	256 s
M1	Protons	32S×32E×21A	688	36V×64E	37	4 s	24 s
M2	He^{++}	32S×32E×21A	688	36V×64E	37	4 s	48 s
M3	HeavyIons	32S×32E×21A	688	36V×64E	37	4 s	48 s
M4	OtherIons	32S×64E×21A	1376	36V×64E	37	64 s	256 s
M5	OtherIons	32S×64E×21A	1376	36V×64E	37	64 s	256 s
M6	OtherIons	32S×64E×21A	1376	36V×64E	37	64 s	256 s
M7	OtherIons	32S×64E×21A	1376	36V×64E	37	64 s	256 s
M8	OtherIons	32S×64E×21A	1376	36V×64E	37	64 s	256 s
M9	OtherIons	32S×64E×21A	1376	36V×64E	37	64 s	256 s
M10	OtherIons	32S×64E×21A	1376	36V×64E	37	64 s	256 s
M11	OtherIons	32S×64E×21A	1376	36V×64E	37	64 s	256 s
M12	OtherIons	32S×64E×21A	1376	36V×64E	37	64 s	256 s
M13	OtherIons	32S×64E×21A	1376	36V×64E	37	64 s	256 s
M14	OtherIons	32S×64E×21A	1376	36V×64E	37	64 s	256 s
M15	OtherIons	32S×64E×21A	1376	36V×64E	37	64 s	256 s
TSTC	STC TOF	64E×1024T	2097	32E×1024T	524	64 s	256 s
TSTE	STE TOF	64E×1024T	2097	32E×1024T	524	64 s	256 s
TLEF	LEF TOF	64E×2048T	4194	8E×2048T	262	64 s	256 s
SUM			**27652**		**1913**		

Table 16 MSA high spatial resolution mode.

Name	Content	Internal (32 bit)		External (16 bit)		Time resolution	
		Dimension	kbit	Dimension	kbit	Int	Med
M0	Starts	32S×32E×21A	688	21A×32S×2E	21	4 s	16 s
M1	Protons	32S×32E×21A	688	21A×32S×4E	43	4 s	16 s
M2	He^{++}	32S×32E×21A	688	21A×32S×4E	43	4 s	48 s
M3	HeavyIons	32S×32E×21A	688	21A×32S×4E	43	4 s	48 s
M4	OtherIons	32S×64E×21A	1376	21A×32S×4E	43	64 s	256 s
M5	OtherIons	32S×64E×21A	1376	21A×32S×4E	43	64 s	256 s
M6	OtherIons	32S×64E×21A	1376	21A×32S×4E	43	64 s	256 s
M7	OtherIons	32S×64E×21A	1376	21A×32S×4E	43	64 s	256 s
M8	OtherIons	32S×64E×21A	1376	21A×32S×4E	43	64 s	256 s
M9	OtherIons	32S×64E×21A	1376	21A×32S×4E	43	64 s	256 s
M10	OtherIons	32S×64E×21A	1376	21A×32S×4E	43	64 s	256 s
M11	OtherIons	32S×64E×21A	1376	21A×32S×4E	43	64 s	256 s
M12	OtherIons	32S×64E×21A	1376	21A×32S×4E	43	64 s	256 s
M13	OtherIons	32S×64E×21A	1376	21A×32S×4E	43	64s	256 s
M14	OtherIons	32S×64E×21A	1376	21A×32S×4E	43	64 s	256 s
M15	OtherIons	32S×64E×21A	1376	21A×32S×4E	43	64 s	256 s
TSTC	STC TOF	64E×1024T	2097	32E×1024T	524	64 s	256 s
TSTE	STE TOF	64E×1024T	2097	32E×1024T	524	64 s	256 s
TLEF	LEF TOF	64E×2048T	4194	8E×2048T	262	64 s	256 s
SUM			**27652**		**1976**		

Table 17 MSA high time resolution mode.

Name	Content	Internal (32 bit)		External (16 bit)		Time resolution	
		Dimension	kbit	Dimension	kbit	Int	Med
M0	Starts	32S×32E×21A	688	36V×32E	18	4 s	8 s
A0	Starts			21A×32S	11	64 s	64 s
M1	Protons	32S×32E×21A	688	36V×32E	18	4 s	8 s
M2	He++	32S×32E×21A	688	36V×16E	9	4 s	12 s
M3	HeavyIons	32S×32E×21A	688	36V×16E	9	4 s	12 s
M4	OtherIons	32S×64E×21A	1376	36V×16E	9	64 s	64 s
M5	OtherIons	32S×64E×21A	1376	36V×16E	9	64 s	64 s
M6	OtherIons	32S×64E×21A	1376	36V×16E	9	64 s	64 s
M7	OtherIons	32S×64E×21A	1376	36V×16E	9	64 s	64 s
M8	OtherIons	32S×64E×21A	1376	36V×16E	9	64 s	64 s
M9	OtherIons	32S×64E×21A	1376	36V×16E	9	64 s	64 s
M10	OtherIons	32S×64E×21A	1376	36V×16E	9	64 s	64 s
M11	OtherIons	32S×64E×21A	1376	36V×16E	9	64 s	64 s
M12	OtherIons	32S×64E×21A	1376	36V×16E	9	64 s	64 s
M13	OtherIons	32S×64E×21A	1376	36V×16E	9	64 s	64 s
M14	OtherIons	32S×64E×21A	1376	36V×16E	9	64 s	64 s
M15	OtherIons	32S×64E×21A	1376	36V×16E	9	64 s	64 s
TSTC	STC TOF	64E×1024T	2097	4E×1024T	65	64 s	64 s
TSTE	STE TOF	64E×1024T	2097	4E×1024T	65	64 s	64 s
TLEF	LEF TOF	64E×2048T	4194	2E×2048T	65	64 s	64 s
SUM			**27652**		**368**		

Table 18 MSA data for the different Mio telemetry regimes.

Mode	Products	bits/spin	bits/64 s	Compressed /64 s(TBC)	/spin	/s
Low	P0L-P3L,SP	357	5712	5712		
	M1L-M3L	192	3072	300 (L10)		
	TSTL	2048	32768	3300 (LL-10)		
	DataOut			**9312**	**582**	**145**
Med A	P0-P3, SP	645	10320	10320		
	P4-P15	60	960	960		
	M0,M1	12288	196608	19700 (L10)		
	A0	184	2944	290 (L10)		
	M2,M3	6144	98304	9800 (L10)		
	M4-M15	7135	114160	11400 (L10)		
	TSTC		131072	13100 (LL-10)		
	TSTE		131072	13100 (LL-10)		
	TLEF		65536	6500 (LL-10)		
	DataOut			**85190**	**5324**	**1331**
Med C	P0-P3, SP	645	10320	10320		
	P4-P15	60	960	960		
	M0,M1	17664	282624	28300 (L10)		
	M2,M3	8832	141312	14100 (L10)		
	M4-M15	8832	141312	14100 (L10)		
	TSTC		131072	13100 (LL-10)		
	TSTE		131072	13100 (LL-10)		
	TLEF		65536	6500 (LL-10)		
	DataOut			**100480**	**6280**	**1570**
Med D	P0-P3, SP	645	10320	10320		
	P4-P15	60	960	960		
	M0,M1	18432	294912	29500 (L10)		
	A0	736	11776	1200 (L10)		
	M2,M3	6144	98304	9800 (L10)		
	M4-M15	7135	114160	11400 (L10)		
	TSTC		131072	13100 (LL-10)		
	TSTE		131072	13100 (LL-10)		
	TLEF		65536	6500 (LL-10)		
	DataOut			**96280**	**6017**	**1504**
Med E	P0-P3, SP	645	10320	10320		
	P4-P15	60	960	960		
	M0,M1	14592	233472	23500 (L10)		
	M2,M3	6144	98304	9800 (L10)		
	TLEF		69905	3500 (L20)		
	Events	2618	41900	41900		
	DataOut			**86480**	**5405**	**1351**
High B	P0-P3, SP	645	10320	10320		
	P4-P15	60	960	960		
	M0,M1	29184	466944	46700 (L10)		
	M2,M3	18432	294912	29500 (L10)		
	M4-M15		442370	44200 (L10)		
	TSTC		1048576	52500 (L20)		
	TSTE		1048576	52500 (L20)		
	TLEF		1048576	52500 (L20)		
	Events	26187	419000	419000		
	DataOut			**708180**	**44261**	**11065**

Table 19 Selected parameters of MSA LEF spectra. The mass resolution is derived from $Tm/\Delta T$ where Tm is the median value and ΔT is the TOF spectra FWHM.

	He^+			
TOF voltage	Energy	Tm (ns)	ΔT (ns)	$Tm/\Delta T$
±8 kV	1–2 keV	398.1	27.1	14.7
	4–6 keV	394.9	33.4	11.8
±11 kV	1–2 keV	336.3	5.5	61.4
	4–6 keV	335.2	27.2	12.3

	Na^+			
TOF voltage	Energy	Tm (ns)	ΔT (ns)	$Tm/\Delta T$
±8 kV	1–2 keV	957.6	5.8	166.0
	4–6 keV	955.4	4.3	222.4
±11 kV	1–2 keV	810.7	6.8	118.7
	4–6 keV	809.7	4.7	172.7

	K^+			
TOF voltage	Energy	Tm (ns)	ΔT (ns)	$Tm/\Delta T$
±8 kV	1–2 keV	1249.4	11.1	112.5
	4–6 keV	1247.2	11.2	111.1
±11 kV	1–2 keV	1057.5	7.2	146.5
	4–6 keV	1055.5	9.3	113.3

Table 20 Sam as Table 19 but for central ST and total ST.

		He$^+$			
TOF voltage	ST	Energy	Tm (ns)	ΔT (ns)	Tm/ΔT
$\pm$8 kV	central	4 keV	193.7	8.6	22.4
		10 keV	154.9	7.8	19.8
	total	4 keV	195.5	14.1	13.9
		10 keV	158.2	12.8	12.3
$\pm$11 kV	central	4 keV	171.3	7.6	22.5
		10 keV	142.5	7.4	19.4
	total	4 keV	173.2	12.4	14.0
		10 keV	144.6	9.6	15.0

		K$^+$			
TOF voltage	ST	Energy	Tm (ns)	ΔT (ns)	Tm/ΔT
$\pm$8 kV	central	4 keV	662.5	322.7	2.1
		10 keV	581.3	342.2	1.7
	total	4 keV	681.8	261.4	2.4
		10 keV	609.5	268.2	2.3
$\pm$11 kV	central	4 keV	620.4	173.0	3.6
		10 keV	525.0	116.1	4.5
	total	4 keV	644.7	236.7	2.7
		10 keV	556.5	251.1	2.2

Table 21 Summary of HEP-ele performance.

Field of view	$(18° \times 57°) \times 2$
Angular resolution	$18° \times 12°$
Energy range	30 - 700 keV
Energy resolution	20 keV ($\leq 20°$C)
	$\Delta E/E = 50\%$
Time resolution	4 s (1spin) (normal mode)
	100 ms (burst mode)
Geometrical factor	0.036 cm^2 sr
Mass	0.27 kg
Power	3.04 W
Dimensions	82 mm $\times$ 134 mm $\times$ 115 mm
Data rate	0.0064 kbits/s (L-mode)
	1.3 kbits/s (M-mode)
	5.1 kbits/s (H-mode)

Table 22 Summary of HEP-ion performance.

Field of view	$11° \times 110°$
Angular resolution	$11° \times 20°$
Energy range	30 - 1500 keV
Energy resolution	20 keV ($\leq 20°$C)
	$\Delta E/E = 50\%$
Time resolution	4 s (1spin) (normal mode)
	100 ms (burst mode)
Geometrical factor	0.36 cm^2 sr
Mass	1.71 kg
Power	4.81 W
Dimensions	212 mm $\times$ 169.2 mm $\times$ 180 mm
Data rate	0.0085 kbits/s (energy), 0.0064 kbits/s (TOF) (L-mode)
	0.77 kbits/s (energy), 0.19 kbits/s (TOF) (M-mode)

Table 23 Observation Mode of HEP-ele

L-mode	Polar FOV(57°):2 $\times$ Sector(90°):4	48 bytes/15 spin
	$\times$ Energy Step:3	48 bytes/15 spin
M-mode	Polar FOV(11°):10 $\times$ Sector(45°):8	640 bytes/1 spin
	$\times$ Energy Step:4	640 bytes/1 spin
H-mode	Polar FOV(11°):10 $\times$ Sector(22.5°):16	5120 bytes/1 spin
	$\times$ Energy Step(95 keV):8	5120 bytes/1 spin

Table 24 Observation Mode of HEP-ion

	Energy Analysis Mode	
L-mode	Polar FOV(60°):2 × Sector(90°):4	64 bytes/15 spin
	× Energy step(440 keV):4	64 bytes/15 spin
M-mode	Polar FOV(20°):6 × Sector(45°):8	384 bytes/1 spin
	× Energy step(220 keV):8	384 bytes/1 spin
	TOF Analysis Mode	
L-mode	Polar FOV(60°):2 × Sector(90°):4	48 bytes/15 spin
	× TOF(300 ns):3 bin	48 bytes/15 spin
M-Mode	Polar FOV(20°):2 × Sector(45°):4	96 bytes/1 spin
	× TOF(150 ns):6 bin	96 bytes/1 spin

Table 25 Summary of ENA performances.

Field of view	15° × 160°
Angular resolution	9° x 25° (FWHM)
Energy range	10 eV − 3.3 keV
Energy resolution	0.5 (ΔE/E)
Mass resolution	H, O and heavy particles
Geometric factor	10^{-2} cm^2 str eV/eV / sector
Total efficiency	$\sim$0.01
Mass	2.13 kg
Power	4.42 W (secondary side)
Dimensions	258 mm × 127 mm × 223 mm (w/o thermal shield)
Data rate	0.5 kBytes/s (nominal)
	after factor 4 compression

Table 26 Format of coincidence mode packet of ENA.

TI		48 bit
packetID		8 bit (0x00)
slotID		8 bit
TOTAL COINCIDENCE COUNT	Incremented when signals from START SECTOR, START RING, and STOP SECTOR are detected and TOF is calculated.	16 bit
TOTAL START COUNT		16 bit
TOTAL STOP COUNT		16 bit
COINCIDENCE START SECTOR COUNT	Incremented when signals from START SECTOR, START RING, and STOP SECTOR are detected and TOF is calculated.	112 bit = 7 ch x 16 bit
COINCIDENCE STOP SECTOR COUNT	Incremented when signals from START SECTOR, START RING, and STOP SECTOR are detected and TOF is calculated.	128 bit = 8 ch x 16 bit
TOF event data		N x 20 bit
Remainder		Filled with zero
TOTAL (= (1/128) * Ts)		3072 bit

TI: Time indicator

slotID: Incremented every energy step (= (1/128)*Ts). Cleared by spin pulse

*1 This table shows a format for 1 energy step.

*2 MDP1 will read the data every 8 energy steps.

Table 27 TOF event data.

START RING	3 bit	0: ring1, 1: ring2, 2: ring3, 3: ring4 7: none
START SECTOR	3 bit	0: sect1, 1: sect2, 2: sect3, 3: sect4 4: sect5, 5: sect6, 6: sect7 7: none
STOP SECTOR	1 bit	1: Difference detected in stop pulse numbers deduced from TDC output and FPGA count. 0: No difference detected (normal)
	3 bit	0: sect1, 1: sect2, 2: sect3, 3: sect4 4: sect5, 5: sect6, 6: sect7, 7: sect8
TOF	10 bit	0x000: This value is not generated (*). 0x001-0x3ef: TOF 0x3f0-0x3fc: spare 0x3fd: No signal on START SECTOR 0x3fe: No signal on STOP SECTOR 0x3ff: No signal on both START SECTOR and STOP SECTOR

*TOF = 0x000 is dealt with no data marker by MDP1.

If it appears, MDP1 will not process the data

appeared afterword in the packet.

Table 28 Format of counter mode packet of ENA.

TI		48 bit
packetID		8 bit (0x01)
slotID		8 bit
START RING and START SECTOR COUNT		448 bit = 4 ch x 7 ch x 16 bit
START RING COUNT		64 bit = 4 ch x 16 bit
START SECTOR COUNT		112 bit = 7 ch x 16 bit
STOP SECTOR COUNT		128 bit = 8 ch x 16 bit
COINCIDENCE START SECTOR COUNT	Incremented when signals from START SECTOR, START RING, and STOP SECTOR are detected and TOF is calculated.	112 bit = 7 ch x 16 bit
COINCIDENCE STOP SECTOR COUNT	Incremented when signals from START SECTOR, START RING, and STOP SECTOR are detected and TOF is calculated.	128 bit = 8 ch x 16 bit
TOF event data		N x 20 bit
Rest		Filled with zero
TOTAL (= (1/128) * Ts)		3072 bit

*1 Above table shows a format for 1 energy step.

*2 MDP1 will read the data every 8 energy steps.

Table 29 Possible combinations of the telemetry mode with the sensor mode of ENA.

Telemetry Mode	Sensor Mode
Mass Accumulation Mode	Coincidence Mode
TOF Accumulation mode	Coincidence Mode
Count Accumulation Mode	Counter Mode
Non-Process Mode	Any
Idle Mode	Any

Table 30 Calibrated energy bin centers for hydrogen and oxygen.

E-Index	Nominal center energy (eV)	Hydrogen (eV)	Oxygen (eV)
0	0	0	0
1	10	20	8
2	20	37	15
3	40	67	29
4	80	120	54
5	160	215	103
6	320	387	196
7	640	693	370
8	1280	1243	699
9	2560	2228	1321
10	56	89	39
11	112	159	74
12	224	286	141
13	448	513	267
14	896	920	504
15	1792	1650	953

Table 31 Calibrated angular response.

Start sector	0	1	2	3	4	5	6
$\theta_0(°)$	67.1	40.8	16.9	-3.0	-24.2	-46.3	-68.1
$\beta_0(°)$	-5.4	-5.8	-6.5	-5.3	-5.8	-5.6	-5.2
$\Delta\theta(°)$	32.8	28.9	25.8	27.0	21.8	21.5	22.9
$\Delta\beta(°)$	11.6	10.5	9.9	9.0	7.7	7.8	7.1

Table 32 Selected estimated geometric factors not including detection probability for neutral hydrogen. Values indicated with n/a are not yet available.

E-Index	Nominal center energy (eV)	G for hydrogen without detection probability (cm^2 sr eV/eV)
0	0	n/a
1	10	n/a
2	20	n/a
3	40	0.9×10^{-7}
4	80	1.2×10^{-7}
5	160	1.9×10^{-7}
6	320	2.5×10^{-7}
7	640	0.5×10^{-6}
8	1280	n/a
9	2560	n/a
10	56	1.0×10^{-7}
11	112	n/a
12	224	n/a
13	448	3.6×10^{-7}
14	896	n/a
15	1792	n/a

Table 33 MPPE data mode and L-mode data products of LEP and HEP sensors.

MPPE MODE NAME	L-mode data products
1. Default Observation Mode	MEA1: Et-OMN, Et-PAP, VM, 3D-LL
	MEA2: Et-OMN, Et-PAP, VM
	MIA: Et-M1, VM-M1, 3D-LL-M1
	MSA: Low [Moments, Omni E-t, TOF]
	HEP: L-mode
2. Exospheric Mode	MEA1: Et-OMN, Et-PAP, VM, 3D-LL
	MEA2: Et-OMN, Et-PAP, VM
	MIA: Et-M2, VM-M2, 3D-LL-M2
	MSA: Low [Moments, Omni E-t, TOF]
	HEP: L-mode
3. Solar Wind Mode/ IP Shock Local Mode	MEA1: Et-OMN, Et-PAP, VM, 3D-LL
	MEA2: Et-OMN, Et-PAP, VM
	MIA: Et-M1, VM-M1, 3D-LL-M1
	MSA: Low [Moments, Omni E-t, TOF]
	HEP: L-mode
4. IP Shock Macro Mode/ Bow Shock Mode	MEA1: Et-OMN, Et-PAP, VM, 3D-LL
	MEA2: Et-OMN, Et-PAP, VM
	MIA: Et-M1, VM-M1, 3D-LL-M1
	MSA: Low [Moments, Omni E-t, TOF]
	HEP: L-mode
5. Reconnection Mode	MEA1: Et-OMN, Et-PAP, VM, 3D-LL
	MEA2: Et-OMN, Et-PAP, VM
	MIA: Et-M3, VM-M3, 3D-LL-M3
	MSA: Low [Moments, Omni E-t, TOF]
	HEP: L-mode
6. Magnetospheric Mode	MEA1: Et-OMN, Et-PAP, VM, 3D-LL
	MEA2: Et-OMN, Et-PAP, VM
	MIA: Et-M3, VM-M3, 3D-LL-M3
	MSA: Low [Moments, Omni E-t, TOF]
	HEP: L-mode

Table 34 MPPE data mode and M-mode data products of LEP and HEP sensors.

MPPE MODE NAME	M-mode data products
1. Default Observation Mode	MEA1: Et-OMNm, Et-PAP, VM, 3D-M
	MEA2: Et-OMNm, Et-PAP, VM
	MIA: 3D-L2-M1 or SW-L2-M1
	MSA: Med A [Moment, 3D-VDF(A), AD(A), TOF(A)]
	HEP: M-mode
2. Exospheric Mode	MEA1: Et-OMNm, Et-PAP, VM, 3D-M
	MEA2: Et-OMNm, Et-PAP, VM
	MIA: 3D-L2-M2
	MSA: Med D [Moment, 3D-VDF(D), AD(D), TOF(D)]
	HEP: M-mode
3. Solar Wind Mode/ IP Shock Local Mode	MEA1: Et-OMNm, Et-PAP, VM, 3D-M
	MEA2: Et-OMNm, Et-PAP, VM
	MIA: 3D-L2-M1 or SW-L2-M1
	MSA: Med C [Moment, 3D-VDF(C), AD(C), TOF(C)]
	HEP: M-mode
4. IP Shock Macro Mode/ Bow Shock Mode	MEA1: Et-OMNm, Et-PAP, VM, 3D-M
	MEA2: Et-OMNm, Et-PAP, VM
	MIA: 3D-L2-M1 or SW-L2-M1
	MSA: Med C [Moment, 3D-VDF(C), AD(C), TOF(C)]
	HEP: M-mode
5. Reconnection Mode	MEA1: Et-OMNm, Et-PAP, VM, 3D-M
	MEA2: Et-OMNm, Et-PAP, VM
	MIA: 3D-L2-M3
	MSA: Med C [Moment, 3D-VDF(C), AD(C), TOF(C)]
	HEP: M-mode
6. Magnetospheric Mode	MEA1: Et-OMNm, Et-PAP, VM, 3D-M
	MEA2: Et-OMNm, Et-PAP, VM
	MIA: 3D-L2-M3
	MSA: Med D [Moment, 3D-VDF(D), AD(D), TOF(D)]
	HEP: M-mode

Table 35 MPPE data mode and H-mode data products of LEP and HEP sensors.

MPPE MODE NAME	H-mode data products
1. Default Observation Mode	N.A.
2. Exospheric Mode	MEA1: 3D-H
	MEA2: 3D-H
	MIA:3D-H-M2
	MSA: High B [Moment, 3D-VDF(B), TOF(B) , EVENT(B)]
	HEP: H-mode
3. Solar Wind Mode/ IP Shock Local Mode	MEA1: 3D-H
	MEA2: 3D-H
	MIA: SW-L-M1, 3D-L2-M1
	MSA: High B [Moment, 3D-VDF(B), TOF(B) , EVENT(B)]
	HEP: H-mode
4. IP Shock Macro Mode/ Bow Shock Mode	MEA1: 3D-H
	MEA2: 3D-H
	MIA: SW-L-M1, 3D-L2-M1
	MSA: High B [Moment, 3D-VDF(B), TOF(B) , EVENT(B)]
	HEP: H-mode
5. Reconnection Mode	MEA1: 3D-H
	MEA2: 3D-H
	MIA: 3D-H-M3
	MSA: High B [Moment, 3D-VDF(B), TOF(B) , EVENT(B)]
	HEP: H-mode
6. Magnetospheric Mode	MEA1: 3D-H
	MEA2: 3D-H
	MIA: 3D-H-M3
	MSA: High B [Moment, 3D-VDF(B), TOF(B) , EVENT(B)]
	HEP: H-mode
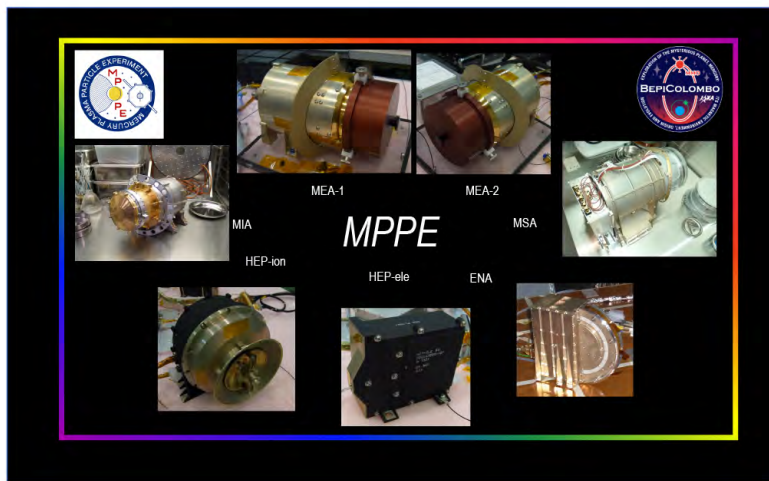
Fig. 1 Photo of the seven MPPE sensors.
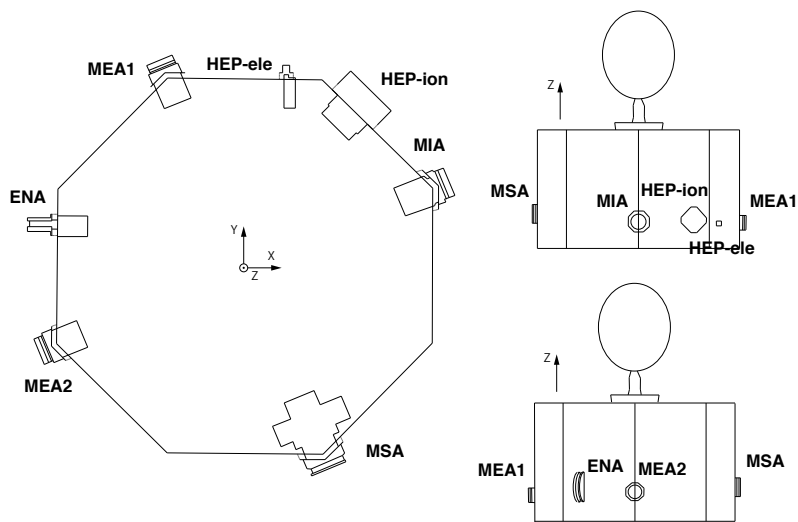
Fig. 2 Locations of the seven MPPE sensors.
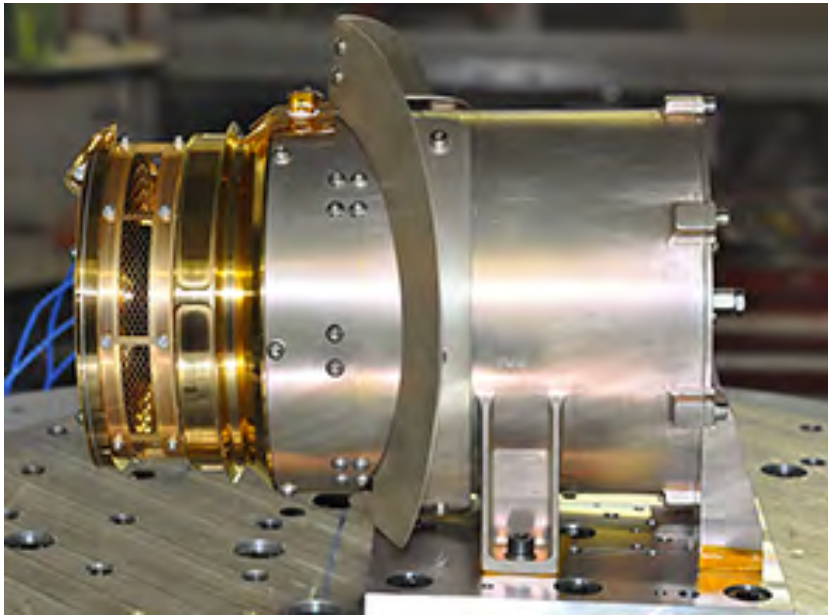
Fig. 3 View of the MEA2 sensor during vibration tests.
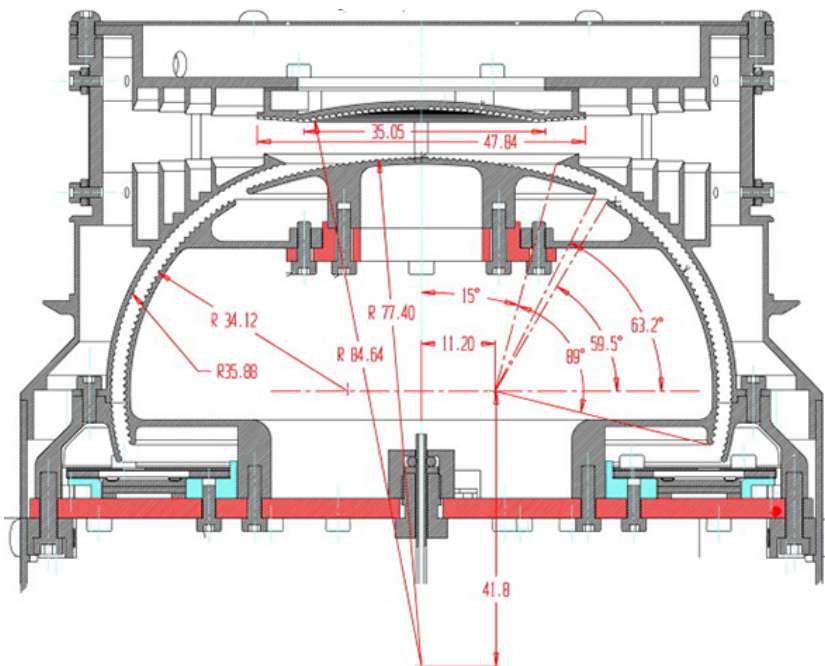
Fig. 4 Electron optic design of MEA.
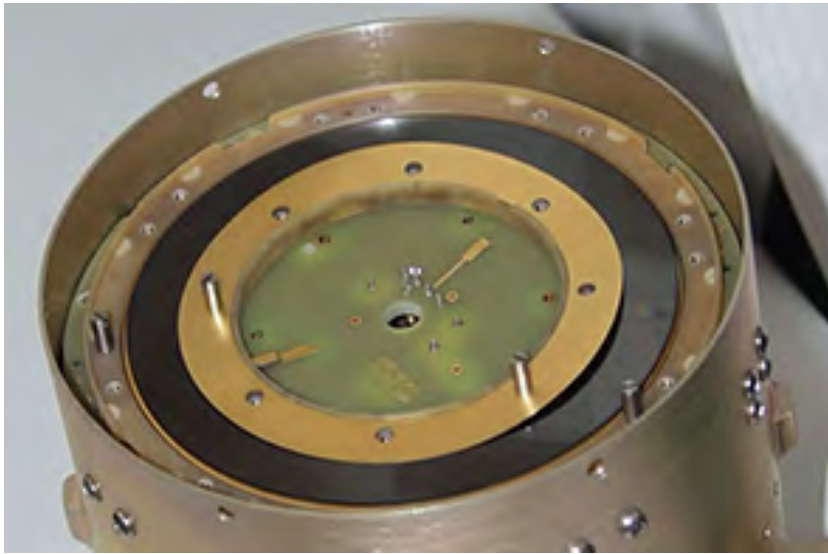
Fig. 5 View of the MCPs located inside the MEA2 sensor head.
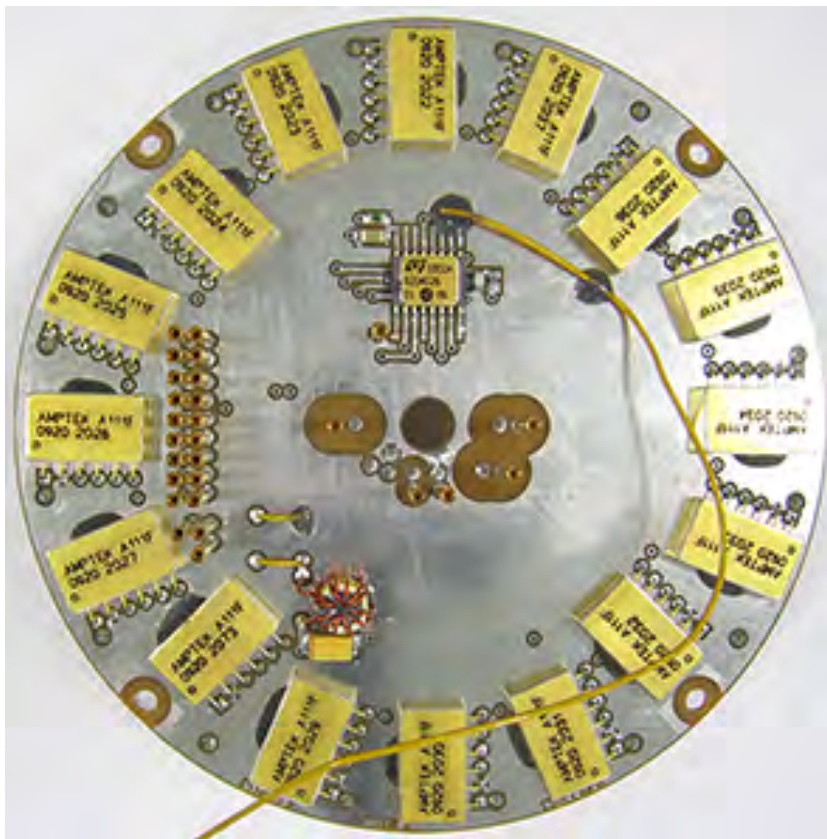
Fig. 6 Anode board of MEA2.
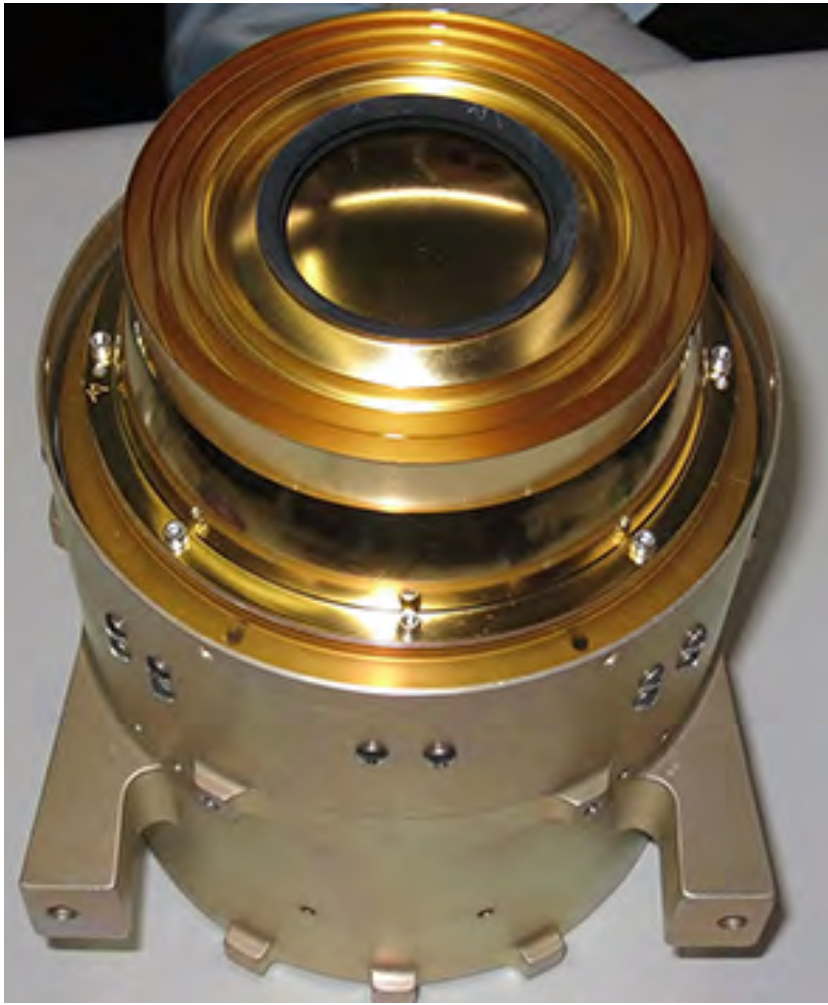
Fig. 7 View of the entrance of the electrostatic analyzer of MEA.
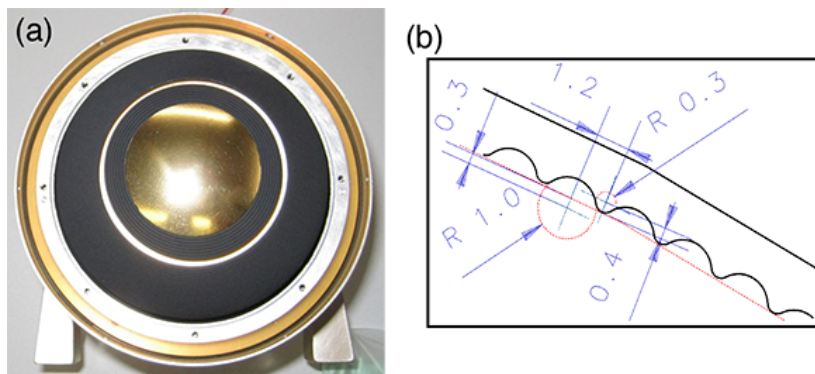
Fig. 8 (a) View of the toroidal inner sphere of MEA2. (b) Dimensions of the scalloping used.
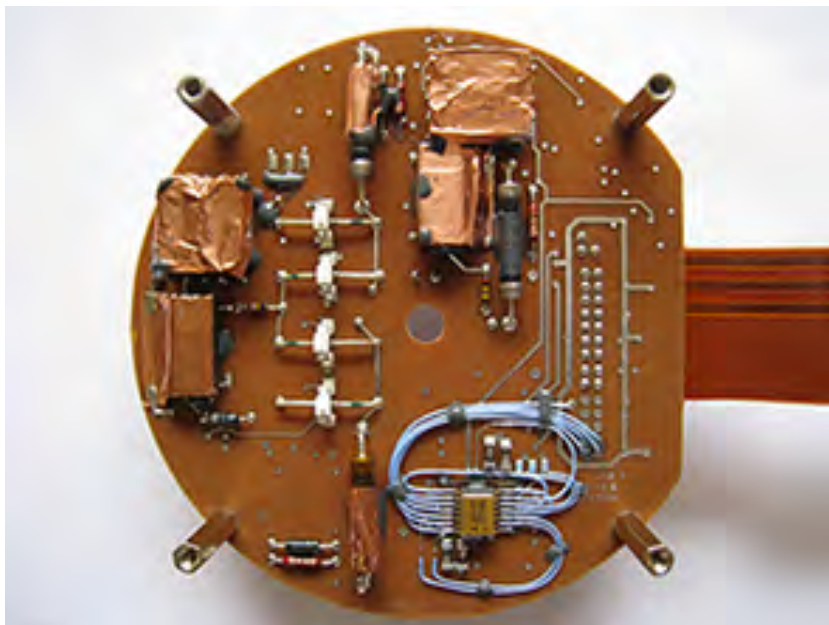
Fig. 9 High-voltage board of MEA2.
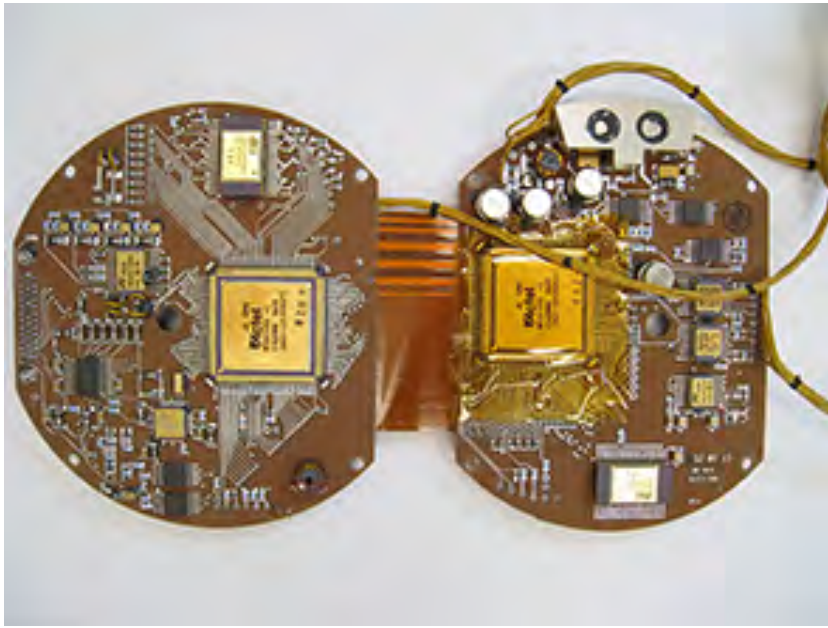
Fig. 10 FPGA board of MEA2.
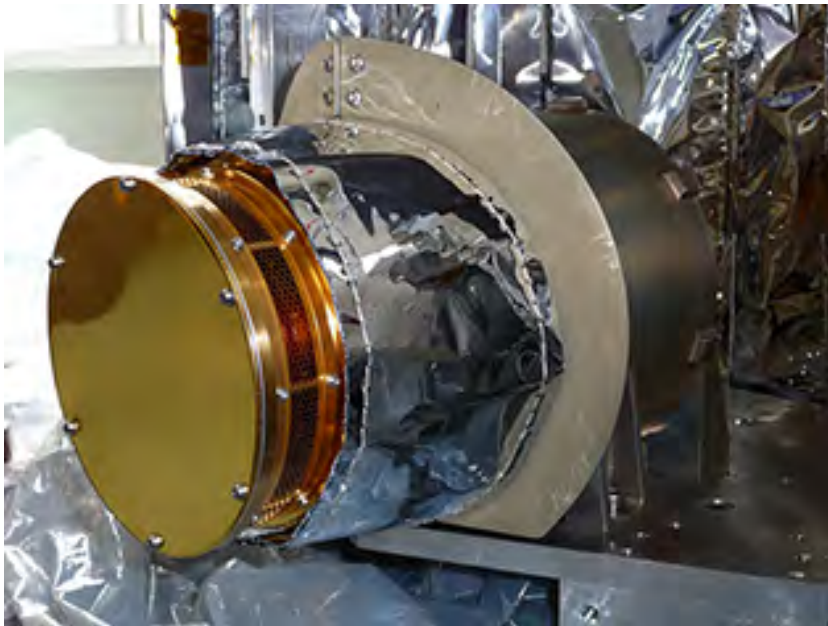
Fig. 11 MEA2 with its multi-layer insulator integrated with the Mio spacecraft.

Fig. 12 Thermal shield of MEA2.
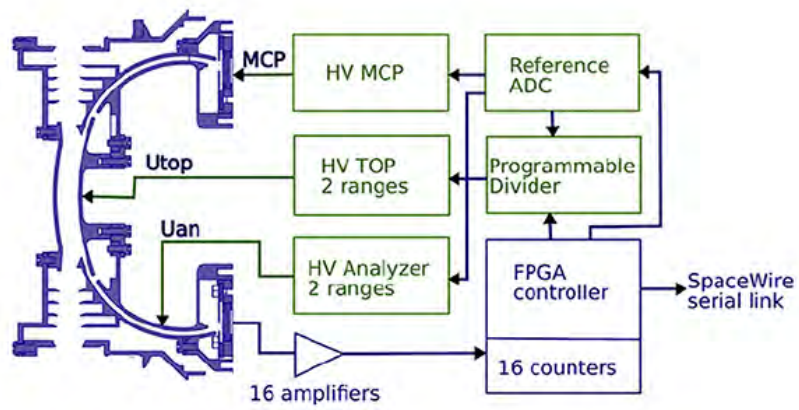
Fig. 13 Block diagram of MEA.
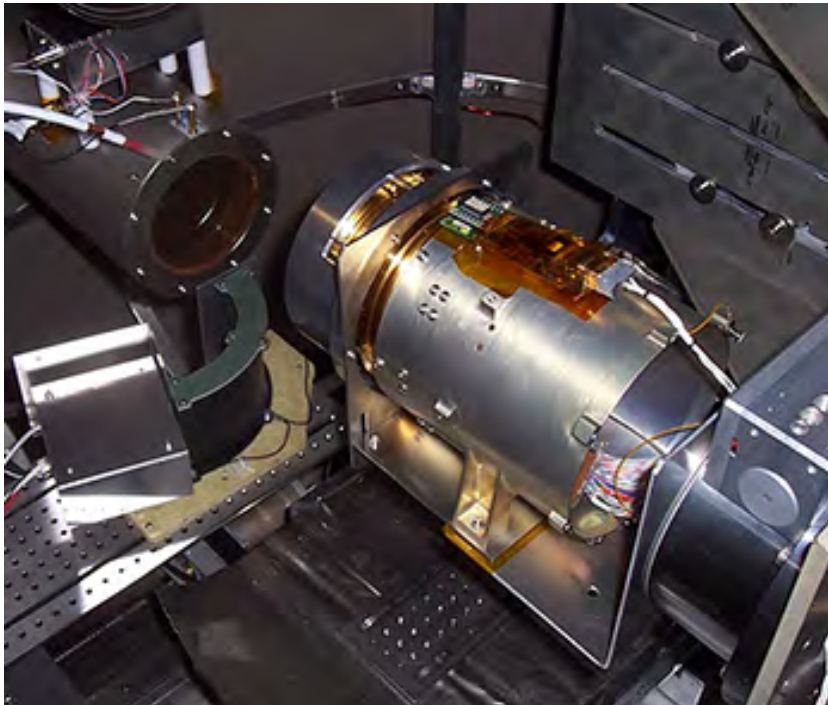
Fig. 14 MEA1 installed in the vacuum chamber. A magnetometer is glued to the sensor housing. The instrument is turned by 90° in elevation. The simulator for the thermal shield of the sensor is shown above the aperture of the sensor.
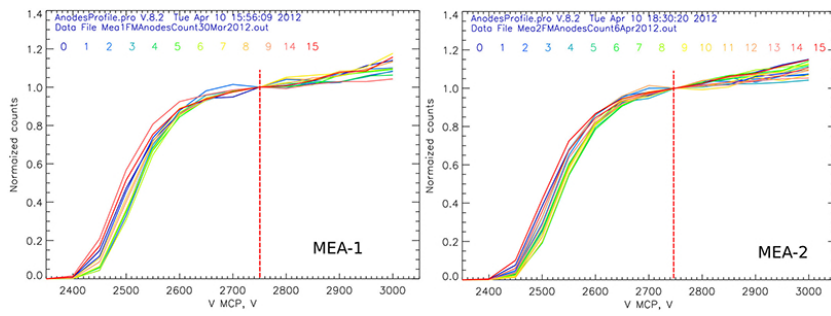
Fig. 15 MCP counts as a function of MCP bias voltage. Each of the 16 anodes is represented by a different color, with the anode number printed in the same color at the top of the plot.
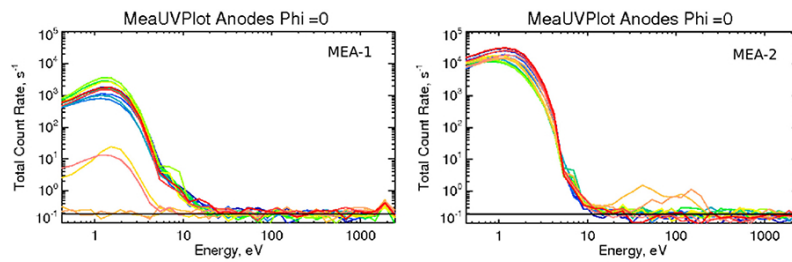
Fig. 16 UV contamination test results for MEA1 and MEA2. Each of the 16 anodes is represented by a different color as described in Figure 15.
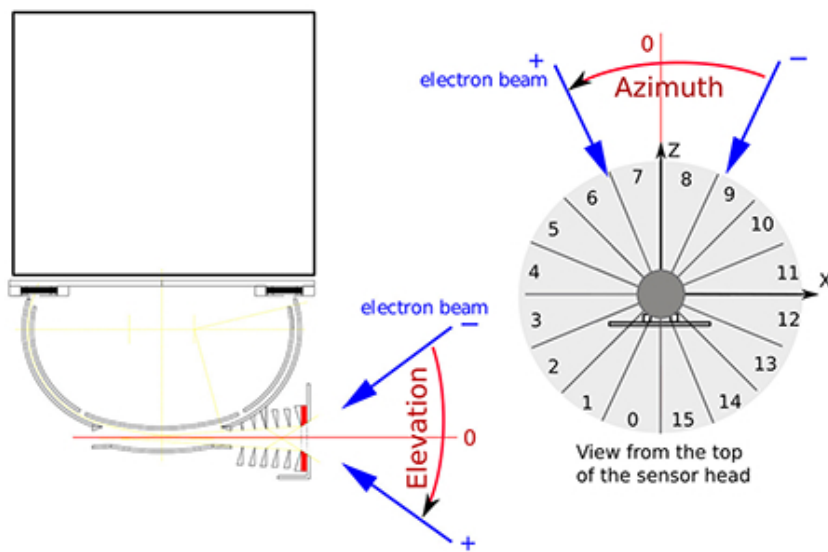
Fig. 17 Definition of the elevation and azimuth angles for full calibration of the MEA sensors.
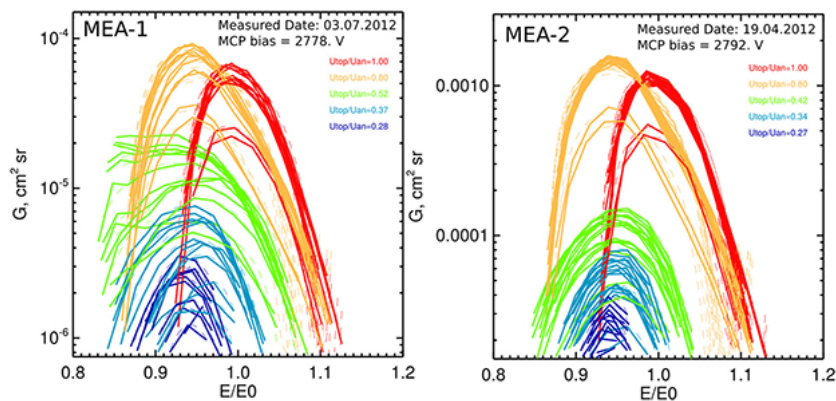
Fig. 18 Energy responses of different anodes for various G-factor levels. Each of the 16 anodes is represented for each G-factor level.
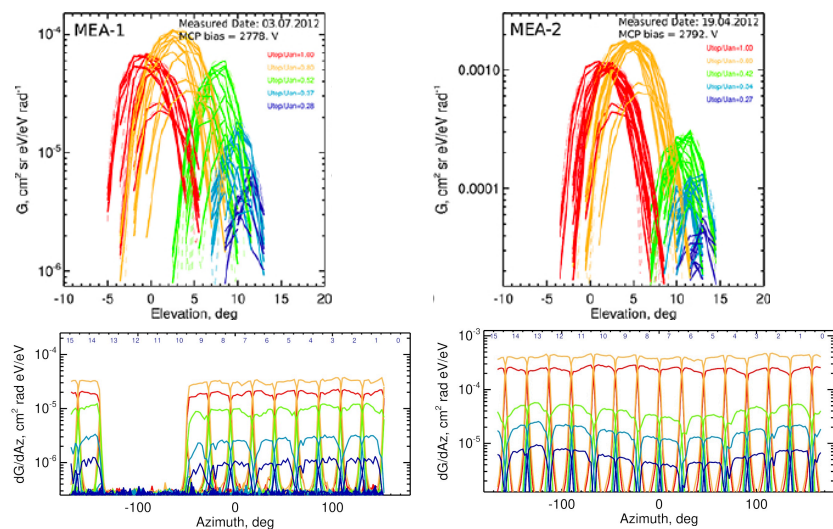
Fig. 19 Top: Elevation response of the 16 anodes for various G-factor levels (in color). Each of the 16 anodes is represented for each G-factor level. Bottom: azimuthal response of the 16 anodes for various G-factor levels (in color, same color code as used on the top panel)
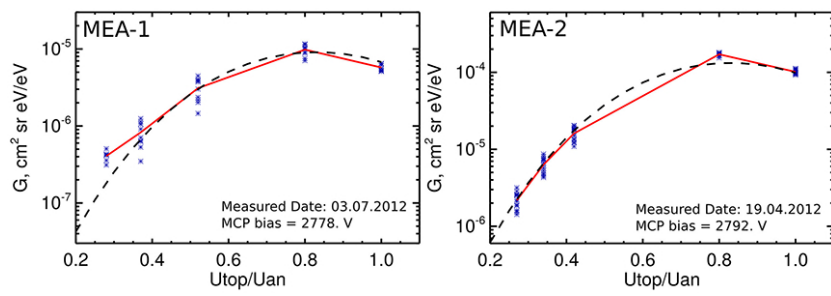
Fig. 20 Anodes G-factors as a functions of Utop/Uan. The dashed lines show the theoretical profile scaled with the appropriate factor.
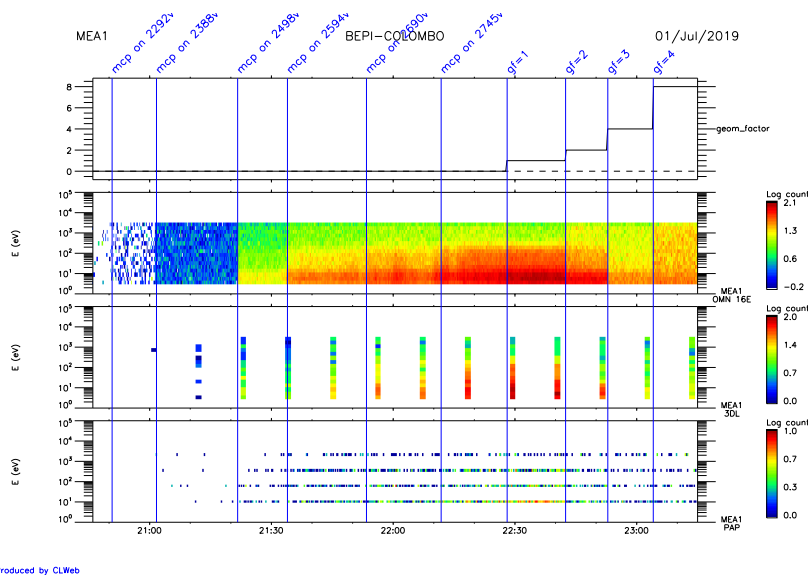
Fig. 21 First MEA1 data obtained in the solar wind on July 1, 2019. The first panel is the GF of the sensor that was varied by decreasing the ratio Utop/Uan from 1 to its lowest value at the end of the interval (for corresponding values of the GF see Figure 20 from right to left). The vertical lines delineate the commands sent to MEA1 during the time period, particularly when the HV was raised to nominal values of 2750 V. The three following panels indicate the energy-time spectrogram of Et-OMN data (in counts), 3D data, and pitch-angle distributions for four selected energies, in L-mode.
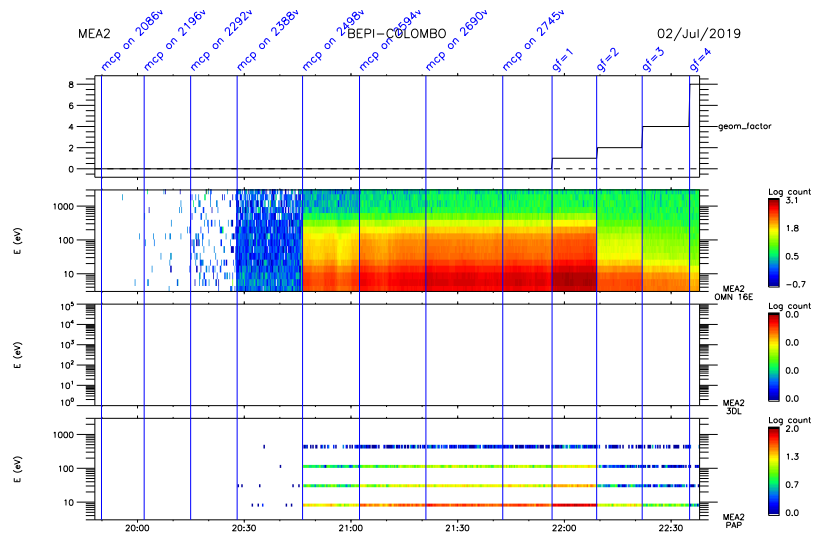
Fig. 22 First MEA2 data obtained in the solar wind on July 2, 2019. The description is presented in Figure 21.
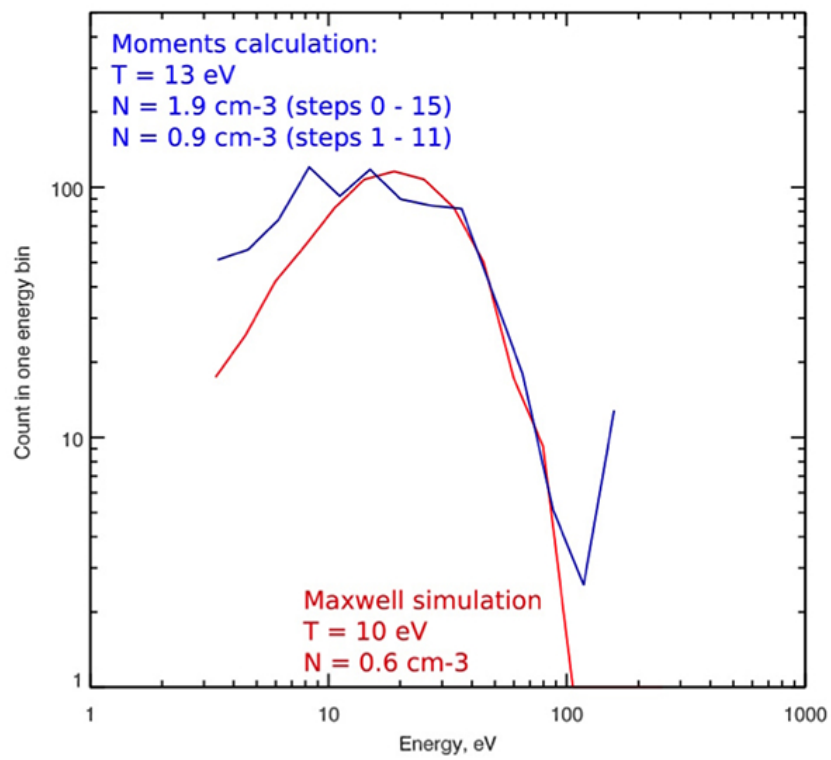
Fig. 23 MEA1 moment (density, temperature) estimated from 3D data (blue) and compared with a Maxwellian distribution function (red), after noise removal. The spike observed above 100 eV corresponds to part of the halo solar wind electron distribution function.

Fig. 24 MIA flight model delivered to the Mio system in June 2014.
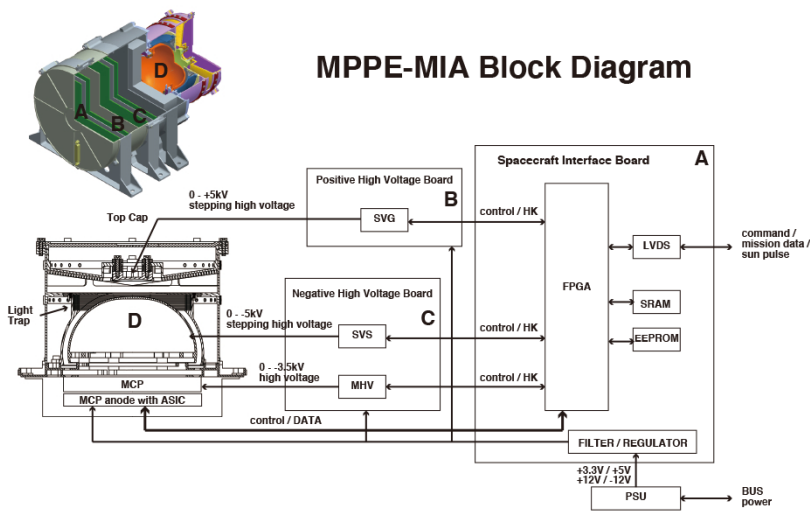
Fig. 25 MIA block diagram.
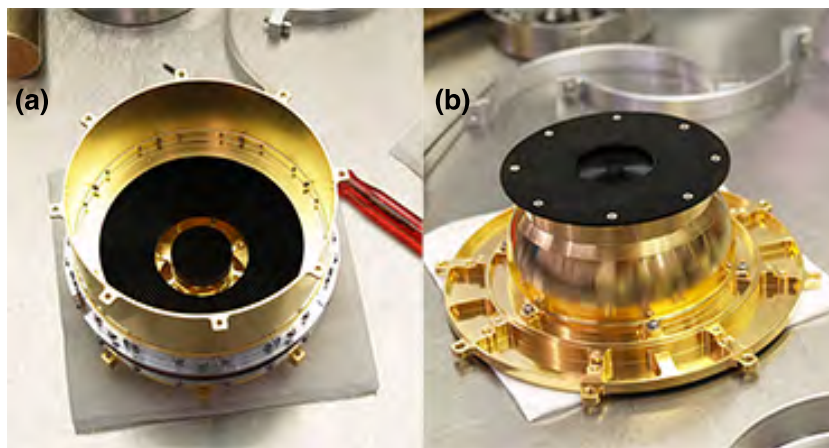
Fig. 26 (a)"Top-cap" and upper part of the entrance collimator of MIA. (b)Inner sphere and bottom part of the entrance collimator of MIA. The parts are gold plated or blackened by copper sulfide black.
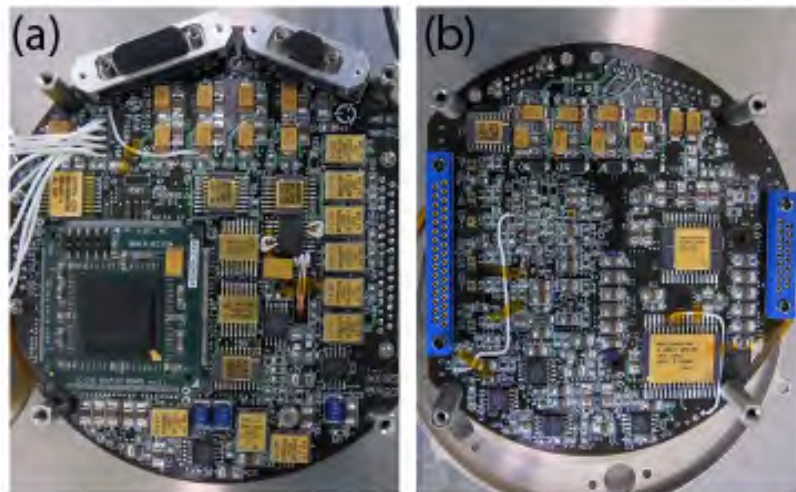
Fig. 27 Digital interface board of MIA. (a) Rear side, (b) front side.
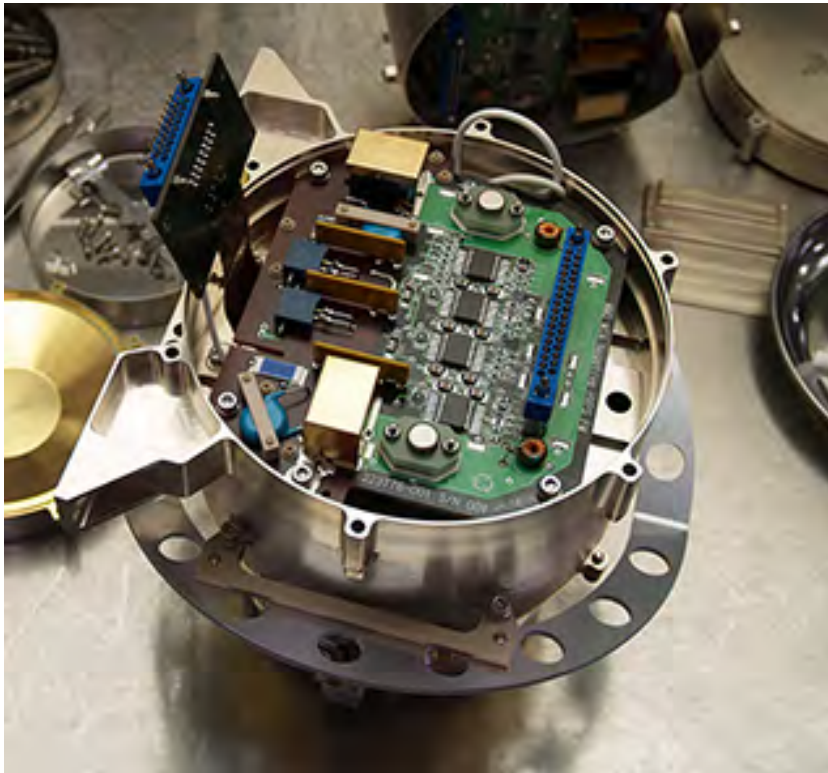
Fig. 28 Negative high voltage board installed in the chassis of MIA. A Hypertac connector

from ASIC on the MCP anode is also shown.

(a) SPIN AXIS

sectors with attenuation grid

+-60deg.

~ecliptic plane

(b) 120deg.

mechanical attenuation grid

(c) 1mm

0.4mm

0.1mm

120.0deg.
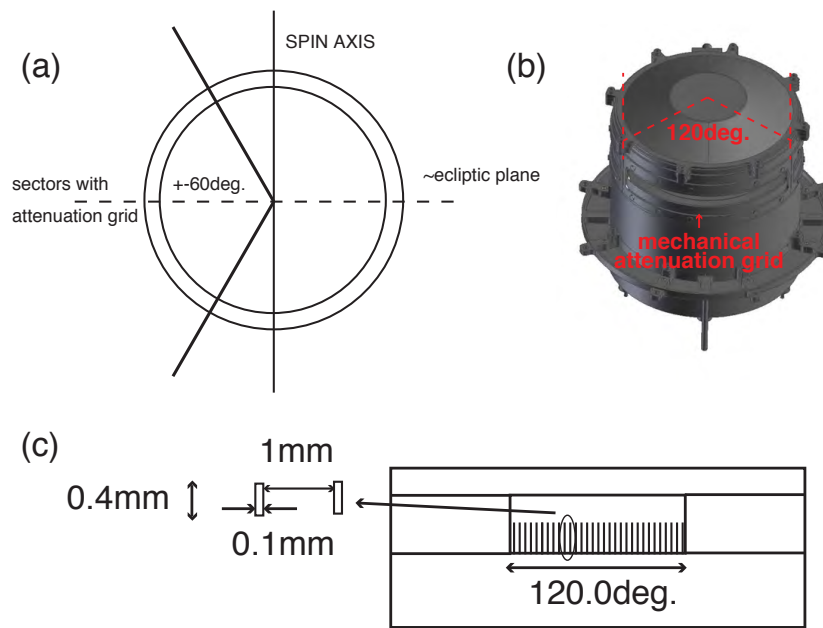
Fig. 29 Attenuation grid of MIA. (a)The relationship between the spin axis and the entrance of MIA with the mechanical attenuation grid.(b)Ion entrance of MIA with the mechanical attenuatin grid. (c) Pattern of attenuation grid.
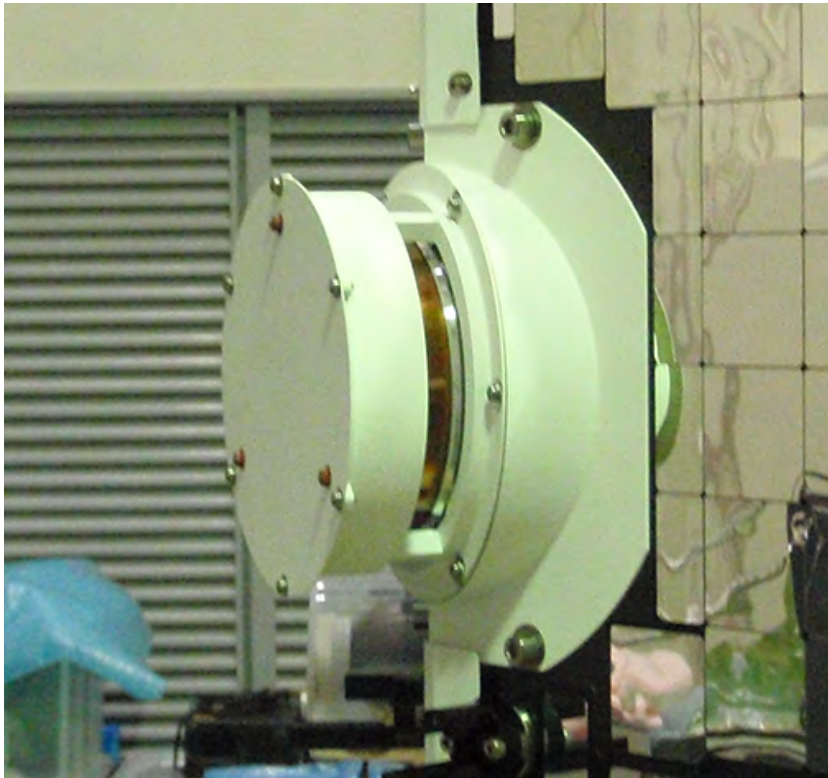
Fig. 30 MIA with thermal shield installed on one of the eight corners of the Mio spacecraft.The entrance aperture is covered by a Kapton sheet that was removed before the launch.
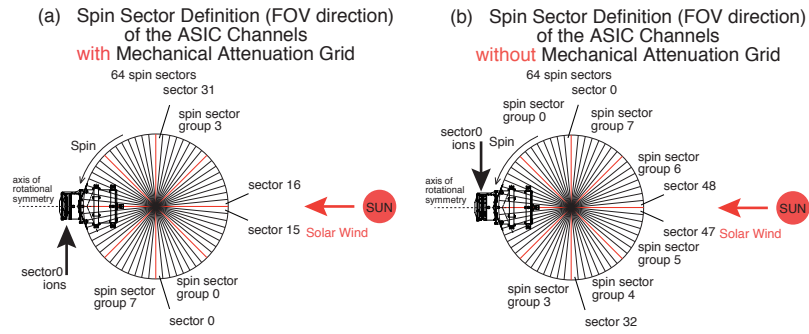
Fig. 31 Definition of the spin sector 0. Spin Sector 0 is defined when the axis of the rotational symmetry of MIA (dashed line) is pointing away from the Sun. The ion flow direction observed at Spin Sector 0 is indicated by a black arrow and the solar wind ion flow direction is indicated by a red arrow. (a) The solar wind channel with mechanical attenuation grid observes solar wind at spin sector group 1 (from spin sector 8 to 15) and spin sector group 2 (from spin sector 16 to spin sector 23). (b) The other channels without the mechanical attenuation grid observe solar wind at spin sector group 5 (from spin sector 40 to 47) and spin sector group 6 (from spin sector 48 to spin sector 55).
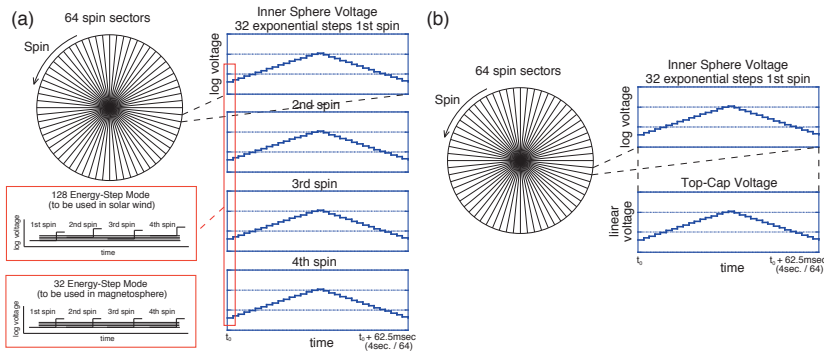
Fig. 32 Energy sweep waveform of MIA.(a) When observing solar wind ions, 128 energy steps are swept by using 4 different 32 energy steps during 4 consecutive spins. (b) When electrical attenuation is enabled, the same volatages are applied to the inner sphere and the top-cap part.
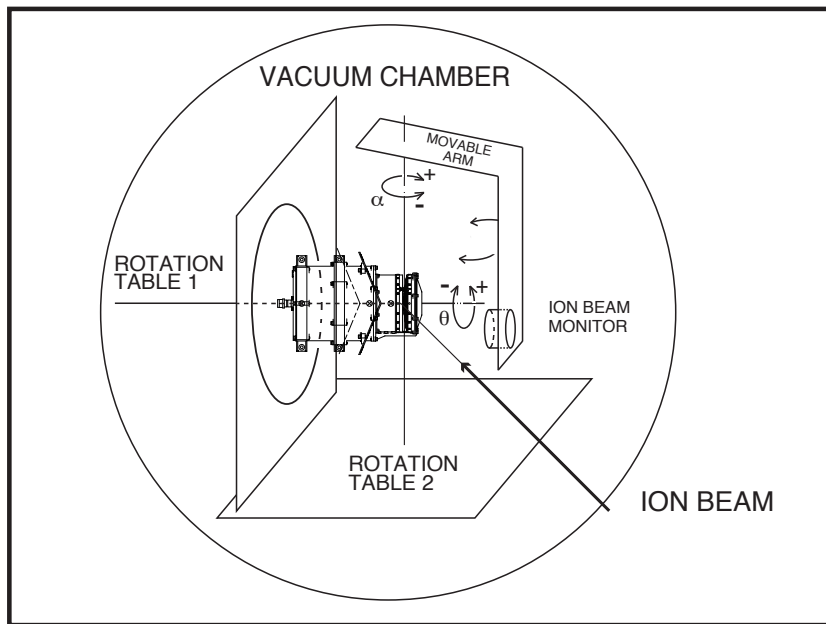
Fig. 33 Schematic diagram showing the configuration of MIA calibration. Rotation Table 1 is installed on Rotation Table 2. The ion entrance angles α and θ with the definitions of their positive and negative directions are shown.
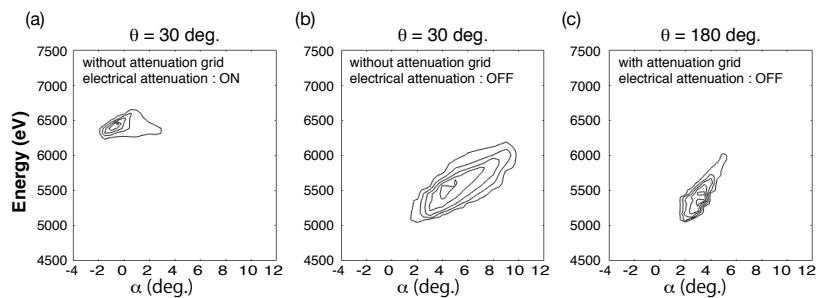
Fig. 34 Examples of E-α contour. An ion beam with a sufficiently large area was injected at $\theta{=}30°$ for panels (a) and (b) and $\theta{=}180°$ for panel (c). The counts are normalized by the maximum count in each E-α contour; five contour lines with levels of 0.1, 0.3, 0.5, 0.7 and 0.9 are shown. (a) Without the mechanical attenuation grid; the electrical attenuation is ON. (b) Without the mechanical attenuation grid; the electrical attenuation is OFF. (c) With the mechanical attenuation grid; the electrical attenuation is OFF.
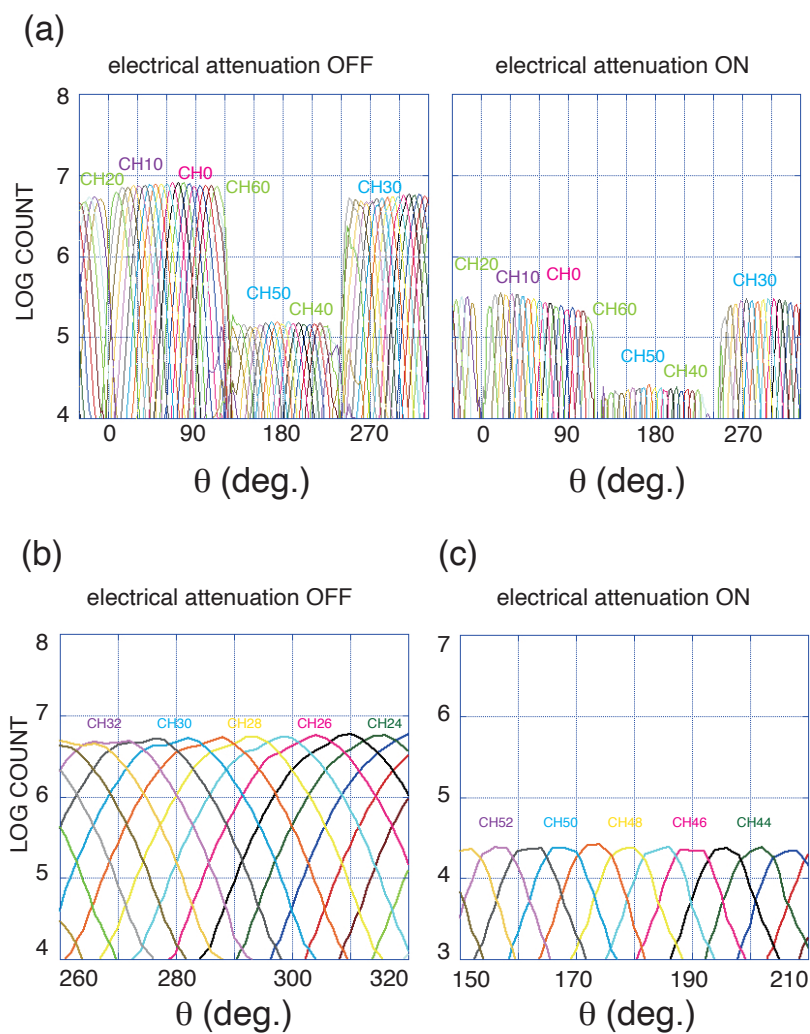
Fig. 35 θ (azimuthal angle) resolution of MIA. (a)The θ angle coverage of each anode channel is shown (left panel: electrical attenunation OFF; right panel: electrical attenuation ON). (b)The θ angle coverage of anode channels CH23 – CH34 without the mechanical attenuation grid and the electrical attenuation is OFF. (c)The θ angle coverage of anode channels CH42 – CH53 with the mechanical attenuation grid and the electrical attenuation is ON.
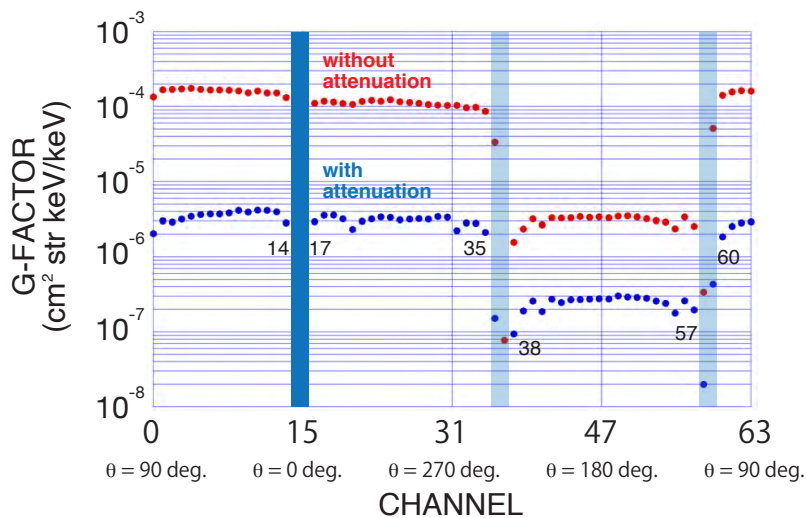
Fig. 36 Geometrical factor of MIA. Red dots show G-factor without electrical attenuation. Blue dots show G-factor with electrical attenuation (energy sweep mode 1). The light and thick blue boxes indicate the channels affected by the physical supports across the entrance aperture. Channel 15 is connected to an annular anode where no ions from the analyzer are expected to enter for monitoring the background count (Saito et al., 2017). Channel 16, which is not connected to an anode is used to monitor the electrical background noise. The relationship between the ion entrance angle θ (Figure 33) and the corresponding ASIC channel is also shown.
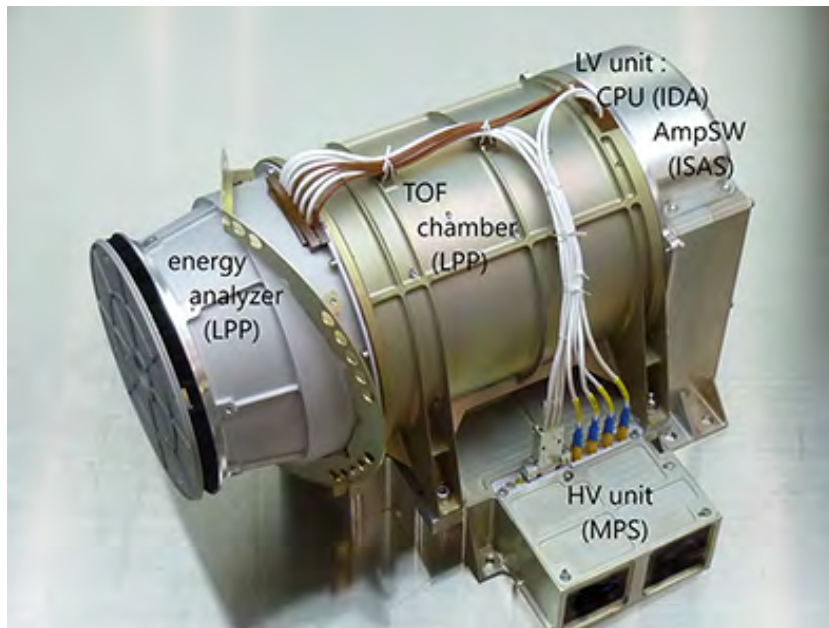
Fig. 37 MSA flight model delivered to Mio system in June 2014.
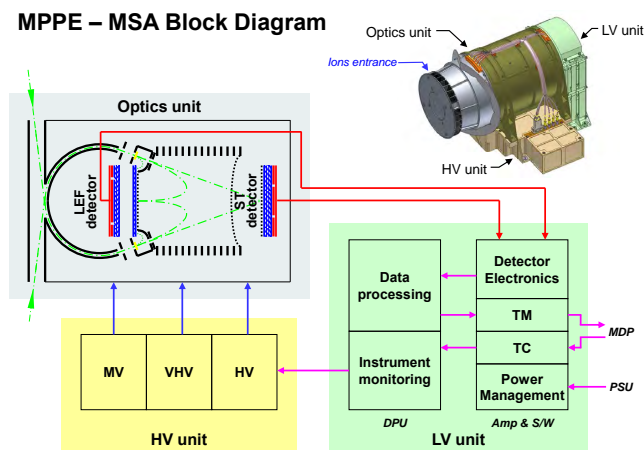
Fig. 38 Block diagram of MSA.
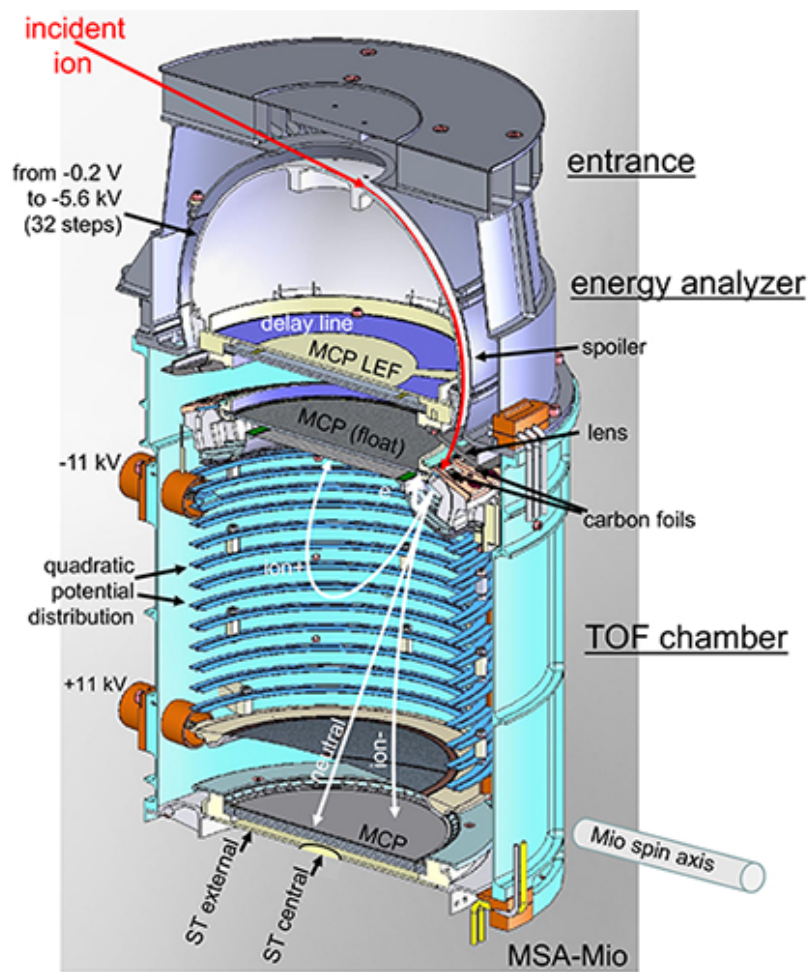
Fig. 39 Schematic illustration of MSA principles.
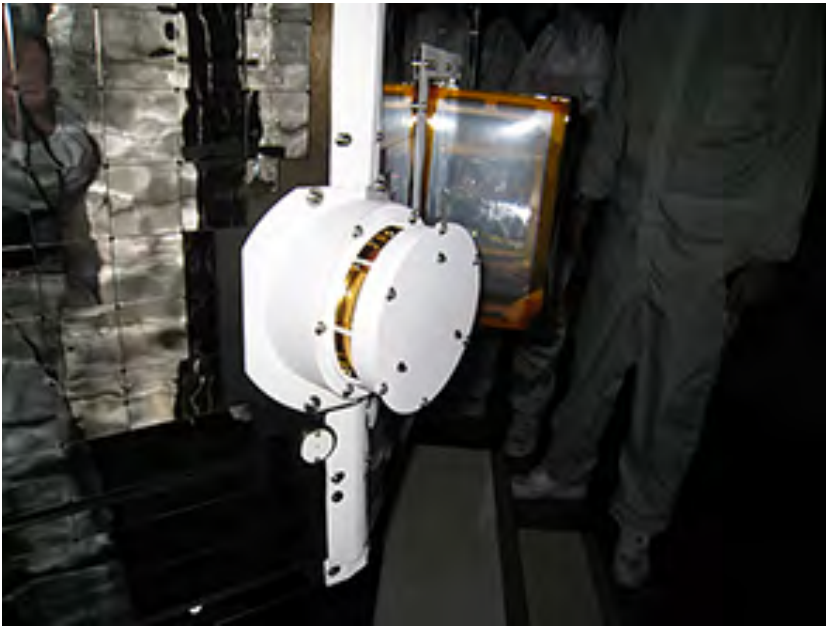
Fig. 40 Thermal shield of MSA.
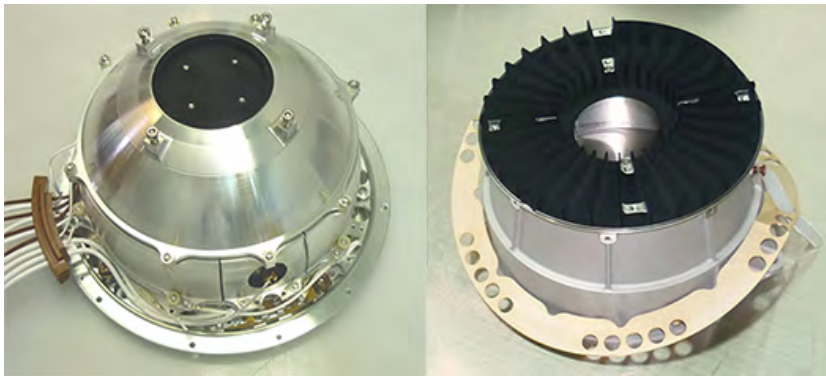
Fig. 41 Copper sulfide blackened energy analyzer (left) and entrance section (right).

Fig. 42 Energy analyzer (left, viewed from the back), and TOF chamber (right, view from top).
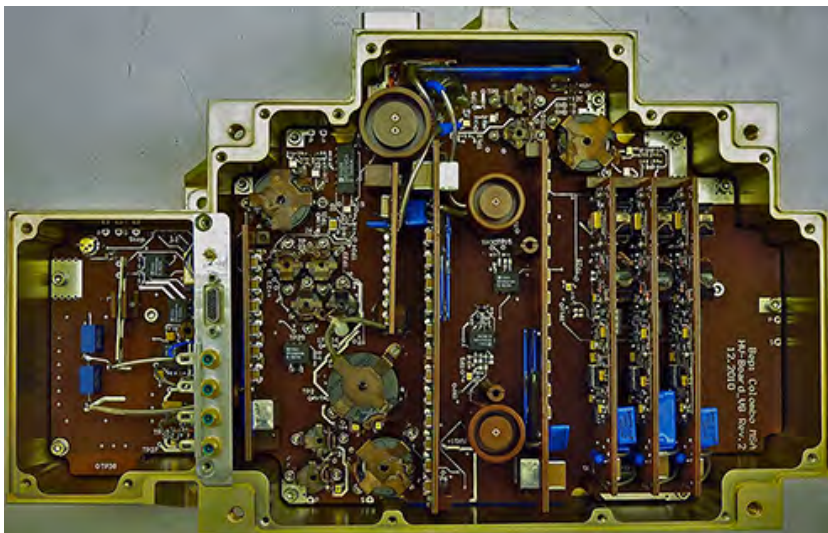
Fig. 43 MSA HPVS (top view).
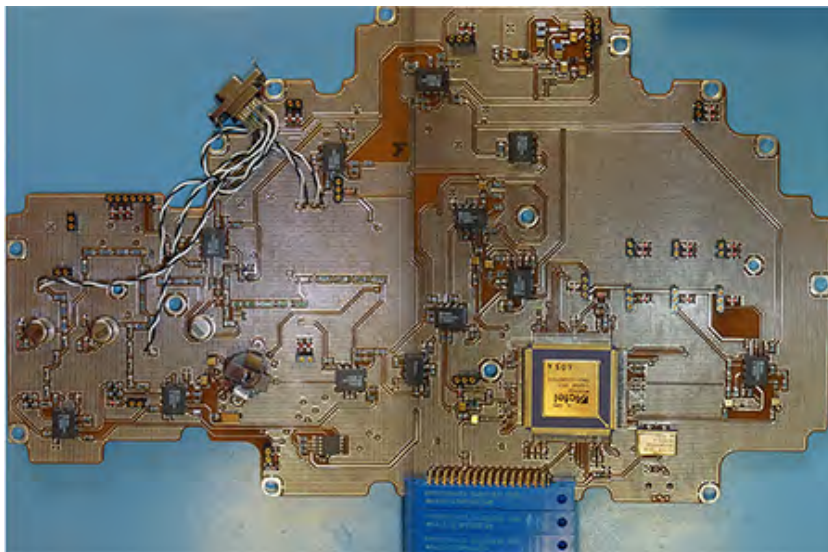
Fig. 44 MSA HVPS (bottom view).
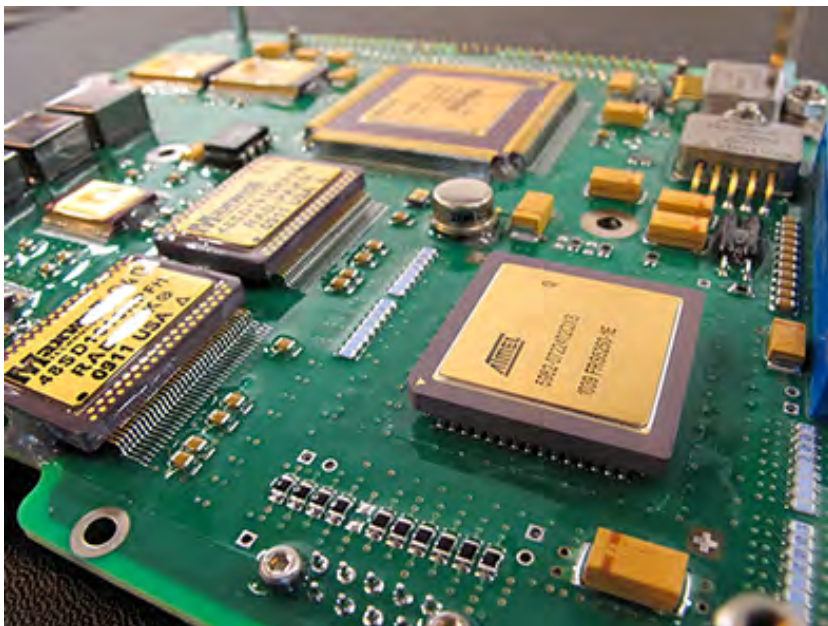
Fig. 45 MSA CPU (top view).
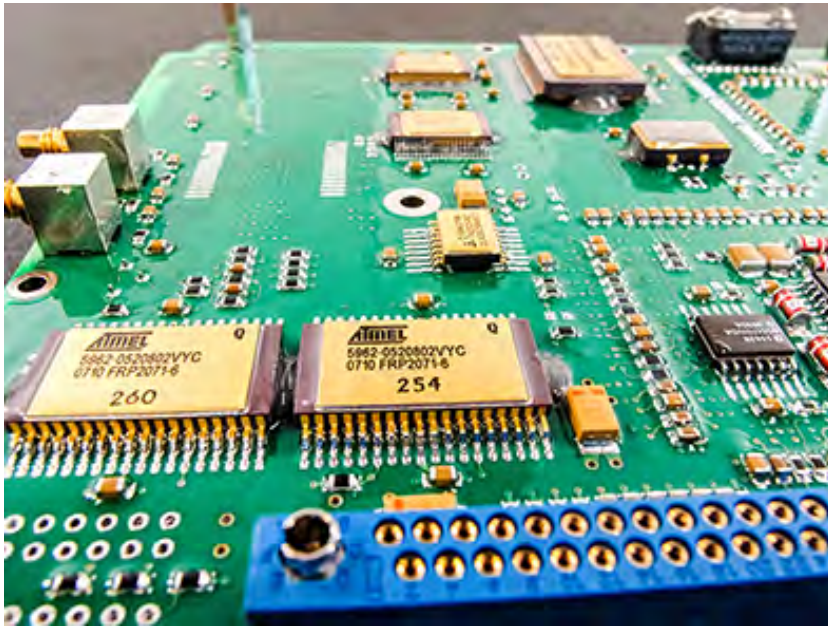
Fig. 46 MSA CPU (bottom view).
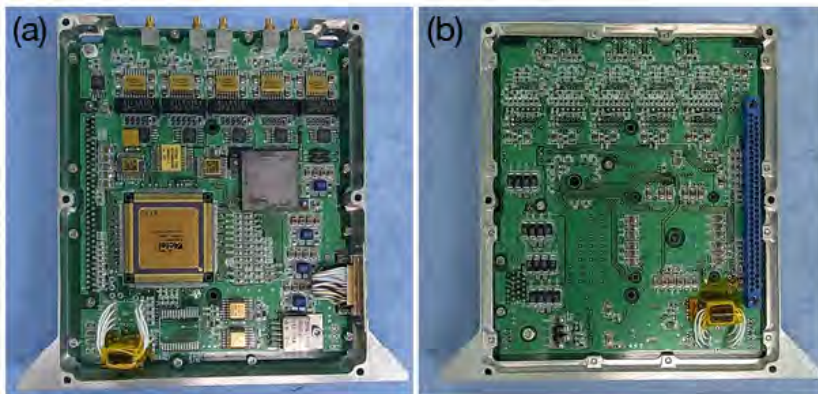
Fig. 47 MSA TOF signal amplifiers and SpaceWire interface. (a) top view (b) bottom view.
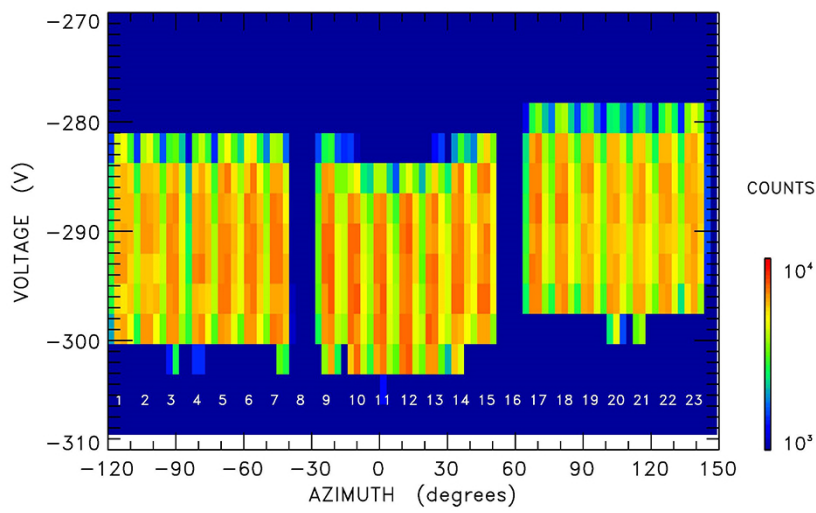
Fig. 48 Color-coded count rate as functions of azimuth and voltage applied on the inner sphere of the energy analyzer for a 2 keV N$^+$ beam.
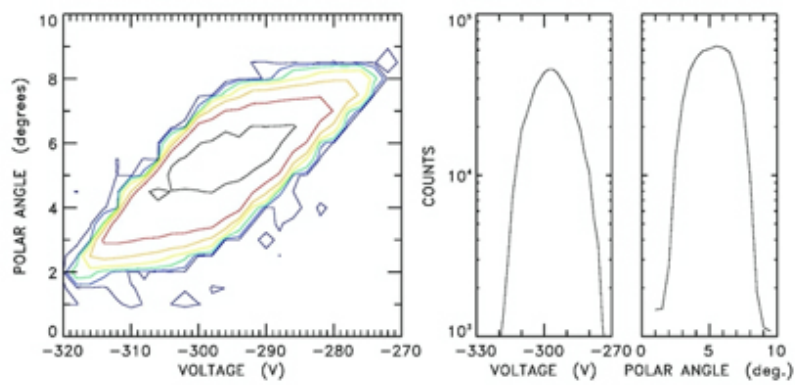
Fig. 49 Count rate contours as functions of the polar angle (elevation) and voltage (energy) for MSA entrance window No. 11 using a 2 keV N$^+$ beam (left). Integrated counts versus voltage and integrated counts versus elevation (right) (after Delcourt et al. (2016)).
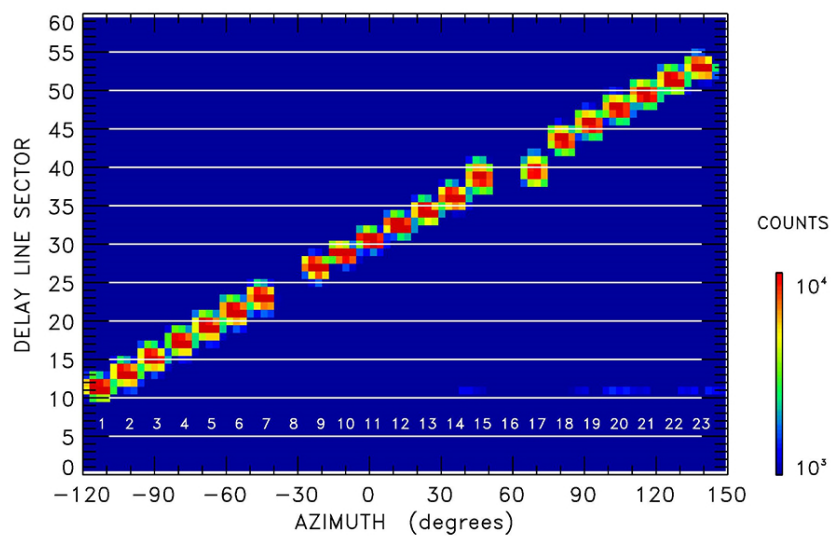
Fig. 50 Color-coded count rate as functions of azimuth and delay line sector for a 2 keV N^+ beam.
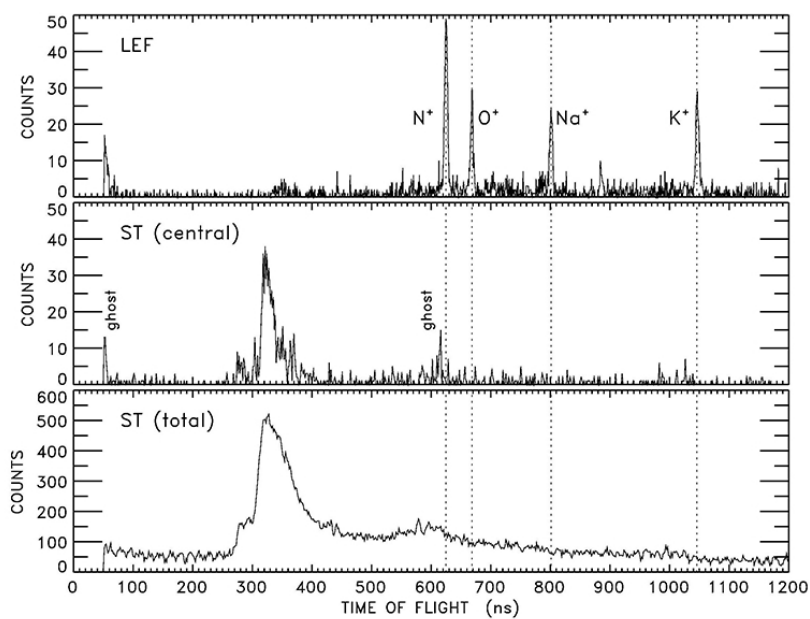
Fig. 51 TOF spectra for a 5 keV beam of N^+, O^+, Na^+ and K^+ ions with TOF chamber high voltage set to ± 11 kV. From top to bottom : LEF, central ST and total ST (after Delcourt et al. (2016)).
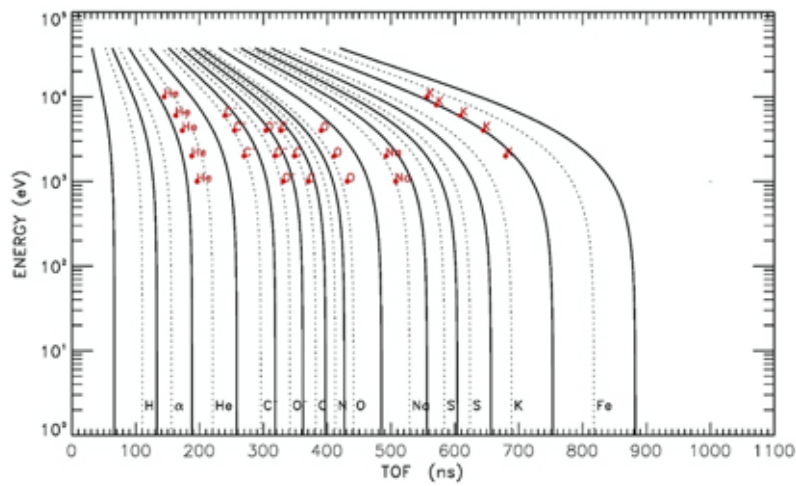
Fig. 52 TOF variation versus energy for different ion species (dotted lines) as obtained from equation (3) of Delcourt et al. (2016) with L = 16 cm. The solid lines depict the TOF intervals attributed to each species and the red dots show the results of MSA FM calibration. The TOF chamber voltage is set to 11 kV.
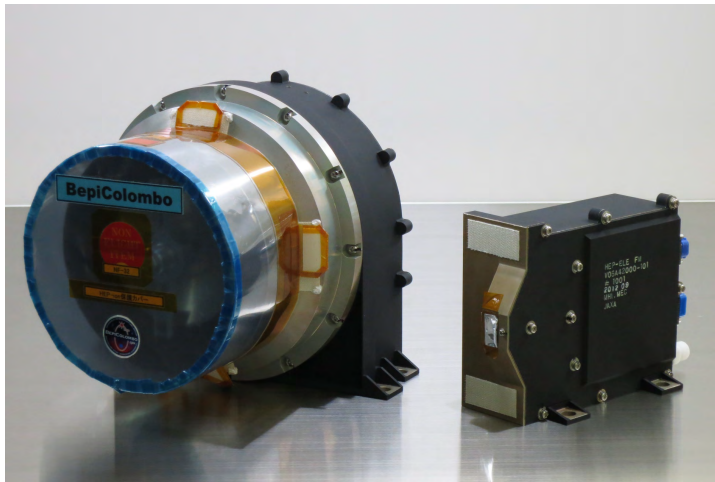
Fig. 53 HEP-ele and HEP-ion with some non-flight items(blue) in a clean bench.
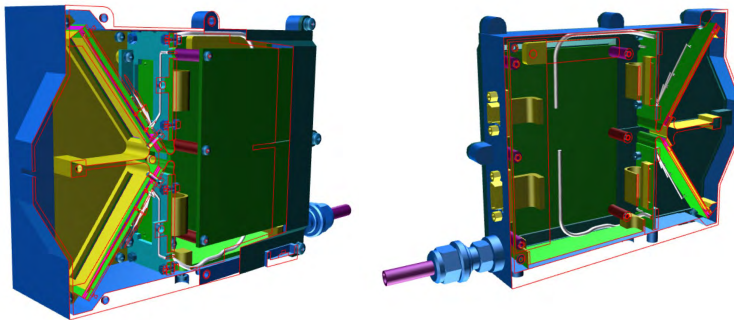
Fig. 54 Cross sections with slightly oblique cutaway of 3D drawing of HEP-ele from two directions.
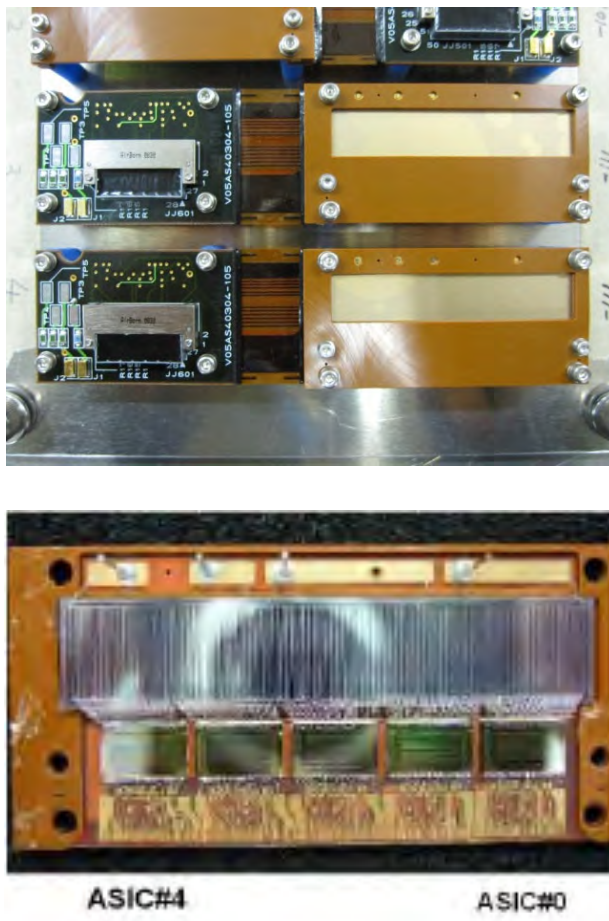
Fig. 55 SSSD-ASIC assembly of HEP-ele.
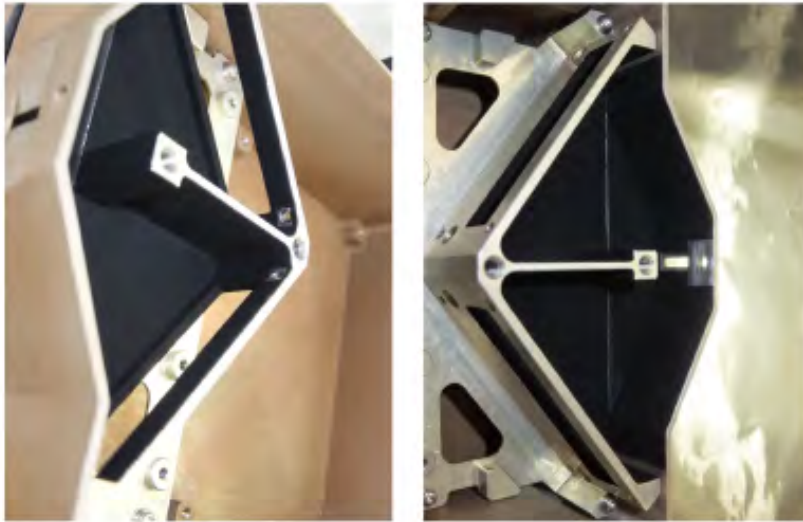
Fig. 56 HEP-ele detector section structures blackened with conductive paint.
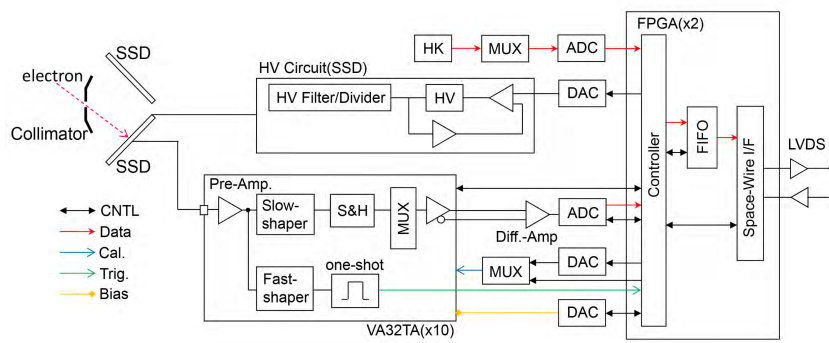
Fig. 57 Block diagram of HEP-ele.
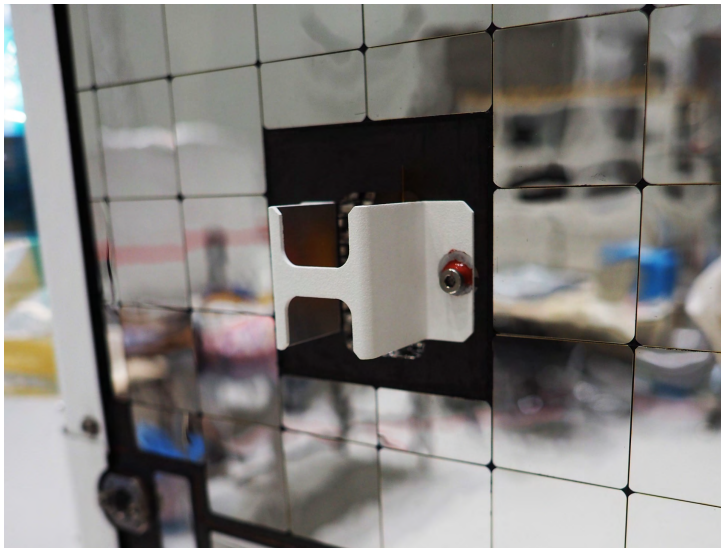
Fig. 58 HEP-ele onboard BepiColombo-Mio photographed during the final works before launch.
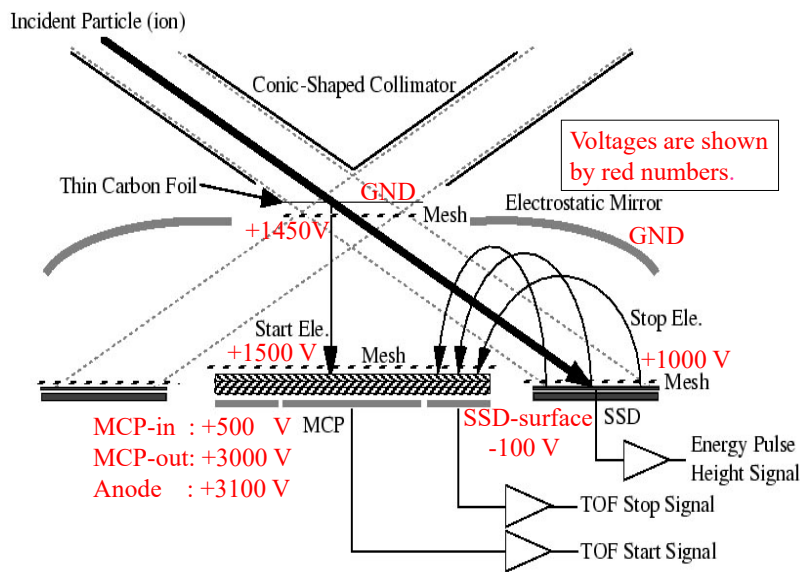
Fig. 59 Measurement principles illustrated on a cross-section of HEP-ion.
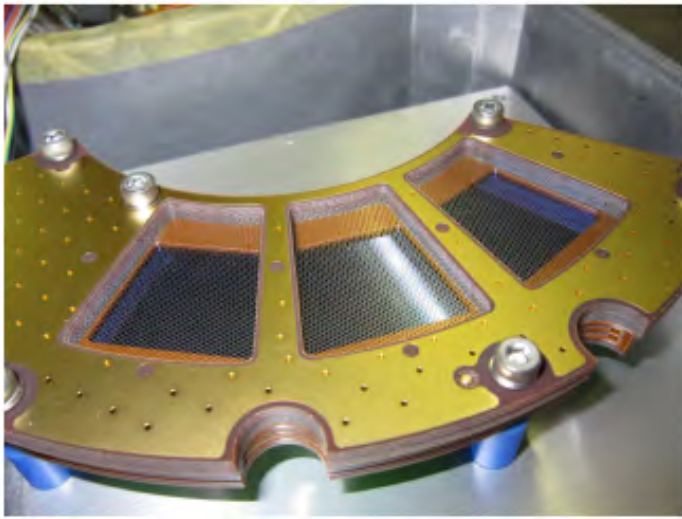
Fig. 60 Proto-type SSSD-ASIC assembly for HEP-ion, which is similar to that of the flight model.
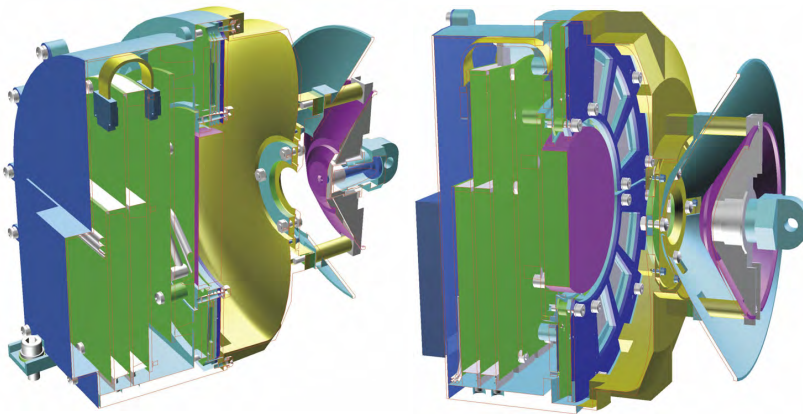
Fig. 61 Cross sections with slightly oblique cutaway of 3D drawings of HEP-ion from two directions.
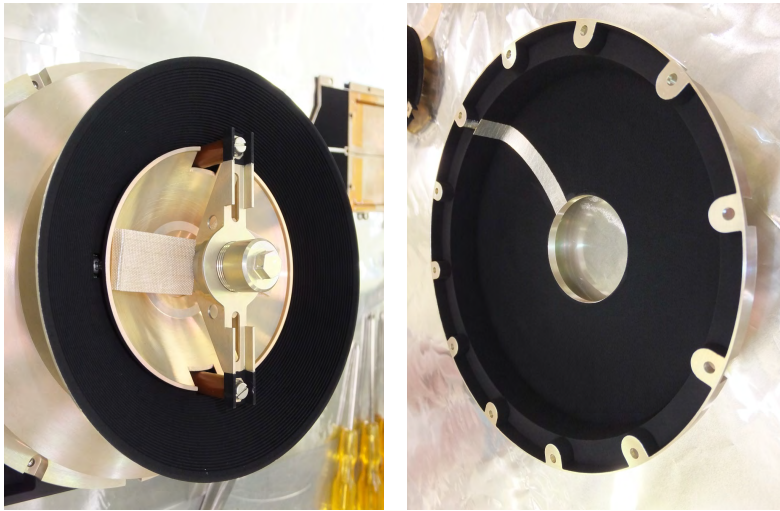
Fig. 62 HEP-ion collimator(left) and electrostatic mirror(right) of the TOF unit blackened with conductive paint.
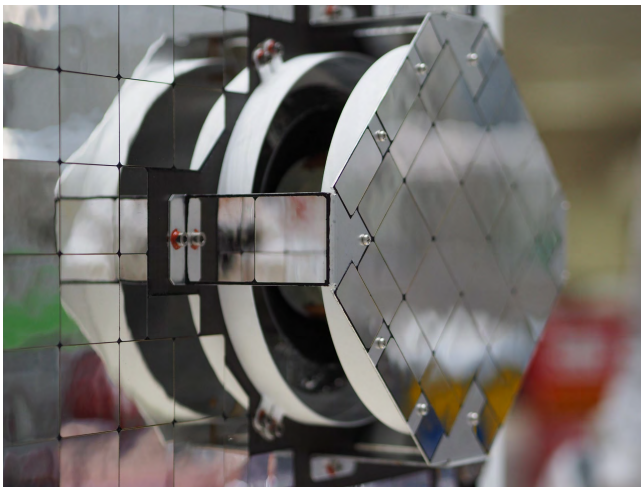
Fig. 63 HEP-ion onboard BepiColombo-Mio photographed during the final works before launch.
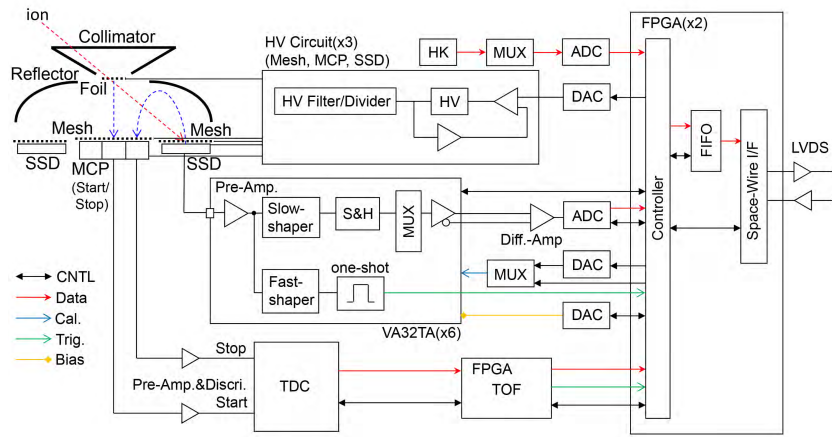
Fig. 64 Block diagram of HEP-ion.
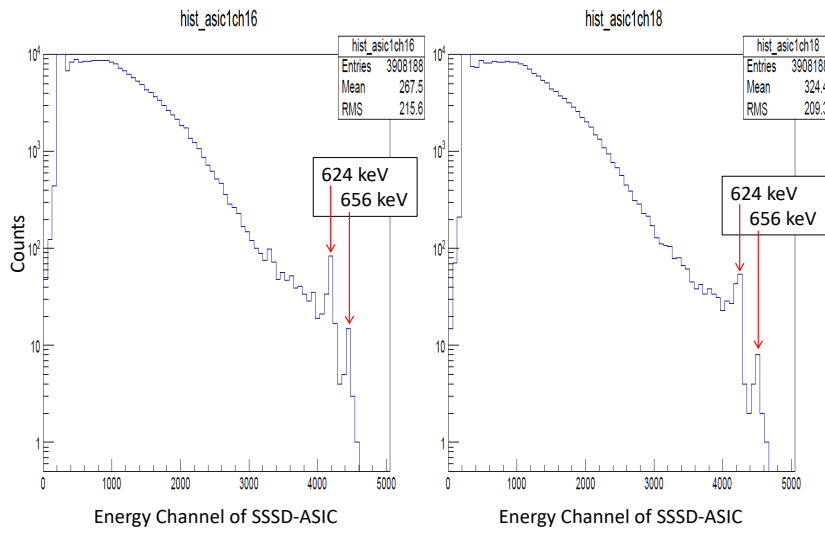
Fig. 65 Examples of pulse height analysis obtained for two strips of the SSSD-ASIC assemblies in HEP-ele.

Fig. 66 Calibration facility at the Solar-Terrestrial Environment Laboratory(currently the Institute for Space-Earth Environmental research, ISEE) at Nagoya University.
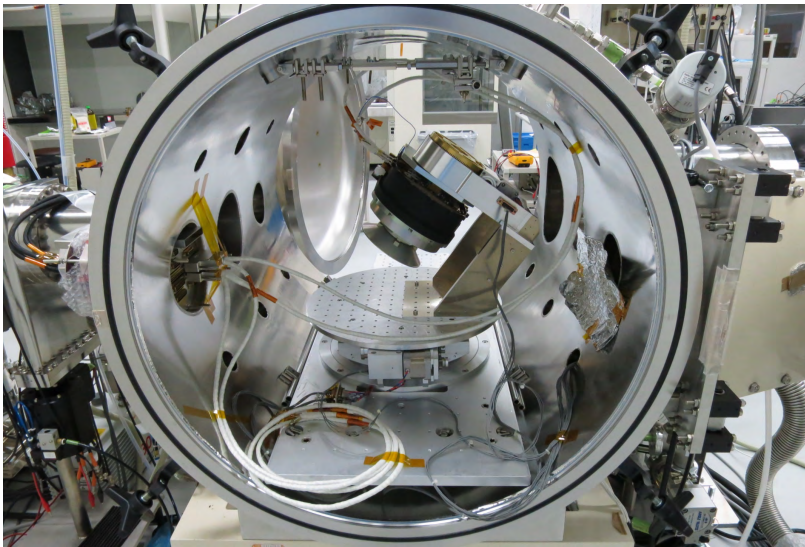
Fig. 67 HEP-ion set on the multi-axial turntable system in the vacuum chamber at the beamline calibration facility.
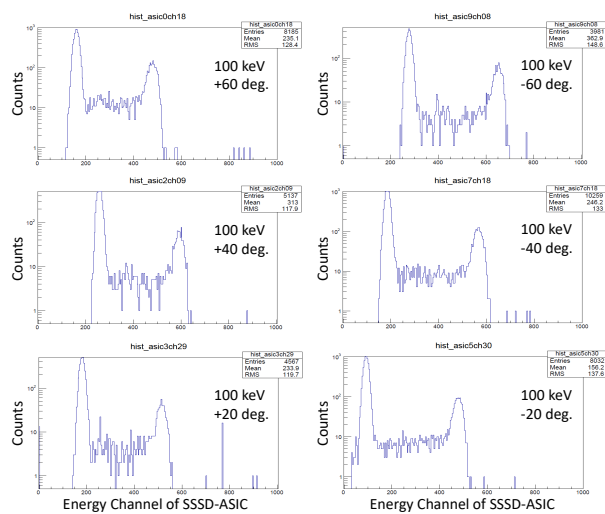
Fig. 68 Examples of pulse height analysis for six incident (polar) angles obtained in the correspondent strips of two SSSD-ASIC assemblies in HEP-ele.
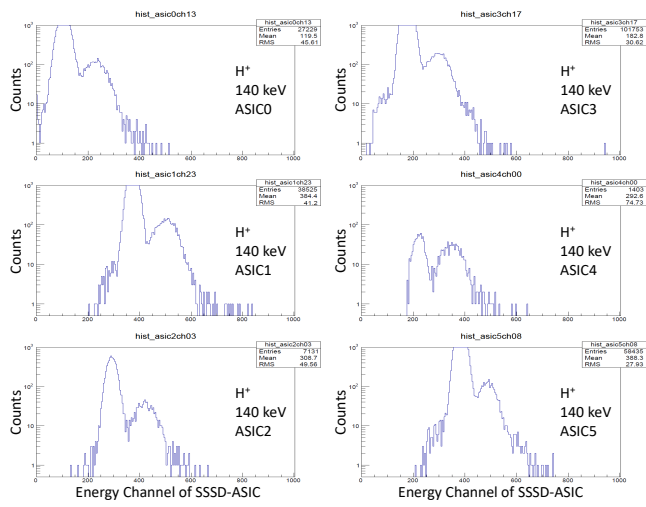
Fig. 69 Examples of pulse height analysis for six incident (polar) angles corresponding to the SSSD-ASIC pairs in HEP-ion.
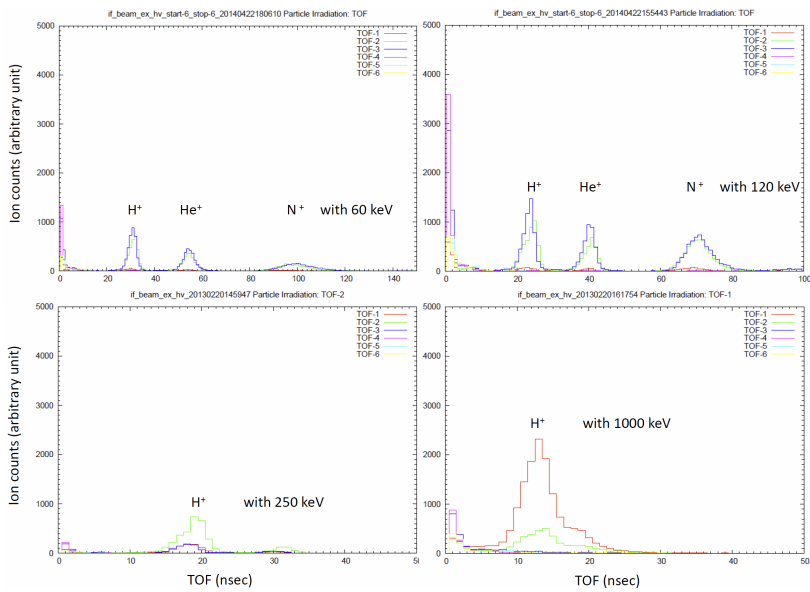
Fig. 70 TOF profiles for ions with energies of 60, 120, 250, and 1000 keV. Only protons were available for energies beyond 150 keV because of the beamline facility performance.
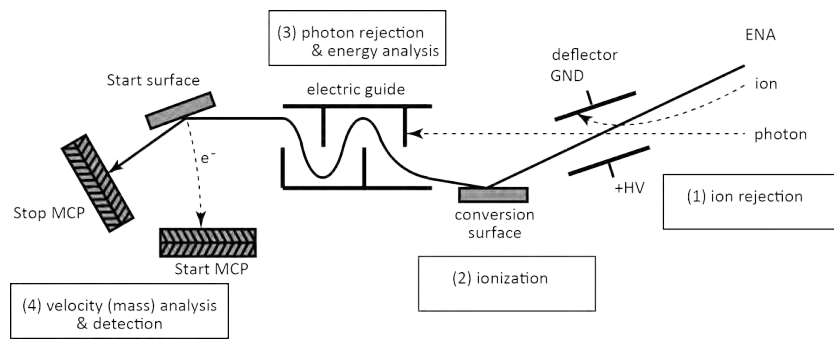
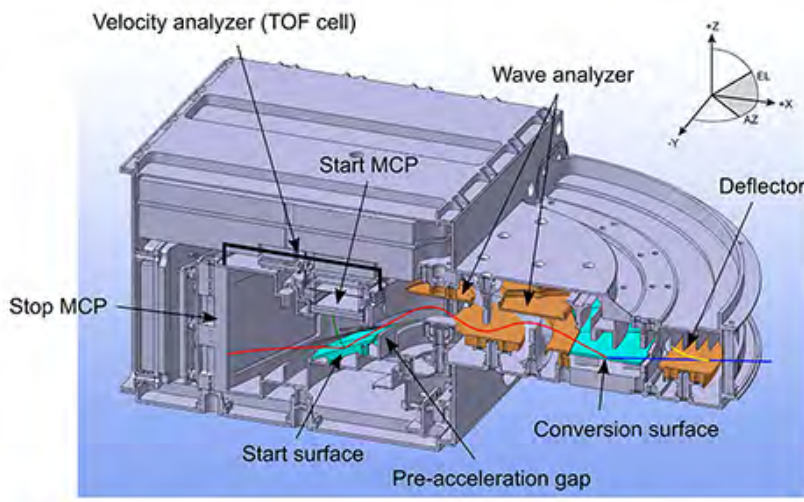**Fig. 71** ENA measurement concept.

Fig. 72 Sectional view of the ENA sensor.

Fig. 73 ENA flight model. The sensor is wrapped by MLI, when ENA is installed in the spacecraft.
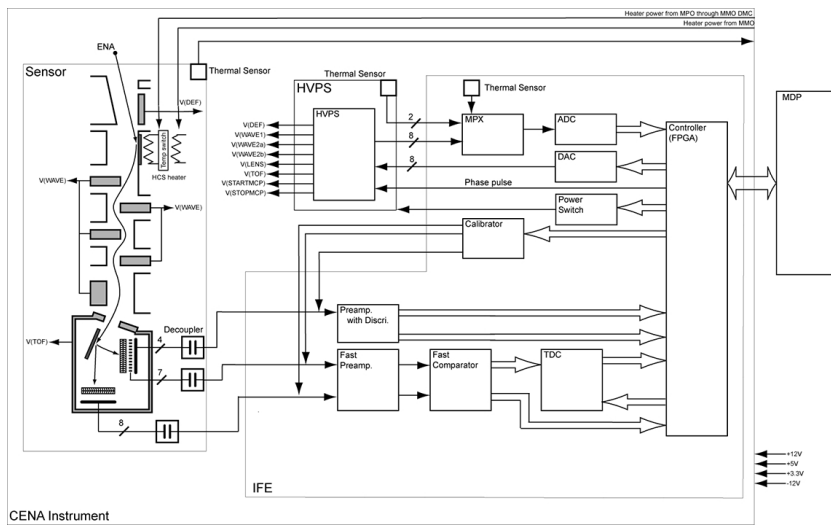
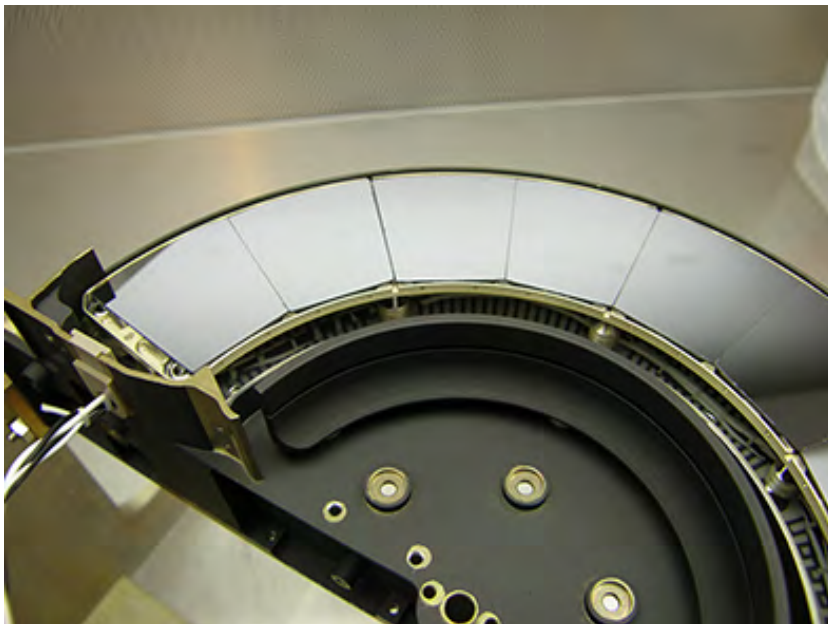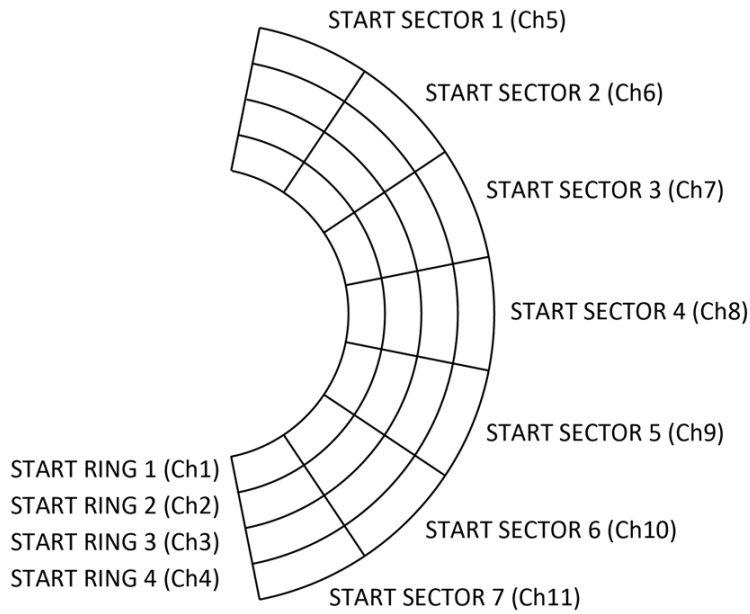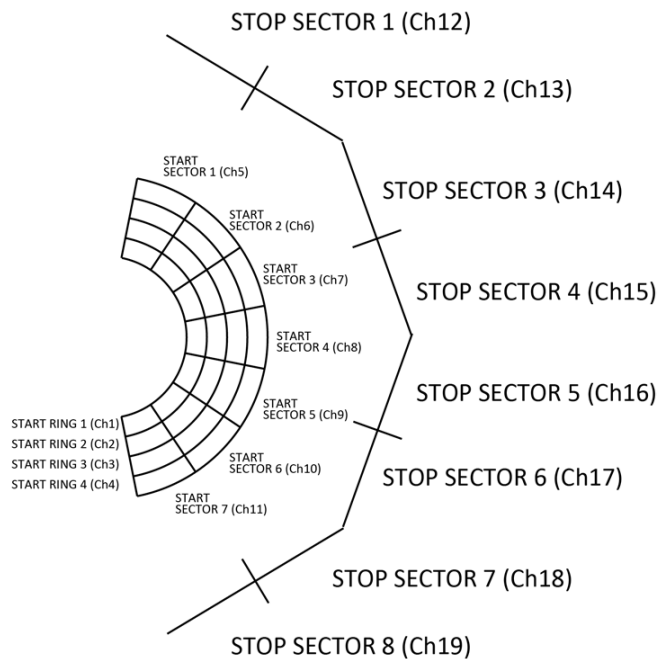**Fig. 74** ENA sun shield.

**Fig. 75** ENA block diagram.

Fig. 76 Conversion surfaces of ENA.

MMO MPPE ENA
START MCP Anode Channel Definition
(View from START MCP input surface)

START SECTOR 1 (Ch5)

START SECTOR 2 (Ch6)

START SECTOR 3 (Ch7)

START SECTOR 4 (Ch8)

START SECTOR 5 (Ch9)

START RING 1 (Ch1)
START RING 2 (Ch2)
START RING 3 (Ch3)   START SECTOR 6 (Ch10)
START RING 4 (Ch4)
                            START SECTOR 7 (Ch11)

STOP MCP Anode Channel Definition

STOP SECTOR 1 (Ch12)

STOP SECTOR 2 (Ch13)

START
SECTOR 1 (Ch5)
                    STOP SECTOR 3 (Ch14)
         START
         SECTOR 2 (Ch6)
                STOP SECTOR 4 (Ch15)
            START
            SECTOR 3 (Ch7)
               START
               SECTOR 4 (Ch8)
                    STOP SECTOR 5 (Ch16)
                 START
                 SECTOR 5 (Ch9)
START RING 1 (Ch1)
START RING 2 (Ch2)
START RING 3 (Ch3)   START
START RING 4 (Ch4)   SECTOR 6 (Ch10)   STOP SECTOR 6 (Ch17)
               START
               SECTOR 7 (Ch11)

                    STOP SECTOR 7 (Ch18)
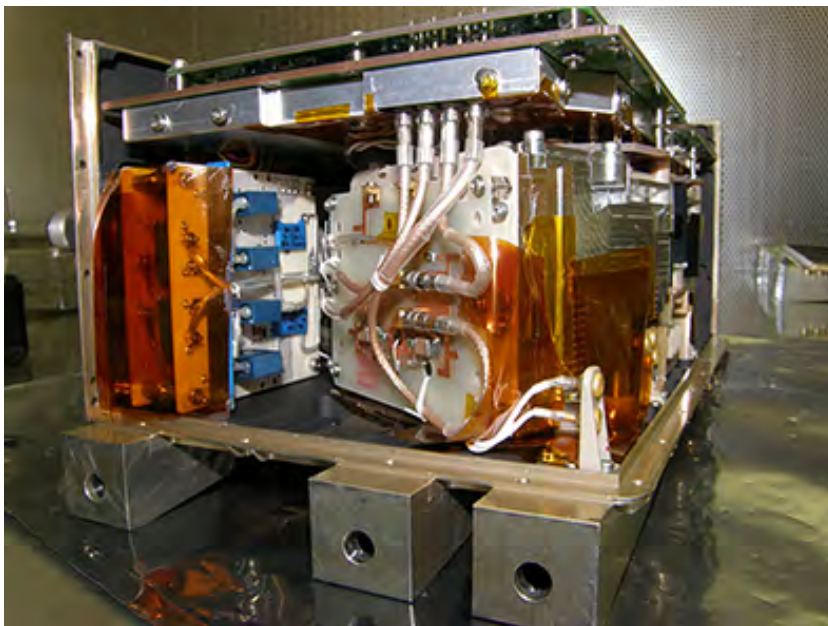
STOP SECTOR 8 (Ch19)

Fig. 77 Channel definition of the MCP anodes of ENA. The lower panel showing the channel definition of the STOP MCP anodes includes the channel definition of the START MCP anode which is the same as that in the upper panel.
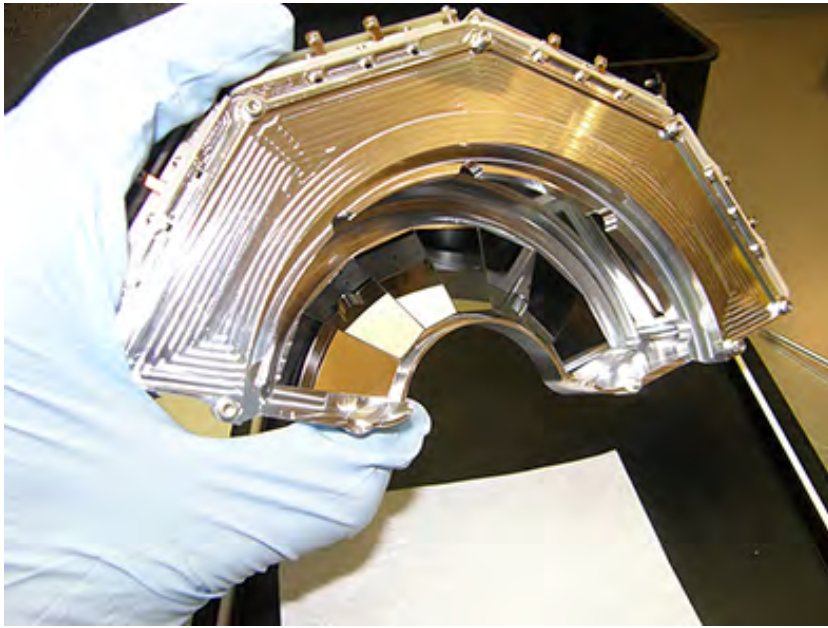
Fig. 78 START surface installed in the electrode structure of the TOF section.

Fig. 79 Assembled configuration of the HVPS, STOP MCP assembly, and preamplifier/digital processing electronics boards.
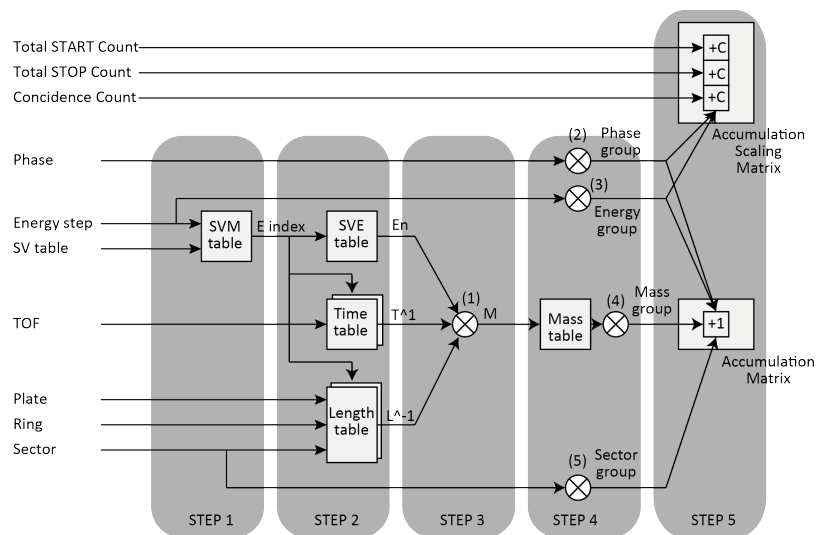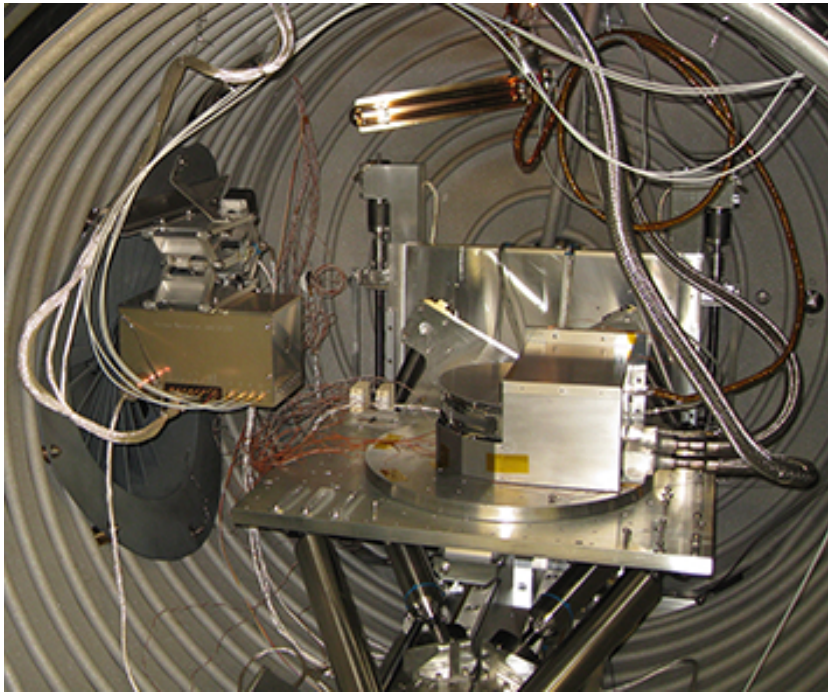
Fig. 80 Schematic diagram of the calculation flow in mass accumulation mode.

Fig. 81 ENA at the MEFISTO calibration facility. The neutral beam is emitted from the beam neutralizer on the left (gold box). ENA (center) is encapsulated in thermal insulation sheets to facilitate temperature control. The entire instrument setup can be moved and rotated relative to the incoming neutral beam with 6° of freedom.
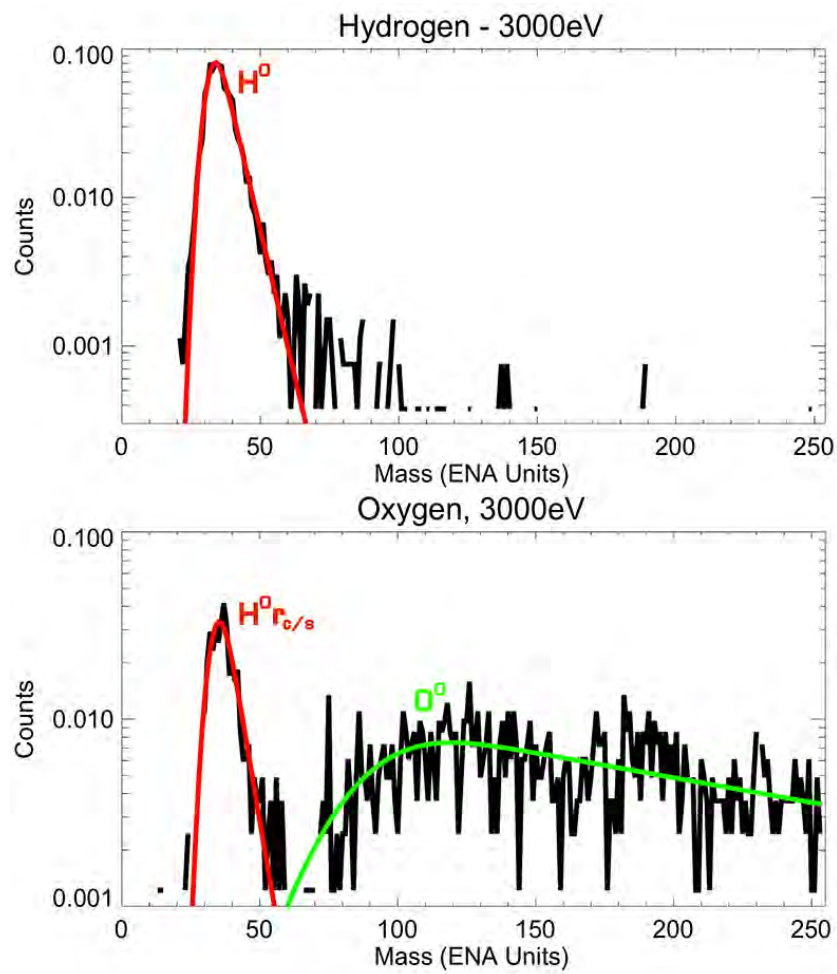
Fig. 82 Typical mass spectra for incident neutral hydrogen (top) and oxygen (bottom). The black lines show the measured data, the colored lines are fitted curves. H^0: hydrogen peak, O^0: oxygen peak, $H^0r_{c/s}$: hydrogen signal owing to a recoil process at the conversion surface. The X-axis in both plots is in mass bin units M as shown in Figure 80 and the Y-axis is in arbitrary units.